ABSTRACT

Title of Dissertation: LATTICE-MATCHED GROWTH OF TOPOLOGICAL SEMIMETAL CADMIUM ARSENIDE ON VIRTUAL TERNARY III-V SUBSTRATES

Thomas G. Farinha, Doctor of Philosophy, 2025

Dissertation directed by: Professor Christopher J. K. Richardson, Department of Materials Science and Engineering, Laboratory for Physical Sciences

Topological materials are a recently discovered electronic class which exhibits electronic band structures that deviate from the behavior of conventional electronic materials. These topological materials exhibit conical bands and host unique band elements such as Dirac and Weyl nodes through which phenomena such as the quantum Hall effect, quantum anomalous Hall effect, and the quantum spin Hall effect may be realized. These effects are protected against the destabilizing effects of thermal fluctuations through crystal symmetry-derived protection. The topological

semimetal Cd_3As_2 is an excellent candidate for the realization of novel devices through magnetic alloying because of its demonstrated high electron mobility (>10,000 $cm^2/V•s$). This dissertation details the molecular beam epitaxy growth and characterization of topological semimetal Cd_3As_2 thin films that are lattice-matched to ternary III-V alloy virtual substrates and optimized for high crystalline quality.

This dissertation will first review the deposition of Cd_3As_2 and the relevant calculations made to determine the suitability of virtual substrates for its lattice matched-growth. Therefore, the stability of ternary III-V alloy buffers and their interfaces with Cd_3As_2 are discussed. Thermal and spinodal decomposition ranges for the ternary III-V alloys are also determined to fully understand them as virtual substrates for Cd_3As_2. Cd_3As_2 thin films are grown with thicknesses targeting 30-100 nm. Three ternary III-V alloy systems GaInSb, AlInSb, and InAsSb are grown on both GaAs and AlAs buffers, using GaAs (001) as a substrate. The structural properties of these high-quality, epitaxially grown single crystals are characterized using *in situ* pyrometry, reflection high-energy electron diffraction, high-resolution X-ray diffraction, X-ray reflectivity, atomic force microscopy, cross-sectional scanning electron microscopy, and tunneling electron microscopy. The optimal processing parameters for producing these Cd_3As_2 thin films and their virtual substrates are described in detail for easy application in future molecular beam epitaxy.

Assessment of the electronic properties of Cd_3As_2 are conducted using Van der Pauw geometry Hall measurements at 2K with external magnetic fields ranging up to 14 T. The electronic attributes of resistivity, carrier density and mobility, and the presence of the quantum Hall effect are probed and reported. The potential epitaxy of different magnetic Cd_3As_2 alloys and proximal magnetic films are explored through calculations of Gibbs free energy. Sm is chosen as the candidate for future work seeking the quantum anomalous Hall effect in magnetic Cd_3As_2.

LATTICE-MATCHED GROWTH OF TOPOLOGICAL SEMIMETAL CADMIUM ARSENIDE ON VIRTUAL TERNARY III-V SUBSTRATES

By

Thomas G. Farinha

Dissertation submitted to the Faculty of the Graduate School of the
University of Maryland, College Park, in partial fulfillment
of the requirements for the degree of
Doctor of Philosophy
2025

Advisory Committee:
Professor Ichiro Takeuchi, Chair
Professor Christopher J. K. Richardson, Advisor
Professor Lourdes G. Salamanca-Riba
Professor John Cumings
Professor Johnpierre Paglione, Dean's Representative

Acknowledgements

Firstly, I would like to recognize the system by which I was able to even attempt my PhD work communicated in this dissertation. It is only through the combined wisdom, efforts, and resources of millions now and in the past that the knowledge and tools that I have used were made available to me. It is my great hope that this work will act as another drop in a sea of effort made to build the combined body of science and technology.

Secondly, I thank every advisor, teacher, and mentor that has aided me in times of confusion, inexperience, and error. To my current advisor, Chris Richardson, I express the utmost gratitude in proving an education that reaches far beyond the realm of mere calculations and data analysis. Under your advisorship I have learned to be a scientist, an engineer, a mechanic, an electrician, and at some points even a dishwasher (as far as cleaning glassware is concerned). Wherever I end up, I know that I will be able to use at least one of the skillsets that I gained during my PhD research.

To my fellow graduate students and coworking researchers, I thank you for many positive and constructive discussions both within and beyond the purview of my PhD research. Learning is the foundation of this experience, and so I am most appreciative of those who helped me learn, those who learned with me, and those who gave me an opportunity to relay what I have learned. I thank fellow students Austin Thomas, Dmitri Krymski, and Riis Card. I thank (now) postdocs Margaret Samuels and Ashish Alexander, and hired postdocs Chomani Gaspe, Josh Thompson, Neda Forouzani, Nick Grabon, Edwin Chung, Rohit Pant, and Jason Dong. I thank our favorite (and only) staff scientist Alan Kramer. From my former group, I thank my previous advisor Marina Leite along with John Howard, Natalie Schwab, Nick Dzuricky, Richa Lahoti, and John Hoerauf.

To the other professors that have guided me through the most difficult and unfamiliar concepts that I have ever encountered, I thank you for bearing with my many questions, some of which you may have already answered beforehand. I thank professors Oded Rabin, Daniel Josell, Lourdes G. Salamanca-Riba, John Cumings, and Cheng Gong.

To the support staff that kept the intricate laboratories where I worked, I thank you for the long hours of maintenance work and your near-instantaneous support during times of crisis. I also thank you for teaching me the fundamental operation of many different processes, as many of you have a far greater understanding of these tools than I could hope to obtain in my short time at UMD. In the Laboratory for Physical Sciences, I thank Jim Fogleboch, Steve Brown, Paul Hannah, Toby Olver, Warren Berk, Jason Moody, Trey Kirlew, Curt Walsh, Tom Salter, Quinn Fowler, and Doug Ketchum. In the UMD FabLab I thank Tom Loughran, Jon Hummel, John Abrahams, and Mark Lecates. In the UMD Surface Analysis Center, I thank Dr. Karen Gaskell.

Thirdly, I thank my friends and family, to whom I've confided all of my successes and failures as my research has been completed. I thank my mother Sheryl and my father Mark, both of whom have traveled this path as graduate students before me. Their absolute support as parents, teachers, and fellow students is incalculable. I thank my brother Carter and my friends Trevor, Liam, Sean, and Jon as they have withstood five years of a graduate student's incomplete rendition of modern materials science.

Lastly, I thank all sources of funding that have graciously allowed for the completion of this research. I would like to acknowledge the A. James. Clark School of Engineering in particular, which awarded me a Clark Doctoral Fellowship with funding for my first year as a graduate student and continuous support throughout my graduate assistantship.

Table of Contents

List of Tables

List of Figures

List of Abbreviations

Spin-Orbit Coupling (SOC)

Three-Dimensional (3D)

Topological Insulator (TI)

Topological Semimetal (TS)

Density of States (DOS)

Thouless-Kohmoto-Nightingale-den Nijs (TKNN)

Inversion (P)

Time-Reversal (T)

Quantum Hall Effect (QHE)

Quantum Anomalous Hall Effect (QAHE)

Two-Dimensional (2D)

Quantum Spin Hall Effect (QSHE)

Ultra-High Vacuum (UHV)

Molecular Beam Epitaxy (MBE)

Density-Functional Theory (DFT)

Face-Centered Cubic (FCC)

Magnetic Topological Memory (MTM)

Topological Magnetoelectric Transistor (TMET)

Beam-Equivalent Pressure (BEP)

Ion Gauge (IG)

Reflection High Energy Electron Diffraction (RHEED)

X-Ray Diffraction (XRD)

Full-Width at Half-Maximum (FWHM)

Relative Intensity (RI)

Reciprocal Space Mapping (RSM)

X-Ray Reflectivity (XRR)

Atomic Force Microscopy (AFM)

Cross-Sectional Scanning Electron Microscopy (XS-SEM)

Threading Dislocation Density (TDD)

Delta Lattice Parameter (DLP)

Root Mean Square (RMS)

Fourth-Row Transition Metal (FRTM)

Rare Earth (RE)

Coordination Number (CN)

Chapter 1: Topological Materials and the Role of Magnetism

1.1 Description of topological band structure

Unique physical phenomena such as quantized electronic behavior and non-trivial magnetoelectric responses have become a major focus of electronic materials research in the past few decades. Within the scope of this effort lies the discovery and subsequent investigation of a new set of electronic classes belonging to what are now recognized as topological materials (1). Topology generally refers to the study of properties which remain constant during the smooth, continuous deformation of shapes, such as electronic bands.

The designation of non-trivial is shorthand for an electronic phase which does not belong to the same electronic structure as the trivial (normal) insulating phase of materials, which includes semiconductors. In other words, the electronic bands of these topological materials cannot be smoothly deformed to produce a trivial insulating phase, and vice-versa. These topological classes of electronic band structures are defined by mathematical quantities known as topological invariants. These values remain invariant in describing a band structure so long as only smooth, continuous transformations are applied to it. As such, if any topological invariant is nonzero then the material is considered topologically non-trivial. Topological invariants are descriptors of specific behavior, so there are separate invariants for different phenomena.

Because trivial and non-trivial topological phases have at least one dissimilar topological invariant, a discontinuous band structure operation is required to move between them. For example, a topological insulator in an insulating atmosphere must necessarily have conducting surfaces/edges to account for the electronic phase transition.

The source of topologically non-trivial electronic behavior is the inversion of the conduction and valence bands in k-space owing to the effect of high Spin-Orbit Coupling (SOC) (2). These inversions produce a near-linear band dispersion in close proximity to the crossing where infinite curvature demands a massless electronic state. This intersection, the Dirac node, has an associated set of Dirac cones which emanate from the crossing. The Dirac node/cones are the overlap of two spin-momentum locked Weyl nodes/cones with opposing chirality. Spin-momentum locking derived from SOC requires that the electron spin and momentum vectors remain perpendicular. Each Weyl node is at the center of helical conic trajectories supporting the movement of a single electron spin at the same energies as the corresponding Dirac cone.

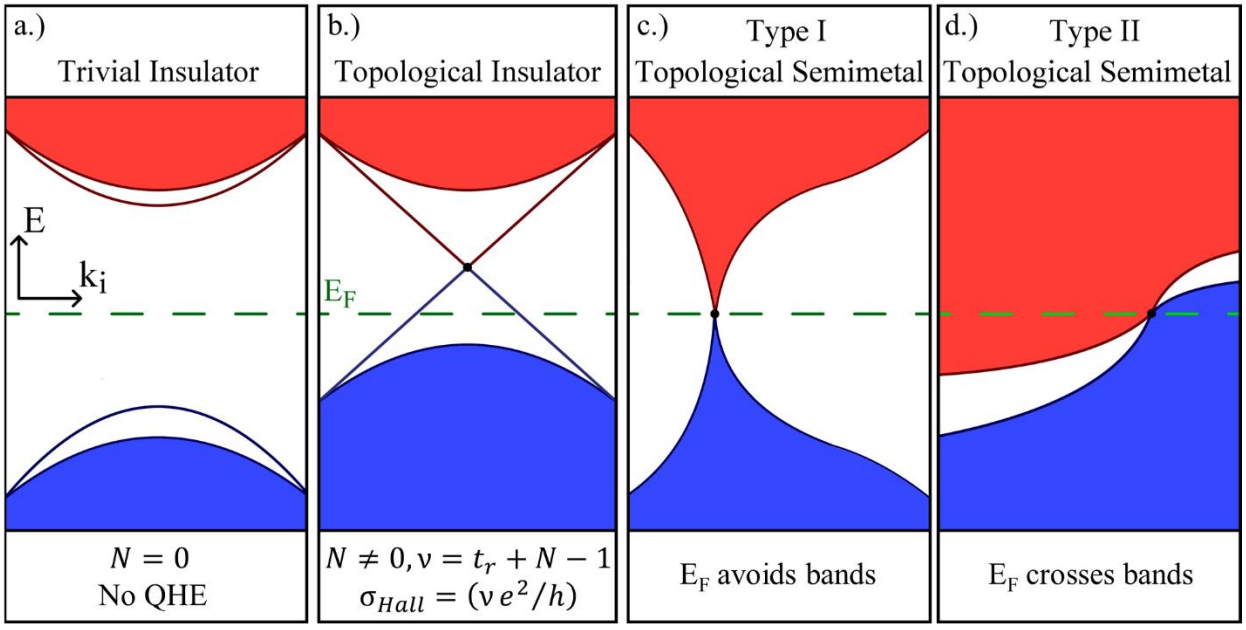

Figure 1.1: Band structures of common electronic phases. a.) represents the trivial insulator phase and b.) represents the topological insulator phase. c.) and d.) represent the bulk bands of Type I and II topological semimetals.

The diagram in Figure 1.1 illustrates the distinction between trivial insulators, Three-Dimensional (3D) Topological Insulators (TIs), and 3D Topological Semimetals (TSs). Energy is shown with respect to an arbitrary k-space axis k_i, which is usually along a high symmetry axis in the Brillouin zone. Bulk material bands for a.) trivial and b.) topological insulators are represented by shaded regions. The surface bands for a.) and b.) appear as lines in this E-k_i planar perspective. TIs are fully gapped in their bulk band structure and exhibit band inversion so that their surface bands host Dirac cones. The Fermi energy level lies within the bulk band gap, hence the use of the insulator terminology despite the presence of conducting surface states. The surface bands in b.) correspond to the Dirac cone(s) in the TI that allow for surface conduction in what is otherwise a bulk insulator. In a magnetic field, the TI surface Density of States (DOS) is composed of N discretized distributions known as Landau levels. The quantized Hall conductance in TIs, $\nu e^2/h$, is a function of both the Thouless-Kohmoto-Nightingale-den Nijs (TKNN) invariant N and the Diophantine equation solution t_r outlined in the originating work (3). A nonzero N for the surface states of these TIs is a result of them being topologically distinct from a trivial insulator.

In contrast to a TI, a 3D TS such as Cd_3As_2 exhibits Dirac/Weyl nodes in its bulk band structure with the Fermi energy level crossing at least one of the intersections (2,4). This produces both conductive surface and bulk bands which may transport free carriers with no energy gap. c.) and d.) contrast two similar topological structures known as Type I and Type II Weyl TSs (2,5). Their distinction lies in the behavior of their surface bands with respect to the Fermi energy level. In the less common Type I Weyl TS (e.g. Cd_3As_2) the Fermi level crosses between the conduction and valence bands as it intersects the Weyl nodes. In the more common Type II Weyl TS (e.g. WTe_2) the Fermi level crosses from the area within one band to the other. This classification is important because it gives insight into the minimum required number of Weyl nodes for the

topological phase to exist, as well as the energy and k-space movements necessary for carrier movement.

Surface transport between Weyl nodes is done through topologically protected spin-polarized channels known as Fermi arcs. They connect the circular Weyl cone projections on the Weyl TS surface (6). Dirac TSs may also exhibit Fermi arcs that connect two Dirac nodes. They are mirrored because as one connects the positive chirality Weyl cone of the first Dirac cone to the negative chirality Weyl cone of the second Dirac cone, and vice-versa. Fermi arcs in Dirac TSs are not topologically protected and may be closed off into Fermi contours which do not connect separate Dirac nodes (7).

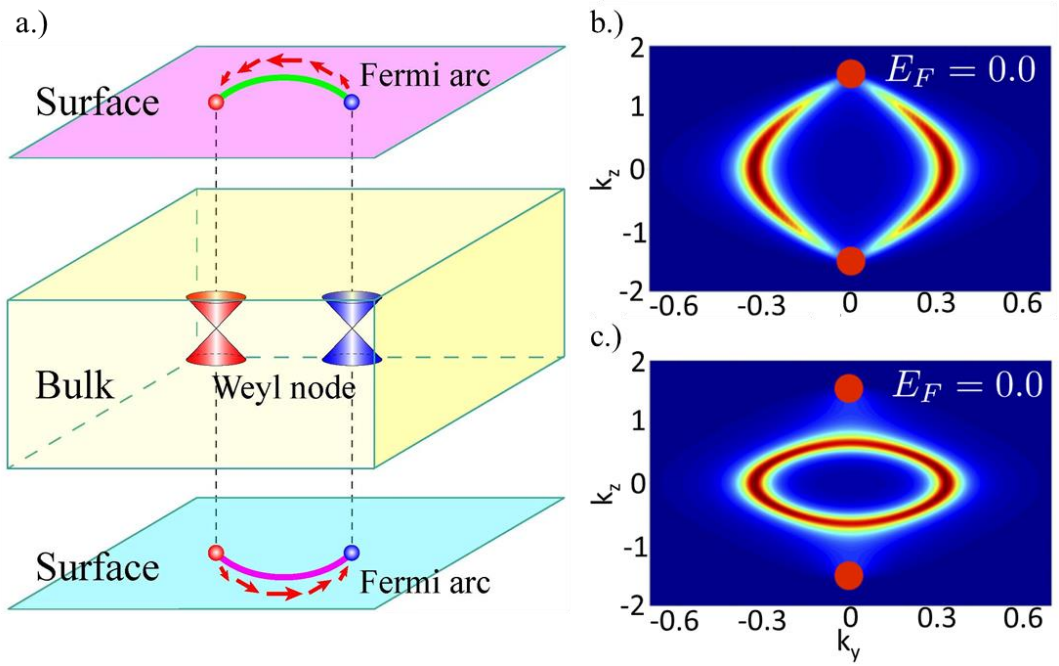

Figure 1.2: a.) Illustration of spin-locked transport in a Weyl Topological Semimetal (TS) (6). Carriers move across the TS surface through Fermi arc channels. Fermi arcs in a Dirac topological semimetal where b.) they provide a path between two separate Dirac nodes and c.) where they form a Fermi contour and do not provide a path (7). The connected Dirac nodes exist at the same energy in the k_y-k_z plane.

Regarding the experimental system, two topologically-protected Dirac nodes appear with the inversion of the 5s and 4p bands along the *c*-axis of the Cd_3As_2 unit cell (8). This is the Z-Γ-Z axis in the Brillouin zone, and the Dirac nodes are symmetric around Γ. The nominally degenerate Weyl cones composing the Dirac nodes are separated in k-space when certain crystal symmetries, such as Inversion (*P*) and Time-Reversal (*T*) symmetries, are broken causing them to lose their degeneracy. Both Dirac and Weyl cones existing within the surface band structure of topological materials lead to unique modes of carrier transport which support quantized versions of the Hall effect.

In the absence of a magnetic field, the surface states of TIs and TSs are protected against gapping by *T*-symmetry within the system, and therefore remain conducting (1). When *T*-symmetry is broken either through either an external magnetic field or an internal magnetic moment the surface conduction is still maintained through the emergence of Fermi arcs which demand spin-dependent carrier transfer. These edge channels also host unique effects like spin-momentum locking which may be useful in future spintronic devices (9). The wide versatility of these topological classes through the use of *P* and *T*-breaking operations leads to the desire for material systems with the prerequisite electronic properties for realized, practical topological electronics.

Topological electronic phases are capable of hosting the Quantum Hall Effect (QHE) and the Quantum Anomalous Hall Effect (QAHE). Both of these phenomena are variations of the classic Hall effect, wherein a longitudinal current along the x-axis is subjected to an orthogonal, external magnetic field $\overrightarrow{B_Z}$ along the y-axis. A Lorentz force acts on a charge carrier in the direction of the mutually-orthogonal z-axis causing an accumulation of charge that produces a transverse, z-axis electric field. The quantum nature of this effect appears when the energies of the carriers

become quantized in groups due to a functionally discrete DOS. The DOS of a topological phase produces a series of equally spaced and shaped single-peak Landau distributions. As these Landau levels are completely filled or emptied with the Fermi energy level lying between them, the Hall conductivity is necessarily quantized in proportion to e^2/h. The number of filled Landau levels is defined as the filling factor υ. The filling factor is the scalar coefficient multiplied by e^2/h to represent the total Landau level contribution to the Hall effect, in accordance with the quantized number of carriers filling a certain number of nearly-discrete levels. The QHE relies on the filling of electronic states following cyclotron orbits with variable, discretized energies. In the presence of an internal magnetic field (that is, through some magnetization $\vec{M}$), this effect becomes the QAHE. It is designated as anomalous because the internal field takes the place of the normally applied external magnetic field in the classical and quantum Hall effects.

The crystalline symmetries present within the member crystals of this group produce band structures that may host unique states such as massless Dirac electrons, magnetic skyrmions, and potentially, the elusive Majorana fermion (10–12). The selection of potential topological materials is surprisingly large and the acquisition of topological band structures is further eased by alloying compounds for more desirable behavior. Well-documented 3D stoichiometric topological compounds include binary tetradymites (Bi_2Se_3, Bi_2Te_3, Sb_2Te_3), ternary tetradymites (Bi_2Te_2S, Bi_2Te_2Se, Bi_2Se_2Te), and the focus of this dissertation: the Dirac TS Cd_3As_2 (13–15). 3D topological alloys such as $Bi_{1-x}Sb_x$ and $Bi_2Te_xSe_{3-x}$, and even some pure materials like strained α-Sn can also be tuned to exhibit desirable topological behavior (16–18). Two-Dimensional (2D) topological systems such as graphene and HgTe/CdTe quantum wells are also of considerable interest due to the appearance of the Quantum Spin Hall Effect (QSHE) within them (10,19,20).

The appearance of these new materials leads to a wealth of potential topological devices both from the incorporation of topological materials into traditional schemes and from the achievement of novel effects only made available through their unique electronic behavior. The realization of these potential devices, however, requires that the topological materials that comprise them first be synthesized with such high crystalline quality and material purity that they may even achieve the very effects which are so desired. The breaking of innate crystal symmetries such as mirror symmetry (2D systems) and rotational symmetries (3D systems) will eliminate the topological protection of otherwise unstable effects such as the QHE and QAHE. Therefore, even the minor presence of defects and impurities within a host crystal has a severe diminishing or quenching effect on what would otherwise be device-worthy material. As such, this dissertation's primary focus is on the growth of the topological semimetal Cd_3As_2 using the Ultra-High Vacuum (UHV) process of Molecular Beam Epitaxy (MBE) to achieve the highest possible quality material for future device incorporation.

1.2 The history and current state of topological materials

The exploration of these novel topological electronic classes began with the works of *Kosterlitz and Thouless* defining topological long-range order and *Thouless et al.* describing the QHE in terms of the system's TKNN invariant (3,21). For each individual electron band below the Fermi level the Berry curvature may be integrated over the entirety of the Brillouin zone, and the solutions are invariant Chern numbers. The TKNN invariant is the summation of all Chern numbers, which are equal to either zero or one in the case of either totally filled or unfilled Landau levels (22). The TKNN invariant is important in defining these topological materials because it describes the integer multiplicity of the Hall conductivity in the QHE. In other words, the TKNN invariant is equal to the filling factor υ for materials exhibiting the integer-QHE. The invariance of the TKNN value is innately linked to the structural symmetries and electronic properties of the solid-state systems that host the effect. Expanding on this phenomenon, the QAHE was first demonstrated in the topological system of Cr-doped $(Bi,Sb)_2Te_3$ by *Chang et al.* in 2013, and is of particular interest for practical devices based on the QAHE which may function without the need for an external magnetic field (23). More recently, another topological invariant "Z_2" was created to describe QSHE in 2D topological systems like those found on the surface of topological insulators (24,25). As the QHE is desired for use in conventional electronic devices, so too is the QSHE desired for novel spintronic device architectures. The use of the Z_2 invariant is analogous to the TKNN in that a nonzero value separates a topological material from the trivial insulating class. Like the QHE the conductivity of QSHE is quantized, only this time with respect to spin current instead of electron current.

As this sub-field has progressed, the potential for its applicability has become significantly wider. These quantum effects are the basis for many exciting proposed device architectures, such

as qubits with topological protection, topological memory, topological transistors, and more (26–28). Before these devices may be realized, material of sufficient quality and stability must first be produced consistently and cost-effectively. Their production therefore begins with the development of their functional topological materials. Many theoretical topological materials have already been grown, characterized, and catalogued following the initial work of their classification (1,29). In addition, *ab initio* methods such as Density-Functional Theory (DFT) have further expanded the selection of potential topological device materials to give much-needed direction regarding further synthesis efforts (30).

1.3 Cadmium arsenide and its suitability as a topological semimetal

Cd_3As_2 hosts Dirac nodes at the Fermi level in its bulk electronic band structure, and is therefore a Dirac TS. This distinction is important as a Dirac TS must have *T*-symmetry. The presence of these Dirac nodes in the bulk bands requires that the crystal adheres to the tetragonal space group $I4_1/acd$ (#142) and that it exceeds a thickness of 60-70 nm (31). This topological phase features two Dirac nodes mirrored around the Γ point on the Z-Γ-Z axis in the Brillouin zone.

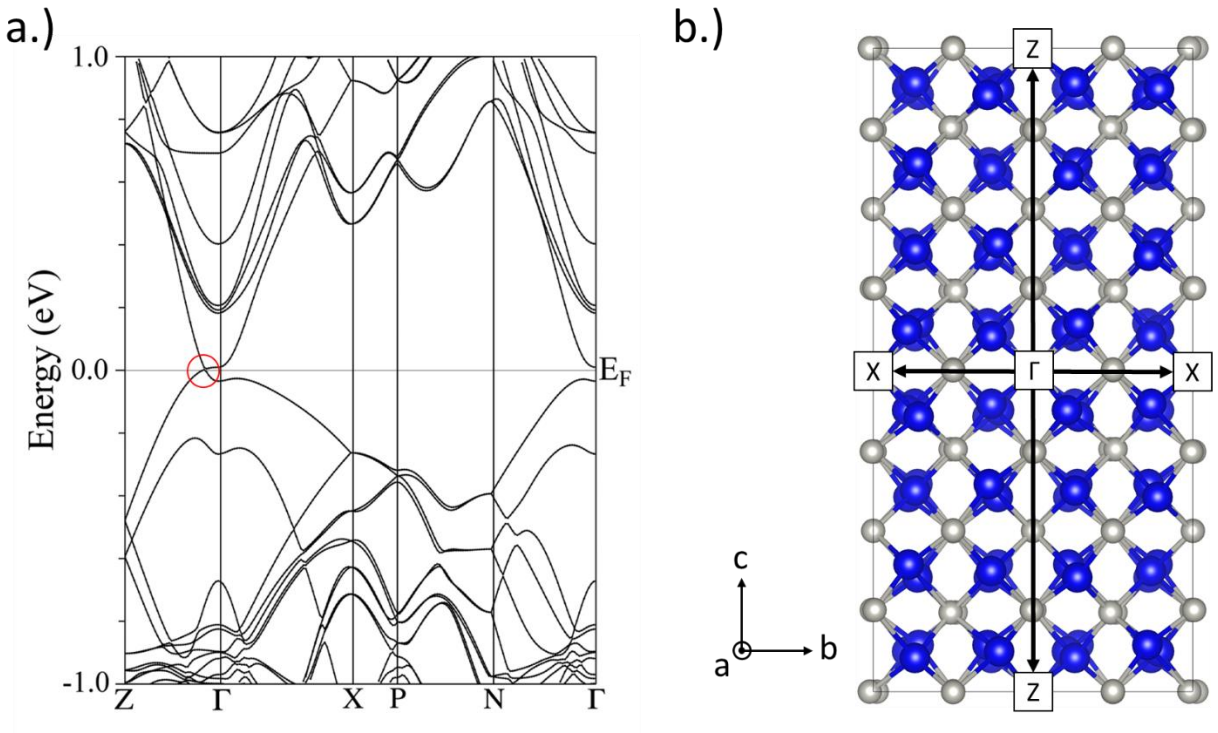

Figure 1.3: a) Theoretical band structure of the centrosymmetric $I4_1/acd$ Cd_3As_2 unit cell calculated via density functional theory with the inclusion of spin-orbit coupling (15). The Dirac node at the band inversion crossing along the Z-Γ axis is circled. b) The physical $I4_1/acd$ Cd_3As_2 unit cell axes corresponding to the labeled Brillouin zone axes in reciprocal space.

Below the thickness limit the bulk bands lose their characteristic Dirac nodes and the conduction and valence bands become gapped. This has the effect of changing Cd_3As_2 from a TS with mixed 2D and 3D carrier transport into a TI with 2D-dominated transport through the material surface. The $I4_1/acd$ space group provides both *P*-symmetry and fourfold rotational symmetry along the c-axis, which is the Z-Γ-Z axis is reciprocal space. In this phase it is composed of 16 sub-cells which follow ordering like that of an antifluorite unit cell with As on the Face-Centered Cubic (FCC) lattice and Cd in the tetrahedral interstices. However, the compound must allow two Cd vacancies per antifluorite-like sub-cell in order to maintain charge neutrality according to its stoichiometry. These Cd vacancies are ordered following a 4_1 screw axis along the unit cell c-axis, pulling the existing atoms off of their cubic-like site coordinates and producing a tetragonal 160-atom unit cell. The resultant unit cell's a lattice parameter is 12.633 Å and its c lattice parameter is 25.428 Å (15). Cd_3As_2 is a Dirac TS because it has a centrosymmetric unit cell, although its growth parameters may easily be tuned to produce slightly non-centrosymmetric atomic positions as in Figure 1.4. This breaks *P*-symmetry and causes the lifting of its Weyl node degeneracy (15,32).

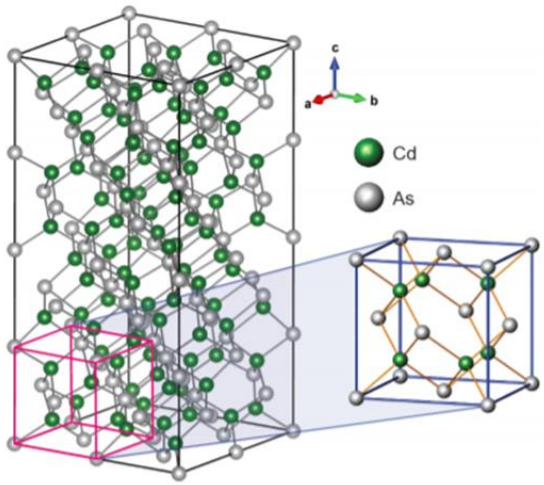

Figure 1.4: Centrosymmetric $I4_1/acd$ unit cell for the Dirac topological semimetal Cd_3As_2. It is composed of sixteen antifluorite-like sub-cells with two ordered Cd vacancies each (33).

The electronic properties of Cd_3As_2 are well-suited for conventional device purposes. For example, bulk Cd_3As_2 crystals are reported to have an electron mobility exceeding 4×10^4 $cm^2/V\bullet s$ at 130 K with the potential to achieve 10^5 $cm^2/V\bullet s$ at 4.2 K (34,35). This is large compared to traditional single-crystal semiconductors such as Si (~1,400 $cm^2/V\bullet s$) and III-Vs such as GaAs (~8,500 $cm^2/V\bullet s$) at room temperature, although it does not approach the highest values in the tens of millions belonging to 2D electron gases like those hosted within GaAs/AlGaAs heterostructures (4.7×10^7 $cm^2/V\bullet s$) (36,37). It has a high carrier density relative to traditional semiconductors, with literature values in the 10^{16}-10^{19} cm^{-3} range (33,35,38,39).

MBE of Cd_3As_2 thus far has targeted its epitaxial growth on both $\{001\}$ and $\{111\}$-type cubic substrates, with crystals being lattice-mismatched with their substrates (40,41). This produces thin Cd_3As_2 films with basal-plane (001) and pseudohexagonal $\{112\}$ orientations with respect to the substrate normal. Interfacial strain due to lattice mismatch between a topological material and its substrate will lead to different band behavior as opposed to the bulk topological material case. DFT of basal-plane Cd_3As_2 suggests that even a small increase in the in-plane a lattice parameter, such as through biaxial stress due to interfacial mismatch, will cause a crystalline phase change which removes *P* symmetry from the unit cell (32). The topological phase-change effect of strain is well illustrated in the case of α-Sn "stanine" where interfacial strain is purposefully applied to engineer topological behavior in what is otherwise a trivial material (18). The choice of thin film orientation has implications beyond lattice matching as well. For example, the pseudohexagonal $\{112\}$ orientation of Cd_3As_2 allows for the separate measurement of either of the two c-axis Dirac nodes, such as through the technique of angle-resolved photo-electron spectroscopy (33). The (001) orientation is the focus of this dissertation, as it may be lattice-matched in plane with a (001)-oriented cubic substrate to avoid strain-induced surface band

structure modification. In contrast, the {112}/{111} epitaxial heterostructure scheme cannot be lattice matched at the interface because the c/a ratio of the tetragonal Cd_3As_2 cell is not exactly equal to two and therefore the atomic positions do not exactly follow hexagonal symmetry. In addition, the Cd atoms are pulled off what would be low-fraction coordinates due to the presence of the ordered Cd vacancies, which further increases the shape mismatch with the perfect {111} hexagonal arrangement. As such, the basal-plane growth of pure Cd_3As_2 is the key to the characterization of its inherent topological properties in the absence of interface-derived strain.

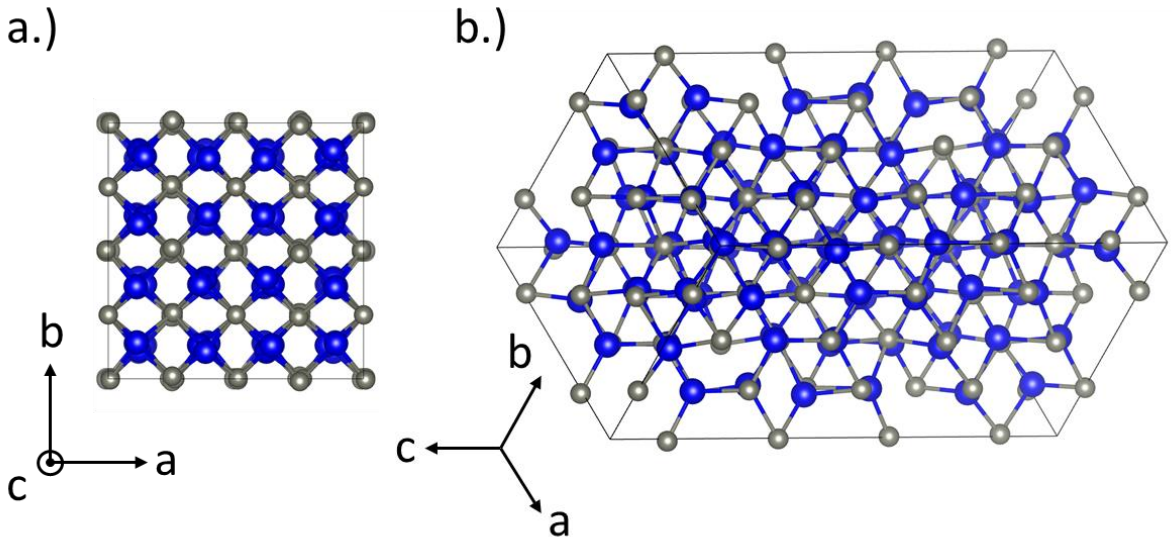

Figure 1.5: Cd atoms (blue) and As atoms (silver) within the a.) basal-plane (001)-type and b.) pseudohexagonal {112}-type orientations of the Dirac topological semimetal Cd_3As_2. The labeled axes correspond to those of the cubic substrate.

1.4 Motivation for topological materials

The ultimate purpose of the research presented in this dissertation is to produce device-worthy Cd_3As_2 thin films, both in their pure states and with a magnetic component derived either from magnetic alloying or through the magnetic proximity effect. Applicable devices include but are not limited to Magnetic Topological Memory (MTM), Topological Magnetoelectric Transistors (TMETs), and topological qubits (42–45). These proposed architectures seek to solve conventional problems such as data storage and current/voltage regulation using novel topological physics, but have so far been limited by the availability of experimentally realized topological systems. Specifically, these proposals rely on the use of magnetically-affected TIs and/or TSs which exhibit the QAHE as a result of broken *T* symmetry.

For example, the proposed MTM architecture in Figure 1.6 uses a change in the permanent magnetization vector of the magnetic topological layer or magnetic proximal layer in its heterostructure to augment its quantized Hall measurement, and therefore the memory state readout (42). High SOC in TIs promotes large coupling between the magnetization and surface states of the topological material. This scheme also requires good control of the Fermi level within the Dirac node range so that the conductivity readings remain quantized with electronic conduction being dominated by TI/TS surface states.

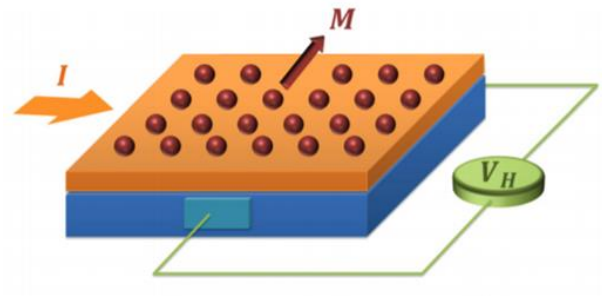

Figure 1.6: Proposed architecture for magnetic topological memory. A magnetically alloyed topological layer or ferromagnetic layer in close proximity is re-magnetized to modify the interaction with the topological semimetal surface states. This allows for the transition between low and high Hall conductivity states which may be read as binary memory states (42).

Simulated TMET architectures also rely on the QAHE, but more generally as the transition between a constant (quantized) low conductivity state and a much greater variable high conductivity state (28,43). This is achieved once again through the manipulation of the Fermi energy level via an applied gate voltage.

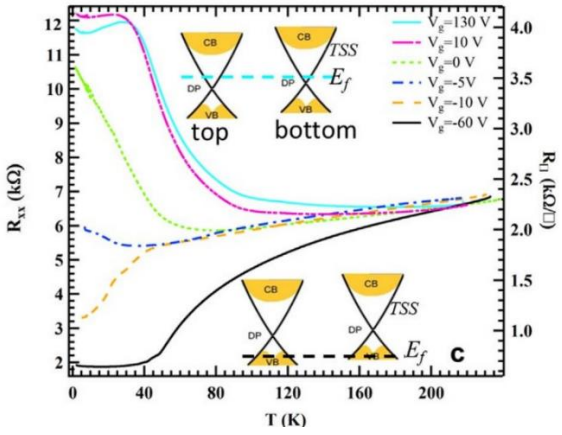

Figure 1.7: Desired electronic response for a proposed topological magnetoelectric transistor. The management of the Fermi energy level between the Dirac node range and the valence/conduction bands allows for the transition between low and high conductivity states (43).

When the Fermi energy lies within the Dirac cone and between the bulk bands, conduction will necessarily be both low due to the conduction mechanics of the surface band structure and constant due to the QAHE so long as the internal magnetization is not changed. The high conductivity state is achieved when the Fermi energy crosses into the valence/conduction band. The use of TSs over TIs here is an important distinction, as the choice dictates the electronic response of the low conductivity TMET state.

High-quality topological materials are particularly desirable for the application of topological protection to qubit-specific criteria like longer coherence times, higher fault tolerance, and the minimization of leakage (44,45). The acquisition of topological superconductors may indeed allow for the realization of topological qubits founded on the manipulation and readout of inherent Majorana bound states within the topological superconducting system.

To acquire Dirac TS Cd_3As_2 worthy of incorporation into these proposed devices, the research in this dissertation follows a series of steps to build a heterostructure that hosts the desired material as a thin film. The research goals therefore follow this heterostructure layer by layer until the topological platform is complete, as illustrated in Figure 1.8. They are:

1. To produce abrupt, metamorphic ternary III-V buffers capable of being lattice matched with a Cd_3As_2 overlayer
2. To produce Cd_3As_2 thin films with electronic properties suitable for device incorporation

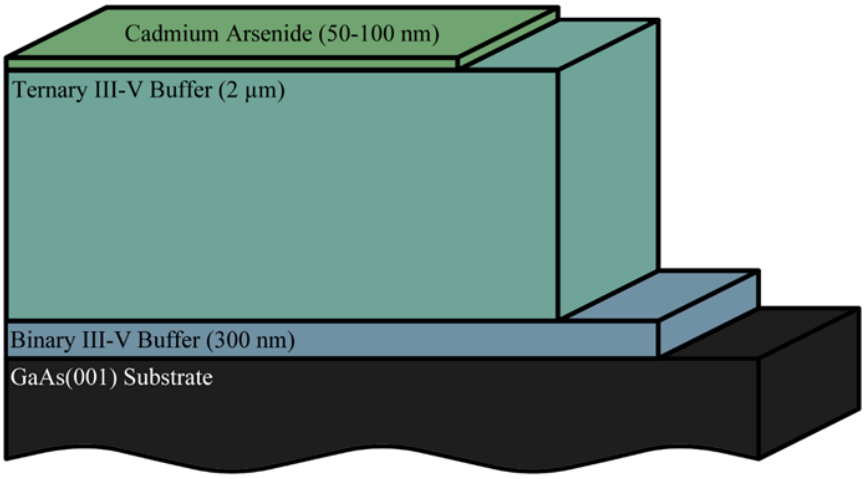

Figure 1.8: General experimental heterostructure designed for the lattice-matched growth of Dirac topological semimetal Cd_3As_2 layers.

With respect to the first goal, only three alloys composed of the available elements Al, Ga, In, As, and Sb are capable of being lattice-matched with pure Cd_3As_2. They are $Al_{47.3}In_{52.7}Sb$, $Ga_{40.7}In_{59.3}Sb$, and $InAs_{37.1}Sb_{62.9}$. They are grown on two potential binary buffers, GaAs and AlAs, to provide six unique heterostructures for comparison. These alloys are grown using MBE and are characterized *in situ* via infrared pyrometry and reflection high-energy electron diffraction. In addition, they are characterized *ex situ* via high-resolution X-ray diffraction including reciprocal space mapping, X-ray reflectivity, atomic force microscopy, cross-sectional scanning electron microscopy, and transmission electron microscopy. The material in this dissertation regarding this step is a summary of work which has already been published (46).

With respect to the second goal, Cd_3As_2 is deposited on nearly lattice-matched AlInSb, GaInSb, and InAsSb characterized using the same methods applied to the initial ternary buffer layers. The unalloyed material is additionally measured for its magnetoelectric response and the QHE via Van der Pauw geometry Hall measurements.

1.5 Requirements for thin films

Control over the interfacial strain between a Cd_3As_2 overlayer and its virtual substrate is a necessity due to its effect on the topological band structure. The presence of strain here is not actually prohibitive in acquiring the TS state as demonstrated in the growth of $\{112\}$-oriented Cd_3As_2 thin films in the literature (8,32,40,41). However, the topological nature of strain-free Cd_3As_2 thin films has yet to be demonstrated as it requires the growth of the (001)-type basal-plane on a lattice-matched virtual substrate. The lattice spacing of the As-FCC lattice along the a- and b- unit cell axes both adhere to the lattice parameter a and so can be lattice-matched with a cubic substrate. Naturally, the zinc-blende ternary III-V alloy systems are directly applied in the growth of Cd_3As_2 films to accomplish this goal. Their natural semiconducting properties, wide lattice-tuning ranges, and now-demonstrated stability at room-temperature after growth are all conducive to the high-quality growth of Cd_3As_2 overlayers. The square atomic arrangement of the ternary buffer surface interfaces with the 10-atom antifluorite-like subcell of the 160-atom Cd_3As_2 unit cell. The lattice-matched condition here is that the Group-V element lattice parameter in the ternary system should equal that of the As FCC sublattice, which is $a_{Cd3As2}/2$ = 6.3167 Å. This idealized heterostructure is illustrated in Figure 1.9. The data used to define these atomic positions is made available through the literature (15,47). The XRD characterization of subsequent Cd_3As_2 growth confirms that is indeed basal-plane growth oriented along a $[001]$-type axis.

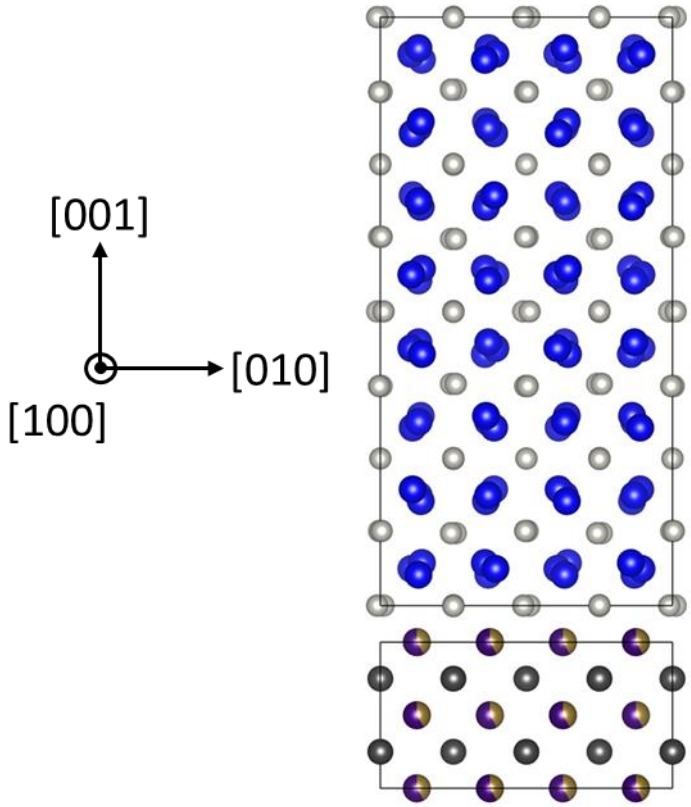

Figure 1.9: Depiction of equivalent site distances between Cd_3As_2 (above) and $Ga_{0.42}In_{0.58}Sb$ (below). Arsenic (silver) and antimony (grey) atoms share the same average spacing. Cadmium (blue) and Ga/In (gold/purple) atoms sit in tetrahedral interstices. Note that this is not a diagram of the actual experimental interface between these layers, only an idealization meant to illustrate the lattice-matched condition.

In addition to the engineering of ternary layer quality and composition targeting, the low growth temperature of TS Cd_3As_2 requires some consideration of overpressure dynamics and interlayer interactions as the substrate temperature is decreased. The shift in growth temperature between the ternary films and Cd_3As_2 is substantial, going from 440-505 °C to a range of 60-200 °C. Because the change in temperature goes below the desorptive range for the Group-V

elements (As, Sb) and into their adsorptive range, it is paramount that the overpressures applied to grow the ternary buffers and maintain their stoichiometry be removed as close as possible to the point of desorptive/adsorptive transition. Removing the pressure at too high a temperature will cause the surface to roughen as the Group-V elements desorb faster than they are replaced. Removing the pressure at too low a temperature will cause metallic Group-V elements to agglomerate on the ternary buffer surface, preventing Cd_3As_2 epitaxy or at the very least reducing its crystalline quality. In these following Cd_3As_2 growths it has become standard practice to transition from Group V overpressure to vacuum at 425 °C, although some earlier growths utilized a transition temperature of 400 °C.

The primary concerns during the growth of these films are twofold: firstly, that the high vapor pressure of Cd will prevent net-positive deposition above a certain temperature threshold and secondly, that there will be a diffusion interaction at the interface between deposited Cd_3As_2 and its chosen ternary buffer system. Note that a molecular Cd_3As_2 source is used to deposit the CdAs films in these experiments. For context, the vapor pressures of elemental source materials at common experimental temperature setpoints (base/bulk where dual-filaments cells are used) are listed in Figure 1.10 (48). The vapor pressure of Cd at 350 °C is 28 times that of As_4 and at least six decades larger than the Group-III sources.

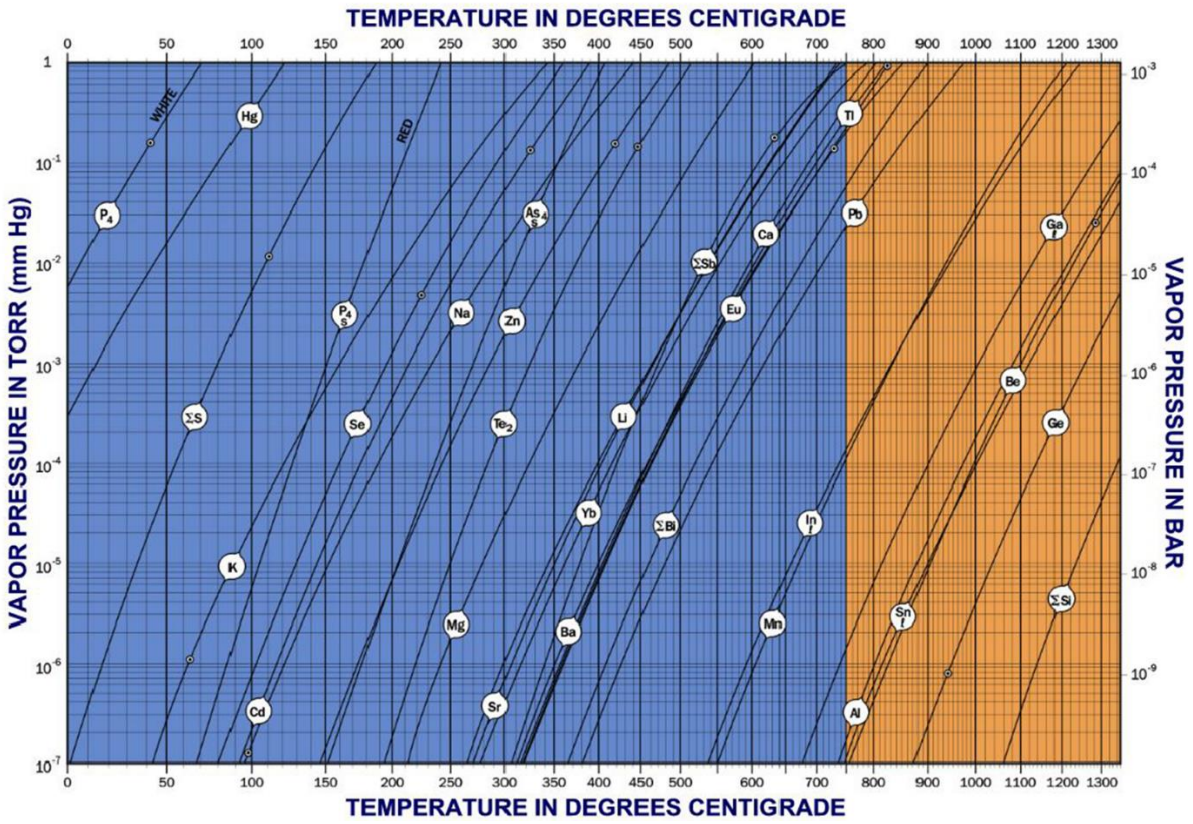

Figure 1.10: Vapor pressures of elements within the range 10^{-7} to 10^{0} Torr for temperatures acquirable using experimental Knudsen source cells (48).

To satisfy the first concern, open-cell MBE regarding Cd_3As_2 in the literature acted as an excellent starting point for the initial experimental parameters (40,41). Over the course of many growths, it was found that the lower growth rates applied using a valved effusion cell required a narrower range of 60-145 °C to produce thin films. Naturally, larger growth rates should allow for a higher temperature growth as the net deposition rate increases, but the effects of Cd_3As_2 growth under the heightened overpressure of its own desorbing film are still unknown. Thermal transfer from the molecular Cd_3As_2 flux was also considered using the effusion cell temperatures as process variables. However, once growth-worthy fluxes corresponding to BEP values in the 10^{-7} to 10^{-6}

mbar range were achieved only Cd_3As_2 cell valve position and substrate growth temperature was used to modify the Cd_3As_2 growth environment.

The second concern was satisfied through the application of Gibbs free energy calculations regarding the diffusion of Group-V elements between their applied overpressures, the three ternary buffer layers, and Cd_3As_2. In particular, these calculations consider the spontaneity of layer intermixing between Cd_3As_2 and the three potential ternary buffers both with and without the presence of Group-V overpressure. The reactions are strongly endothermic, and no evidence of alloying across the Cd_3As_2-ternary interfaces has been found in this experimentation.

Chapter 2: Experimental Procedures and Their Refinement

2.1 Molecular beam epitaxy

2.1.1 Fundamentals of MBE

MBE is a technique designed to use UHV for thin-film deposition of traditional electronic materials with minimal crystal defects and impurities. There is an extreme focus within the MBE community on the epitaxial growth of crystal thin films due to the general goals above. Beginning with notable published work in the 1960s, its major feats include the acquisition of the highest magnitude III-V semiconductor carrier mobilities as in AlGaAs/GaAs, InGaAs/InAs, and AlGaSb/InAs 2D electron gas heterostructures (37,49–51). Certain devices such as optoelectronic heterostructures for lasers, high-electron mobility transistors like those in modern cell phones, and metal-oxide-semiconductor field-effect transistors require a high minimum semiconductor mobility and good layer thickness control in order to be considered practical, and so are therefore popular commercial applications of what is otherwise a very research-focused thin film deposition technique.

MBE is founded on the use of source material evaporation through strict temperature control in low-pressure conditions. Solid source materials must be high purity (5N-7N+) to reap the full benefit of UHV to produce low contamination films. Source evaporation of metals and metalloids with sufficiently high vapor pressures in UHV generally follow the use of a Knudsen-type cell.

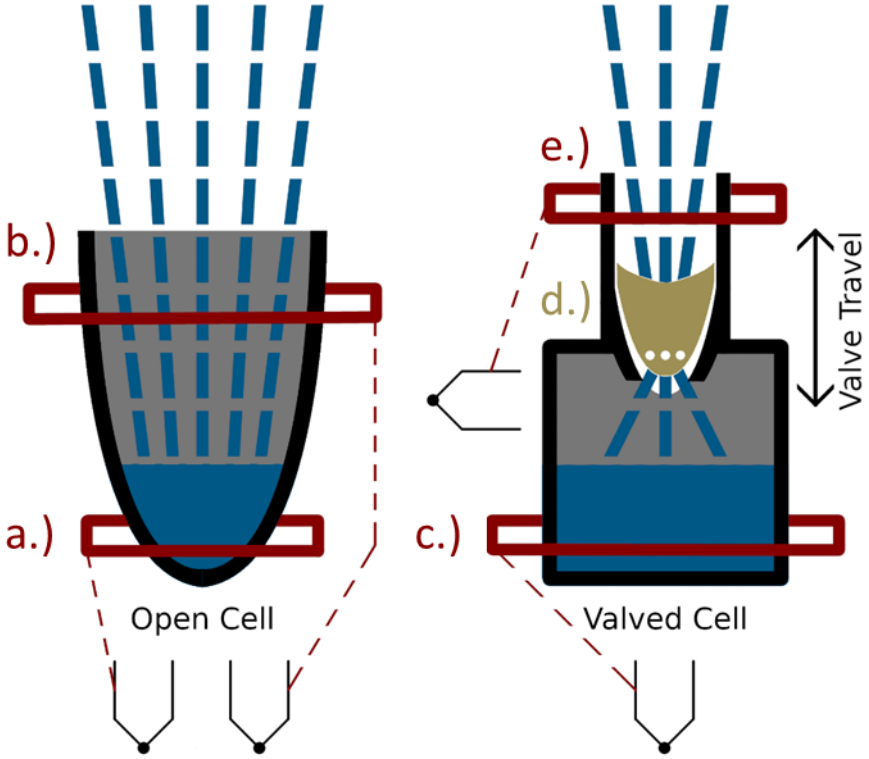

Figure 2.1: Representation of source material effusion cells used for molecular beam epitaxy in these experiments. The effusion path follows the dashed blue lines in both cases. Dashed red lines connect thermocouple connection posts to their approximate reading positions at their respective filaments. The Knudsen cell effusion rate is controlled at a minimum through a) a base-level heater element (filament). Dual-filament cells also feature b.) a tip-level filament. Valved cells control effusion rate through both c.) a bulk-material filament and d.) a porous p-BN valve. e.) Where applicable, a high-temperature thermal cracking section converts molecular source fluxes into a more reactive species.

Here, a central crucible is heated by filaments monitored by some type of temperature control, such as a proportional-integral-derivative thermal control loop. The use of a pyrolytically-grown boron-nitride crucible is standard for III-Vs due to the material's high temperature stability

and its low reactivity with Group III and V elements. A heated source cell forms a steady beam of evaporated material which follows a shape based on set geometries such as cell dimensions, nozzle dimensions, and distance to the substrate. This beam flux can be monitored by Beam-Equivalent Pressure (BEP) measurements conducted using an Ion Gauge (IG) which intersects the effused beam path and outputs a pressure corresponding to the actual source material flux. Such BEP measurements are taken over a range of filament temperatures to determine a corresponding data set which can be easily interpolated for fine control of layer growth rate and thickness, alloy composition, and ultimately film crystallinity. BEP measurements conducted within this dissertation follow polynomial fittings for valve-position setpoints and Arrhenius-type log fitting for open cell temperature setpoints. MBE effusion cells may either be single or dual-filament according to the specific requirements of their held source material.

Source material within an open effusion cell may be heated using a dual-filament setup to keep the cell tip temperature 100-200 °C hotter than the cell base, a feat only made possible through lowered thermal transfer within the UHV environment. This prevents the accumulation of source material on the Ga and In effusion cell tips over time to eliminate spitting of cooled droplets, which otherwise contact the substrate during growth and create nanometer-sized film defects. The Al effusion cell is single-filament with a cold tip as the Al source material tends to migrate beyond the cell opening once the temperature has exceeded the melting point of 660.3 °C. This migration of liquid Al may cause premature cell failure if not prevented. Closed, valved cell types like those belonging to As, Sb, and Cd_3As_2 are dual-filament to prevent the accumulation of material around their very narrow valve openings. The bulk filament temperature provides coarse beam flux control according to the exponential increase in effusion rate with respect to absolute temperature. Changes in valve opening (positive position) allow for finer control of source flux with a

relationship that is well approximated by a polynomial fit of BEP vs. position. In addition, the dual-filament setup is a necessity for the As and Sb cells which use a cracker section to split their nominally effused tetramers (4-atom) into dimers (2-atom) before the source beams make contact with the substrate. These cracker zones operate at much higher temperatures (900-950 °C) than the bulk filament setpoints required for significant effusion (390-610 °C).

A general schematic of the reactor source positions and the corresponding confocal atomic beam setup is shown below in Figure 2.2. The angles of the source beams range from nearly horizontal to a 22° rotation from vertical. The angle of the source cell is an important consideration in determining the maximum allowable charge before spillage due to gravity. This is a particular danger in the case of the open effusion cells used for Al, Ga, In, and initially CdAs, which is why their steeper angle configuration is favorable.

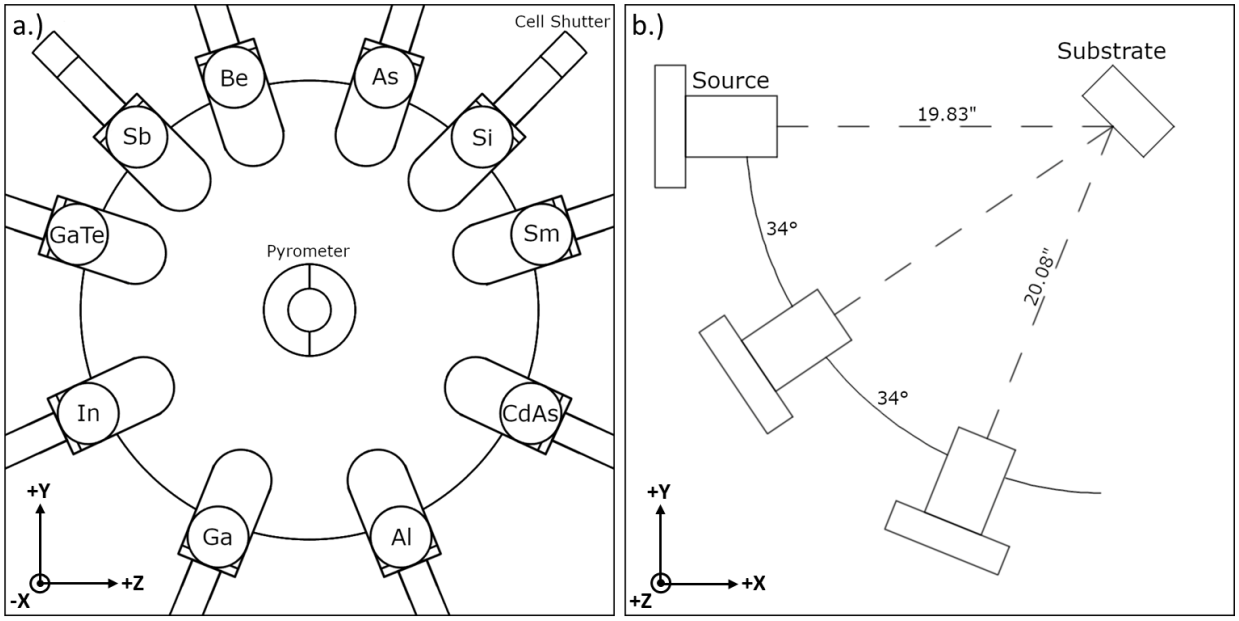

Figure 2.2: a.) Schematic of the molecular beam epitaxy reactor source flange with cell orientations and b.) their confocal paths meeting at the substrate manipulator.

MBE is a thin film growth technique limited by source evaporation rate and thermal processes on the substrate. Many variables are considered to ensure that source materials sufficiently interact with a given substrate for proper crystal growth. These include reactor geometry, substrate temperature, substrate rotation speed, source temperatures and their BEP values, reactor pressure, UHV contamination, and more. The reactor used here is an Applied EPI 1040 hosting ten source material ports with beams that meet at a confocal point on the substrate surface. The reactor possesses a substrate manipulator which can hold custom 2" and 3" wafer uniblocks. While MBE substrates may be conductively heated through an internal heating element and metal contacts (such as tantalum), this reactor and many modern counterparts utilize a radiative heating element which applies a high-intensity infrared flux to the substrate to manage heating and cooling during thin film growth. Sample rotation speed is controlled by an external, magnetically coupled motor which may reach rotational speeds of 60 RPM. This rotation is an important part of keeping MBE-grown films even across the substrate surface with respect to its rotational angle, although films still tend to be thicker at their centers by a few percent when compared with their edges. The use of a valved cell for the MBE of Cd_3As_2 is relatively new. Such a valved molecular source cell was employed to overcome initial difficulties in depositing Cd_3As_2 using an open effusion cell. With an open Knudsen cell setup, the high vapor pressure of Cd caused Cd_3As_2 source material to effuse at a rate suitable for MBE even as low as 300 °C, which provided less flux control during temperature setpoint changes.

The kinetic and thermodynamic interactions between an atomic/molecular source beam and a crystalline substrate follow a general pathway with each step corresponding to some probability of further interaction (and necessarily, a probability of removal from the interacting system). During this process an atom/molecule (i.e., a species) may engage in weak van der Waals

interaction with the substrate (physisorption), chemical bonding with the substrate (chemisorption), and incorporation into the substrate crystal according to its symmetry/charge neutrality-defined site ordering.

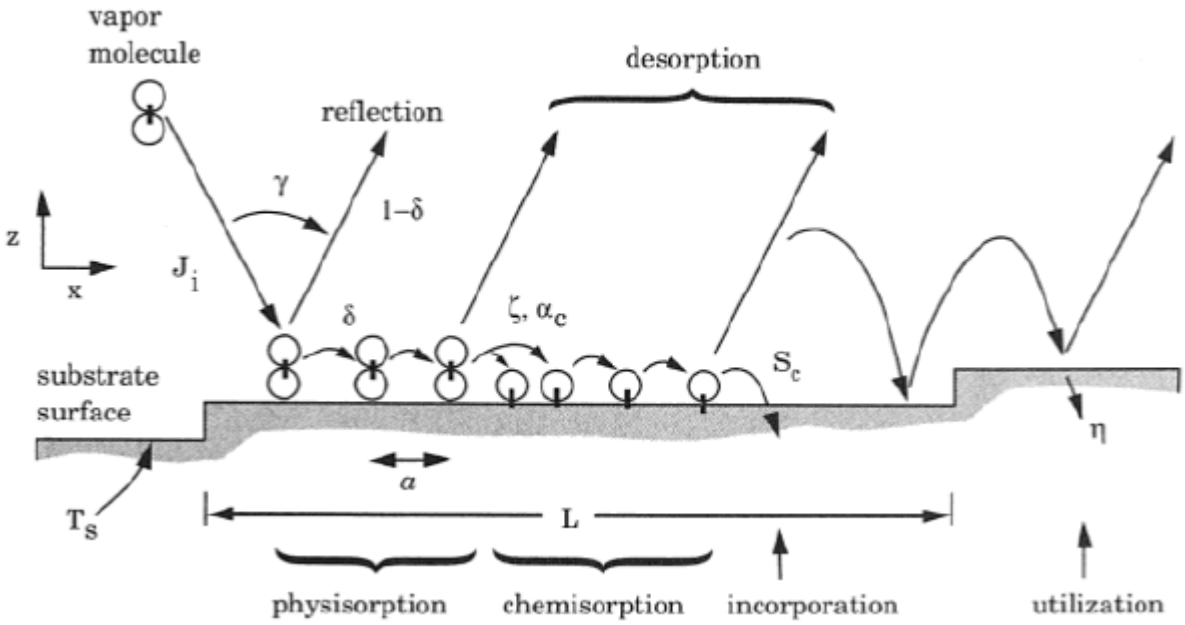

Figure 2.3: Diagram of local thin film growth using a molecular beam such as As_2. The steps of physisorption, chemisorption, and incorporation are illustrated on one crystal terrace (52).

The steps are generally as follows: 1.) An impinging beam species contacts the substrate and either reflects back into the chamber or physisorbs, 2.) the species either thermally desorbs from the surface or chemisorbs onto the substrate, and 3.) the species either thermally desorbs from the surface (now after chemisorption instead of physisorption) or is incorporated into the correct atomic site(s) following the lowest Gibbs free energy atomic ordering as a function of its epitaxy on a specific crystal (52). Each of these steps has at least one quantifiable probability associated with further interaction, all of which contribute to the final fraction of atoms taken from the

impinging beam flux and incorporated during thin film growth. Figure 2.3 shows a diagram of these steps in order from left to right. This picture is accurate in the case that the rate of incorporation exceeds the rate of desorbing, incorporated atoms. The rate of desorption is mediated by the vapor pressure P of the substrate crystal and the absolute temperature T of the substrate, according to the Clausius-Clapeyron equation:

$$\frac{dP}{dT} = \frac{\Delta H_{vap}}{T(V_g - V_s)}. \tag{2.1}$$

Other terms include the enthalpy of vaporization ΔH_{vap} and the molar volumes of the gas V_g and liquid/solid source V_s. If $V_g \gg V_s$, the vapor acts as an ideal gas. In this case and if ΔH_{vap} changes negligibly with respect to T, the relationship may be further reduced to the familiar equation used for BEP setpoint changes in these experiments:

$$\ln P = coefficient * \frac{\Delta H_{vap}}{RT} + constant. \tag{2.2}$$

Amongst these growth probabilities is the sticking coefficient, which is the probability of a chemisorbed species incorporating into a thin film. It is an extremely important consideration for alloy targeting and determining specific growth conditions such as the sufficient Group-V overpressure for good semiconductor growth. It is a factor in heterostructure layer growth times and calculating relative beam fluxes for alloy targeting. For example, differences in sticking coefficients amongst the Group-V elements will cause a ternary alloy to drift from its target composition if not accounted for. The same would be true for the Group-III elements if not for the fact that their sticking coefficients are near unity at the experimental growth temperatures and

Group-V overpressures. Many factors influence the sticking coefficient of a material beam including the crucible temperature, the atomic flux magnitude, and the effused atom/molecule. Note that Group-V fluxes (As & Sb) adsorb as a molecular species before bonding to the host crystal, further complicating sticking probability considerations.

Pure As and Sb sublimate as the tetramers As_4 and Sb_4 at temperatures sufficient for reasonable MBE growth rates (390 °C and 610 °C respectively). These tetramers, however, possess approximately half the sticking coefficient of their dimers As_2 and Sb_2 at temperatures used in these growths (53–56). For example, the sticking coefficient of Sb_4 is approximately one-half when interacting with a GaAs (001) substrate above 375 °C. In contrast, the sticking coefficient of Sb_2 is unity above 325 °C, even when growing under two concurrent Group-V overpressures (Sb_2 & As_2). This sticking coefficient doubling effect is attributed to the surface interaction between the Group-V flux and the substrate requiring that tetramers split into dimers before chemisorbing onto open sites. As such, material crackers are heated to much higher temperatures (900 °C for As_2 and 950 °C for Sb_2) to provide source beams with more desirable surface interactions. The lower bulk zone temperature setpoints ensure that source material is not effused out at an unnecessary rate.

The arrival of atoms at the substrate surface may be quantified through the use of BEP measurements. While more accurate in the case of Group-III element competition, these calculations are necessary for all three experimental ternary alloy systems as their atomic fluxes must be tuned between samples to precisely acquire the compositions which are lattice-matched to the in-plane Cd_3As_2 lattice parameter $a_{CdAs} = 12.633$ Å. Linearly interpolating the ternary system lattice parameters using Vegard's law, the corresponding lattice-matched alloys with $2a_{ternary}$ = 12.633 Å are $Al_{47.3}In_{52.7}Sb$, $Ga_{40.7}In_{59.3}Sb$, and $InAs_{37.1}Sb_{62.9}$ (57). The Group-III source beams are generated by open effusion cells, so relative flux tuning is done through

modification of individual temperature setpoints. The BEP measurements for these cells are used to determine the atomic flux ratio J_x/J_y required to achieve a specific composition (58).

$$\frac{J_x}{J_y} = \left(\frac{P_x \eta_y}{P_y \eta_x}\right) \sqrt{\frac{(T_x M_y)}{(T_y M_x)}} \tag{2.3}$$

However, the sensitivity of the IGs used in BEP measurements varies with the ionization efficiency η_i, temperature T, and molecular weight M_i of the species of source atom or molecule. The ionization efficiency is defined in reference to the known ionization efficiency of N_2 which is $\eta(N_2)$ and the atomic number of the source material species Z_i.

$$\frac{\eta_i}{\eta(N_2)} = \left[\left(\frac{0.6 Z_i}{14}\right) + 0.4\right] \tag{2.4}$$

The ionization efficiency ratio scales linearly with atomic number, so that significantly more In flux is required for the same BEP measurement as a corresponding Ga beam, and likewise for Ga flux compared to Al flux.

During these experiments a Cd_3As_2 open cell setpoint range of 225-350 °C was found to cover BEP values up to 1.14×10^{-5} mbar. For comparison, MBE recipes for In, Ga, and Al targeting equivalent BEP values require a much higher base cell filament setpoint (950-1175 °C) to even achieve values on the order of 10^{-6} mbar. In addition, the fast rise in the open Cd_3As_2 cell effusion rate with respect to temperature is such that the BEP remains within the desired 10^{-6}-10^{-5} mbar range only over base filament setpoints of approximately 300-350 °C. Because even a fraction of a °C here has such a large effect in terms of final Cd_3As_2 layer growth rate, an E-Science 50 ULT Titan valved effusion cell with a graphite crucible was installed for greater control of atomic flux.

Higher filament setpoints are employed with the base temperature set to 400 °C and the tip temperature set to 500 °C. The flux associated with a valve position is unique to the cell geometry and so is not generally applicable, but for this particular setup a good range for Cd_3As_2 growth is a valve opening of 100-125 mils for a BEP on the order of 10^{-6} mbar.

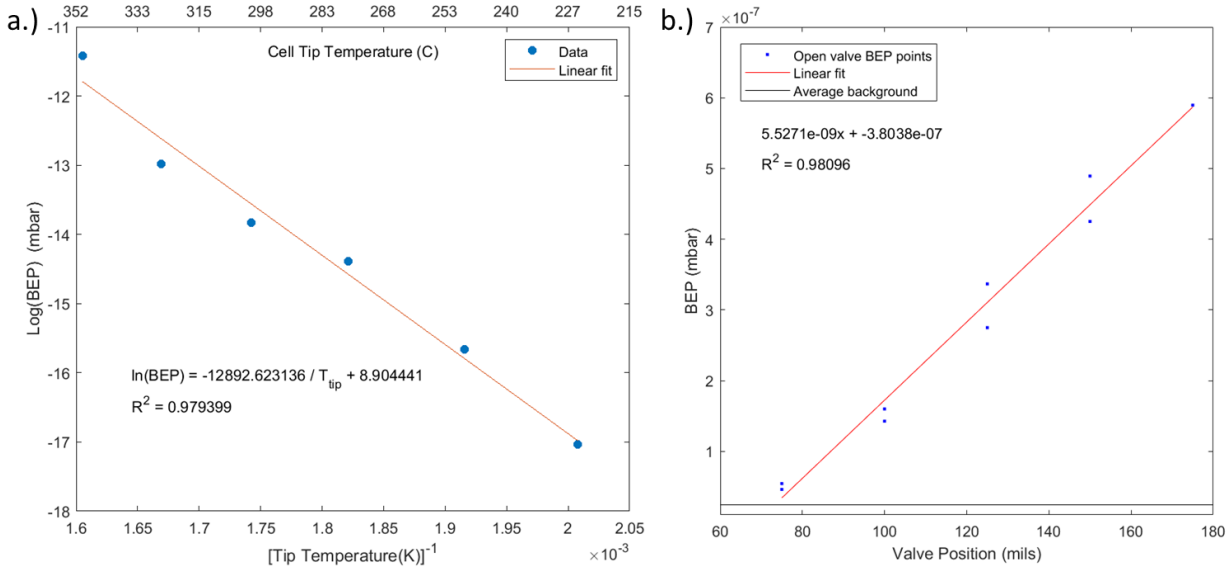

Figure 2.4: Comparison of beam-equivalent pressure measurements for a.) the open Cd_3As_2 effusion cell with respect to temperature and b.) the valved Cd_3As_2 effusion cell with respect to valve position. The data in a.) is plotted according to the Arrhenius relationship which is well fit by a linear trendline. The data in b.) is fit with a linear polynomial used to practically estimate Cd_3As_2 beam-equivalent pressure as a function of valve position.

2.1.2 General MBE process

The general process for MBE conducted in this research follows the series of steps outlined in Figure 2.5: substrate heating and As_2 overpressure switchover, native GaAs substrate oxide desorption, homomorphic/pseudomorphic binary buffer growth, ternary layer growth, Cd_3As_2 growth where applicable, substrate cooling, and UHV switchover. The substrate temperature is measured via in situ pyrometry for all steps except 10, which uses the substrate manipulator thermocouple for reference.

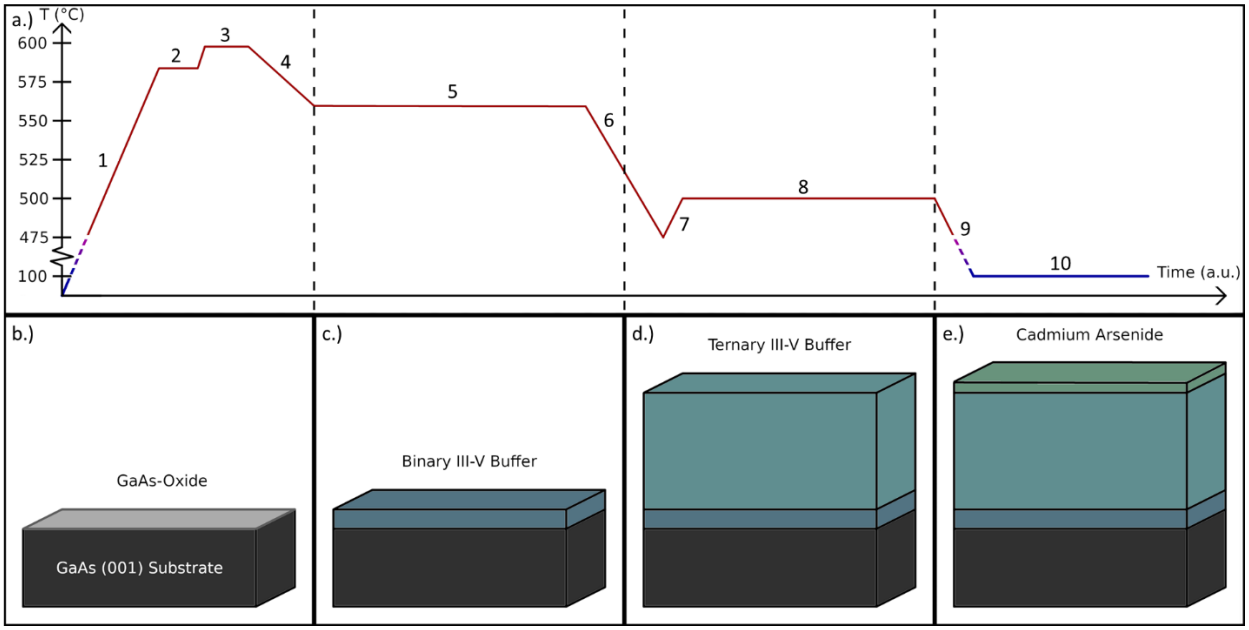

Figure 2.5: General growth flow for experimental samples. The substrate temperature in a.) progresses through substrate preparation and heterostructure growth. Steps 1-4 in b.) follow the initial heat up, GaAs oxide desorption, and cooldown to the binary III-V growth temperature. Steps 5-6 in c.) follow the growth of the binary III-V and cooldown to a lower ternary III-V starting growth temperature. Steps 7-8 in d.) follow the nucleation and growth of the ternary buffer. Steps 9-10 in e.) follow cooldown to 60-200 °C and subsequent Cd_3As_2 growth.

The native GaAs oxide desorption occurs *in vacuo* at a maximum literature value of 583 °C (59). Regarding deoxidation, experimental GaAs (001) substrates are held at 583 °C under As_2 overpressure for ten minutes before an additional ten-minute soak around 598 °C to ensure that the native oxide has been completely eliminated. Higher soak temperatures risk roughening the GaAs (001) surface due to net As desorption at the same As_2 overpressure, and so longer desorptive soaks at lower temperatures are preferred. GaAs and AlAs binary buffers are grown at 560 °C targeting thicknesses of 300 nm. Their primary function is to reduce the number of threading dislocations at the interface with a ternary III-V alloy overlayer by burying contaminants and defects on the substrate surface. The ternary III-V alloy buffers are grown over a lower range of temperatures from 440 °C to 500 °C. The thicknesses of these layers target 2 μm so to further minimize the threading dislocation density at their surfaces. There is a general jump in pyrometer temperature during ternary III-V nucleation as illustrated by step 7. This is due to an increase in radiative heating efficiency from the substrate manipulator heater as the optical band gaps of all three lattice-matched ternary alloys are lower than either of the binary III-V arsenide buffers. Each of these growth steps are pre-programmed and activated through the process control software "Molly 2000," wherein specific temperatures, times, and step activation criteria are defined to better automate the growth process. Temperatures used to control process steps above 400 °C are measured via a pyrometer set to monitor the substrate manipulator in its growth position. Lower setpoints use the substrate manipulator thermocouple reading.

Because the commercial GaAs (001) 2" and 3" wafers used for growth are cleaned before packaging they are considered epitaxy-ready and are not further treated before sample growth. Before MBE can occur at higher temperatures, the GaAs substrate must be stabilized under As_2 overpressure to ensure good epitaxial overlayer growth. There is a specific transition temperature

range where exposure to As_2 overpressure will change from causing a net accumulation (adsorption) of metallic As on the substrate surface to allowing for the stabilization of the substrate with excess surface As desorbing from the hot substrate. Because oxide desorption and III-V layer growth occurs within the desorptive range, this transition range is only crossed twice per sample during initial heating and final cooldown before any Cd_3As_2 growth. It is generally 400-450 °C for the experimental growths. A lower As_2 overpressure introduction setpoint of 350 °C is applied during initial heating since excess As is desorbed once the transition range is crossed.

2.1.3 Reflection high energy electron diffraction

Reflection High Energy Electron Diffraction (RHEED) is conducted *in situ* to monitor the surface quality of layers during growth and in between steps. The UHV environment is suitable for electron beam diffraction, making *in situ* RHEED applicable. Specific growth step failures can be identified through comparison of RHEED patterns in tandem with reactor pressure data and *in situ* pyrometry. In the experimental setup, an electron beam is generated from a 1.5-1.6 A tungsten filament current under a 15 kV acceleration voltage. The beam meets the substrate at a glancing angle with the diffracted beam projecting onto a phosphor screen.

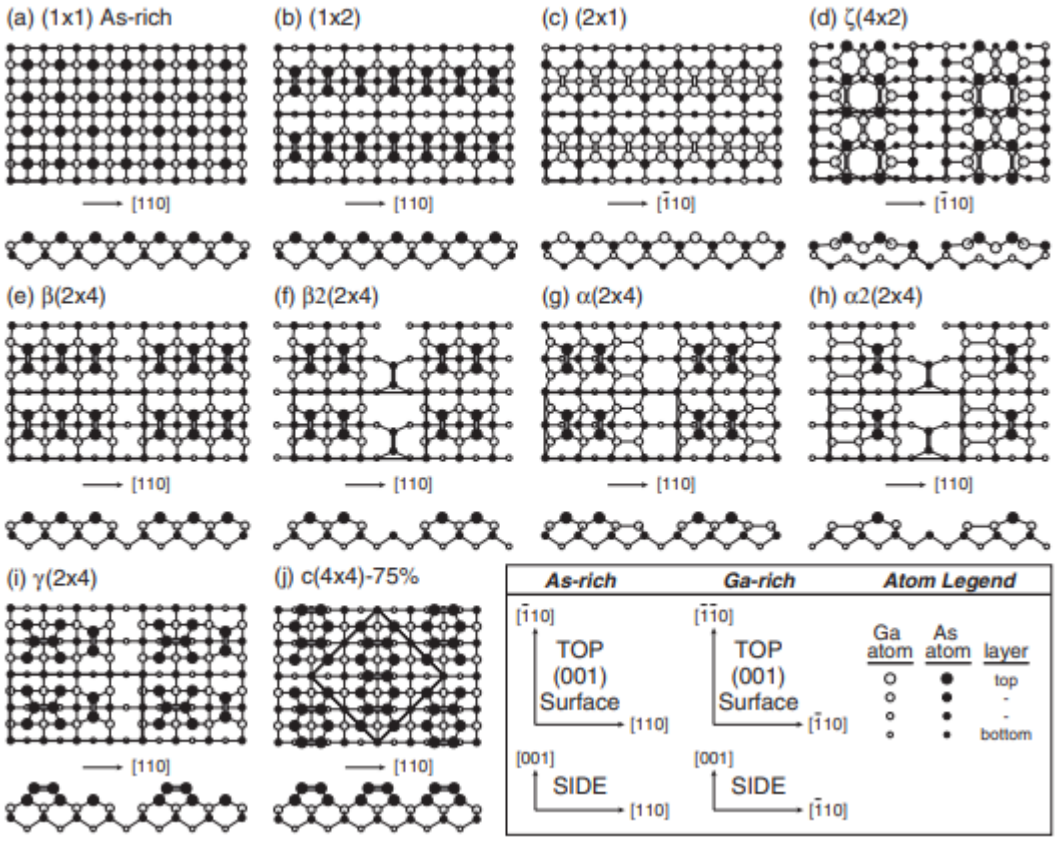

Figure 2.6: GaAs (001) surface reconstructions during homomorphic growth. (c) and (d) are Ga-rich growth conditions and the rest are As-rich conditions (60).

The spacing of the reciprocal lattice rods produced by the single-crystalline topmost atomic layers allows for an excellent measure of surface crystal quality during growth. The surface reconstruction of atoms with respect to layer rotation are also derived from these RHEED images, providing further data for consideration of the deviation from the ideal epitaxial growth condition. For example, the GaAs buffers grown in these experiments reliably produce RHEED patterns with (2×4) multiplicity corresponding to surface atoms which are twice and four times the normal lattice spacing apart. This is in line with literature that suggests that the β2 (2×4) structure is the most energetically favorable structure for growths near these experimental temperatures and Group-V overpressures (61). Diagonal lines in these images are Kikuchi lines, which are useful in aligning the substrate with the RHEED gun's electron beam. RHEED images of 0° and 90° sample rotations are of particular interest due to the fourfold in-plane symmetry of the cubic III-V and tetragonal Cd_3As_2 layers produced as part of this research. These high-symmetry angles can be identified by the presence of reciprocal lattice rods (i.e. streaks) with consistent multiplicity. In Figure 2.7, the red and blue markers indicate major and minor streaks. Note that the major marker spacing is the same for both rotations, as it corresponds to the in-plane atomic spacing $\sqrt{2}a$ for both $\langle 110 \rangle$-type high-symmetry directions.

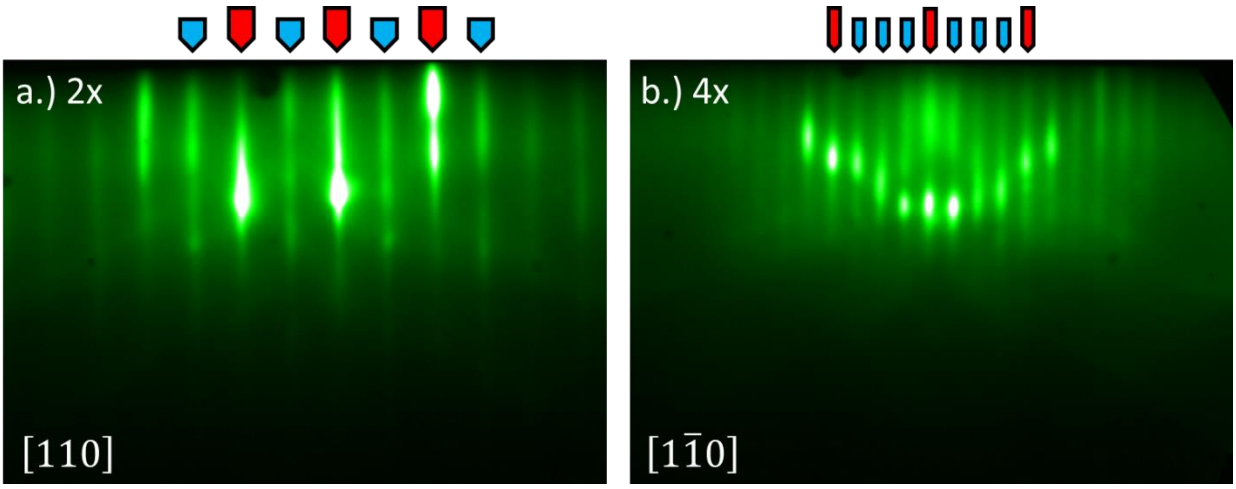

Figure 2.7: Representative reflection high energy electron diffraction images of GaAs grown homomorphically on a GaAs (001) substrate. Subplots a) and b) show 90° rotations of the high-symmetry ⟨110⟩-type direction patterns for the zinc blende structure.

2.1.4 Infrared pyrometry

Pyrometry is a fast optical measurement which may be used to more accurately determine the temperature of an MBE film/substrate during growth in comparison to the substrate heater thermocouple reading. As such, this *in situ* technique is applied constantly during all experimental growths and provides a process variable by which certain growth steps are activated and deactivated. Following common practice, the pyrometer is calibrated according to the GaAs oxide desorption temperature of 583 °C. The oxide desorption causes a clear change in RHEED image contrast within seconds of reaching the correct temperature.

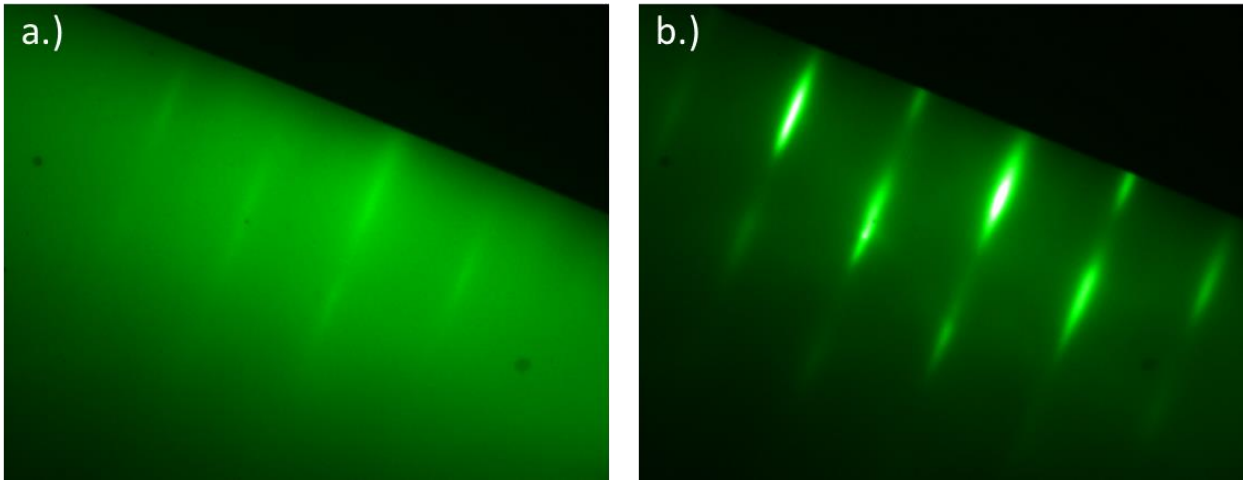

Figure 2.8: Representative reflection high energy electron diffraction image of GaAs a.) before and b.) after its native oxide has desorbed at a pyrometer temperature of 583 °C. These images correspond to the same sample rotation.

The emissivity coefficient of the pyrometry module is adjusted so that its reading equals 583 °C at the point where the GaAs oxide's removal causes a (2×4) surface reconstruction to appear clearly. The current pyrometer is only accurate in the mid-to-high temperature range ($T \geq 400$ °C), and so

the substrate heater thermocouple is still used for low temperature transitions like the addition of As_2 overpressure at 350 °C during the initial GaAs substrate deoxidation step.

Despite the pyrometer's utility, certain considerations must be taken into account when analyzing pyrometry data and when using it for automation. The emissivity of the substrate is a pyrometry parameter calibrated for smooth III-V layers in the experimental temperature ranges. As a result, significant increases in surface roughness will raise the pyrometer reading as the emissivity scales proportionally to the increase in emissive surface area. High surface roughening occurs in the case of InSb melting and subsequent phase separation during improper GaInSb, AlInSb, and InAsSb alloy growth because it creates many new phase domains which preferentially nucleate near the sample surface where minimal phase-separation driven stress exists (62). This removes the pyrometer as an accurate measure of temperature and disrupts any further automated recipe steps which rely on this accuracy to transition between growth steps at specific substrate temperature setpoints. Constructive/destructive interference of infrared wavelengths caused by the thin film over initial growth thicknesses also produces pyrometer temperature oscillations, as reported previously in the literature (63). This has, so far, has occurred to a lesser extent such that it has not required mid-growth substrate thermocouple setpoint modification to maintain the desired pyrometer temperature. These growth-interference oscillations are most pronounced in AlInSb, followed by GaInSb and then InAsSb.

Several equipment contributions also had to be considered during pyrometer calibration and usage: mainly those which produce significant deviations in the signal. These factors generally fall into the categories of infrared-emitting parts and substrate emissivity-modifying parts. Amongst the first category lies every component which emits significant infrared radiation in accordance with high temperature setpoints, such as the substrate and substrate manipulator (the

intended target for measurement), the source cells, the growth chamber, the growth BEP IGs, and the pyrometer viewport heater. The opening and closing of source shutters have generally not corresponded with immediate changes in pyrometer signal during these experiments. The growth chamber IGs generally do not interfere with substrate pyrometry, which may be attributed to their geometries with respect to the substrate manipulator. The distant, offset position of the growth chamber IG is contrasted by the growth BEP IG which is lowered in line with the confocal source beams during its operation. When active, its effect on the pyrometer is something like a positive 150-200 °C jump in readout. Fortunately, this effect does not impact system operation as calibration and growth procedures are conducted separately. The final emitting component, the pyrometer viewport heater, was found to significantly alter the pyrometer reading during normal growth operations. Its direct path to the substrate manipulator may be the source of its increased contribution. The power supplied to the viewport heater therefore had to be limited to 15 W (approx. 300-350 °C window temperature) during growth in order to prevent an inaccurate pyrometer calibration leading to consistent growth failures.

The second category of pyrometer-modifying conditions considers the position, angle, and rotation speed of the substrate manipulator. The substrate manipulator position has moved very rarely over the course of these experiments, but certain maintenance activities such as the replacement of the heater element have moved both the position of the substrate holder and the angle of the heater assembly cylinder. These small deviations are accounted for through re-calibration of the pyrometer, as they affect the geometry seen by the radiation emitted by a hot substrate. As the substrate is rotated during growth it lowers the pyrometer signal by about 5 °C. This could be a result of more even heating/cooling of the substrate or variations in the infrared

signal from hot effusion cells. Pyrometer calibration is done with substrate rotation set to 60 RPM to account for these variations during normal growth.

The final contribution, sample emissivity, is a materials property which affects the blackbody radiation spectrum of a sample as it is heated within substrate manipulator. The GaAs wafers used in these experiments are either semiconducting Si-doped (earlier experiments) or semi-insulating undoped (later experiments). An interesting effect with regard to the doping level is that is that the bulk properties of the GaAs wafer appear to primarily mediate the emissivity of the wafer. In practice, both wafer types have been interchanged under the same emissivity calibration without causing growth setpoint issues. The major consequence of using undoped wafers in later experiments is that the substrate heater output had to be increased to achieve the same pyrometer temperatures, an effect attributed to the loss of free carrier heating caused by a significant impurity level decrease from that of the Si-doped substrates.

2.2 X-ray methods

2.2.1 High-resolution X-ray diffraction

X-Ray Diffraction (XRD) was conducted using a PANalytical X'Pert Pro MRD system. The general setup of a diffraction experiment is shown in Figure 2.9. This system is configured to emit a Cu-Kα beam from a 45 kV, 40 mA source which is passed through a four-bounce hybrid Ge (220) monochromator. The angular cutoff of incident beam is narrowed via a 1/4° acceptance angle incident slit before contacting the sample surface. The diffracted intensities were measured using either a triple-axis detector or a 256 channel PANalytical PIXcel3D unit with over 65,000 (256^2) solid-state pixels. The PIXcel3D detector is capable of using all channels at once to simultaneously detect points over a 2.51° angle. The analyzer crystal of the triple-axis detector reduces the Full-Width at Half-Maximum (FWHM) of measured XRD peaks, thereby allowing for a better horizontal peak resolution (64). The triple axis detector has a minimum resolution of 12 arcsec, and PIXcel3D detector 6 arcsec.

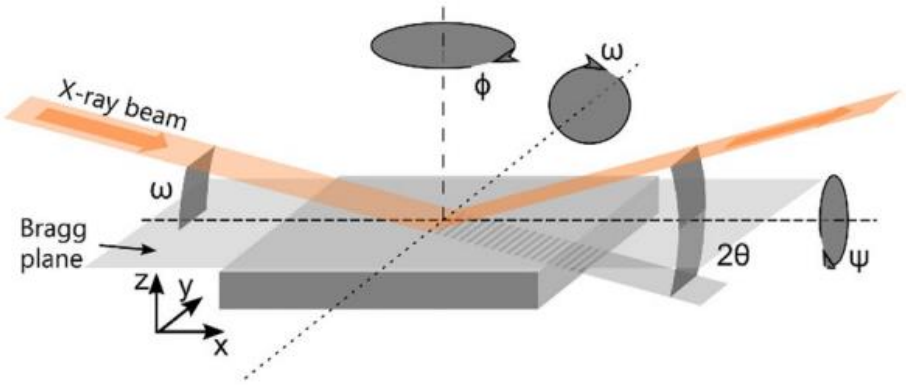

Figure 2.9: General X-ray diffraction setup with defined incident/diffracted beam angles and sample stage rotations (65).

The primary peaks of interest for these MBE-grown III-V crystals belong to the (004) and $(\bar{2}\bar{2}4)$ planes. Note that the overbar terminology corresponds to negative vector components, while underbars distinguish vector components with more than one digit. Because the experimental GaAs (001) substrates are oriented along a $\langle 100 \rangle$-type direction, the (004) peak is symmetric around the sample normal and does not require φ optimization to be detected. In contrast, the $(\bar{2}\bar{2}4)$ plane is asymmetric with respect to the sample normal and so requires φ optimization over a minimum 90° range in accordance with the fourfold crystal symmetry around (001). To generalize these definitions further, symmetric peaks are those where the plane normal is parallel to the scattering vector while asymmetric peaks are all others. The ω-2θ scans conducted here generally target symmetric (004) peaks for detection of III-V crystals. Cd_3As_2 scans follow similar reasoning, but they target the much higher order indices $\{00\underline{16}\}$ and $\{\bar{4}\bar{4}\underline{16}\}$ because of the much larger large unit cell ($a = 12.633$ Å, $c = 25.428$ Å). This corresponds to similar interplanar scattering distances in accordance with Bragg's law so that all peaks of interest may be captured over a relatively small θ range.

$$\lambda = 2d_{hkl} \sin\theta. \tag{2.5}$$

This equation relates the incident x-ray wavelength λ to the miller indices (hkl) of the interplanar distance d_{hkl} and the diffracted angle θ. The λ used for these measurements is the average of the Cu Kα doublet (Cu $K\alpha_1$ and Cu $K\alpha_2$): 1.5406 Å. The data shown here is measured in 0.05° steps over a 5-55° ω range, and in finer 0.005° steps over a 27-34° ω range which encompasses all peaks of interest.

Because Cd_3As_2 belongs to the tetragonal space group $I4_1/acd$ (#142), its XRD should theoretically produce more peaks of lesser multiplicity than in the case of a cubic system. For

example, its (400) and (040) peaks corresponding to $a/4$ = 3.158 Å should have slightly larger θ values than the (004) peak corresponding to $c/8$ = 3.179 Å. In the case of an undesired polycrystalline sample, this could cause overlap which makes peak analysis difficult from a FWHM determination standpoint. In any case, it is important to ensure that the plane reflections selected for XRD are of high enough relative intensity that they may be consistently identified beyond the noise floor of the measurement. The fundamental equation for the structure factor of a unit cell,

$$F_{hkl}(\theta) = \sum_i f_i(\theta) \exp[2\pi i(hx_i + ky_i + lz_i)], \tag{2.6}$$

and Euler's identity,

$$e^{ix} = \cos x + i \sin x, \tag{2.7}$$

are therefore applied to determine if the following plane reflections should be forbidden for the TS Cd_3As_2 crystal (that is, the diffracted beam destructively interferes to become zero intensity), as well as the relative intensities of nonzero reflections. Here, x_i, y_i, z_i are the fractional coordinates of the atom i in terms of its unit cell position. The atomic scattering factors f_i are element-specific, e.g. f_{Cd} and f_{As}, and are used for relative intensity comparisons since their values require more complicated electron density computation for quantification. Atoms belonging to the same Wyckoff position will have the same contribution to $F_{hkl}(\theta)$ as a result of crystalline symmetry. Therefore, it is only required that f_i for every Wyckoff position be calculated and then scaled by their multiplicity within the unit cell for the total contribution to $F_{hkl}(\theta)$.

Using the symmetry associated with the Wyckoff positions of the atoms in the Cd_3As_2 unit cell (As: 32g, 16d ,16e; Cd: 32g, 32g, 32g), the solutions for the (400), (040), (004), (008), and

$(00\underline{16})$ planes have been calculated as shown in Table 2.1 (15). These solutions show that the (004) plane reflection is virtually nonexistent in comparison to those of the (400) and (040) planes with the same lattice parameter a. This effect is further compounded by the fact that the XRD signal is proportional to the square of the structure factor. The expectation is therefore that the (008) peak, the $(00\underline{16})$ peak, and the combined $(400)/(040)$ peak (according to the equal a and b parameters) should be visible in an experimental XRD spectrum.

Table 2.1: Calculated structure factors for relevant $I4_1/acd$ Cd_3As_2 X-ray diffraction peaks in terms of the atomic scattering factors f_{Cd} and f_{As}. $F_{hkl}(\theta)^2$ compares the considered planes as the X-ray diffraction intensity is proportional to this value. The theoretical Relative Intensities (RIs) of these peaks are also reported.

Plane	$F_{hkl}(\theta)$	$F_{hkl}(\theta)^2$	RI (%)
(400)	$63.836 * f_{As}(\theta) - 91.733 * f_{Cd}(\theta)$	$4.075 \times 10^3 f_{As}(\theta)^2 - 5.856 \times 10^3 f_{As}(\theta) f_{Cd}(\theta) + 8.415 \times 10^3 f_{Cd}(\theta)^2$	21.58
(040)	$62.790 * f_{As}(\theta) - 89.205 * f_{Cd}(\theta)$	$3.943 \times 10^3 f_{As}(\theta)^2 - 5.601 \times 10^3 f_{As}(\theta) f_{Cd}(\theta) + 7.958 \times 10^3 f_{Cd}(\theta)^2$	21.58
(004)	$3.1824 \times 10^{-2} * f_{As}(\theta) - 4.192 \times 10^{-3} * f_{Cd}(\theta)$	$1.013 \times 10^{-3} f_{As}(\theta)^2 + 2.668 \times 10^{-3} f_{As}(\theta) f_{Cd}(\theta) + 1.757 \times 10^{-5} f_{Cd}(\theta)^2$	0.00
(008)	$63.851 * f_{As}(\theta) - 88.077 * f_{Cd}(\theta)$	$4.077 \times 10^3 f_{As}(\theta)^2 - 5.624 \times 10^3 f_{As}(\theta) f_{Cd}(\theta) + 7.757 \times 10^3 f_{Cd}(\theta)^2$	9.80
$(00\underline{16})$	$63.407 * f_{As}(\theta) + 66.268 * f_{Cd}(\theta)$	$4.020 \times 10^3 f_{As}(\theta)^2 + 4.202 \times 10^3 f_{As}(\theta) f_{Cd}(\theta) + 4.392 \times 10^3 f_{Cd}(\theta)^2$	5.85

To test the accuracy of these calculations, a theoretical XRD spectrum for polycrystalline Cd_3As_2 was simulated to determine the relative intensity of the considered peaks. The open access Python package XRayUtilities was used for determining these values (66).

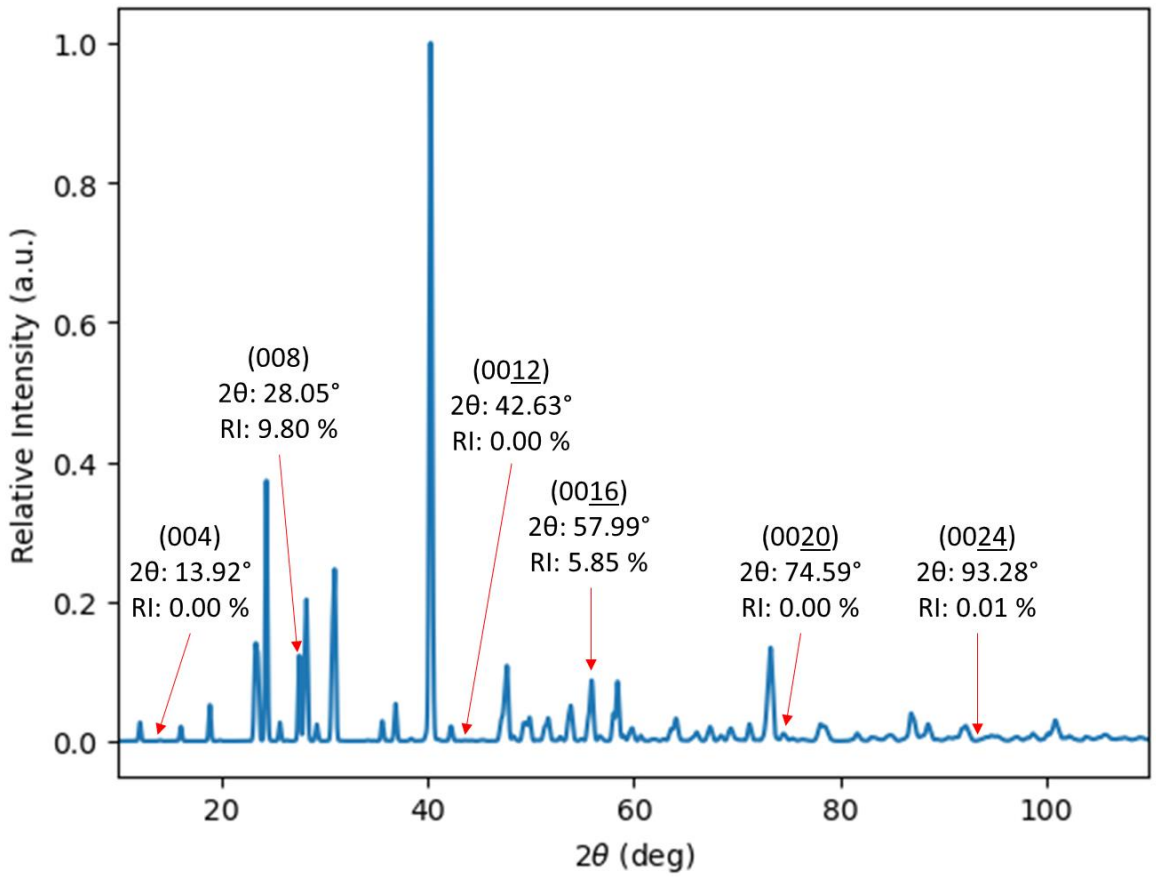

Figure 2.10: Simulation of X-ray diffraction peaks for polycrystalline $I4_1/acd$ Cd_3As_2. Peaks visible during X-ray diffraction of the (001)-oriented single crystal are specifically labeled with their simulated 2θ positions. Their Relative Intensities (RIs) are also listed.

Only the peaks visible for the (001)-oriented crystal are labeled because the others should not appear in these symmetric scans. The intensities for (400) and (040) correspond to the same, combined peak with intensity 21.58 %. The (004) peak intensity is essentially zero according to the simulation, agreeing with the structure factor calculations. In addition, its multiples $(00\underline{12})$, $(00\underline{20})$, and $(00\underline{24})$ have negligible intensities. The substantially smaller intensity of the (004) peak therefore reasonably allows the a-lattice parameter reflections (400) and (040) to be

analyzed for polycrystalline films without concern for the close peak grouping issue proposed before. The other major conclusion from these calculations is that the $(00\underline{16})$ peak should have a similar relative intensity compared to the alternative for basal-plane single crystal identification (008). It is therefore used for identification purposes in the analysis of XRD characterization since it is closest to the III-V (004) peaks identified from the buffer and substrate layers of the experimental heterostructure.

In addition to fundamental crystal phase identification, these measured ternary III-V alloy (004) peak positions provide data for the approximation of alloy composition which has been of great use in targeting lattice-matched buffers for Cd_3As_2 overlayer deposition. This involves the linear interpolation of binary constituent peak positions to determine the alloy composition x which is a function of the cubic binary constituent lattice parameters and their alloy fractions x and $(1-x)$, according to the use of Vegard's law (57). This alloy fraction is taken as the ternary alloy composition in MBE recipe modification for specific alloy targeting. The use of a bowing parameter and its related quadratic term is available for more accurate approximation of other alloy parameters, such as band gap E, where these alloy systems deviate significantly from Vegard's law in practice. The full interpolation relation for a general composition-dependent alloy parameter $P(x)$ with addition of a system-specific bowing parameter b_i is:

$$P(x) = xP_{constituent\,1} + (1-x)P_{constituent\,2} + b_{ternary}x(1-x) \qquad (2.8)$$

Extensive work on the deviation of ternary Group III-V systems from Vegard's law is detailed elsewhere, especially for the arsenides (67). Individual ternary III-V system parameters are well documented in the literature (47).

2.2.2 Reciprocal space mapping

Reciprocal Space Mapping (RSM) is essentially a series of adjacent ω-2θ XRD scans swept over a line to produce a 2D image colored/contoured in accordance with individual pixel intensity. These absolute RSM scans cover an area defined by specific central ω and 2θ coordinates and fully swept $\omega/2\theta$ ranges. The RSM setup uses the same equipment as the ω-2θ scans. RSM was only conducted using the PIXcel3D detector with all channels active due to the greatly increased time requirements for these increased-dimensionality maps. In the case of the widely spaced peaks shown in later chapters, the PIXcel3D resolution is sufficient to accurately detect and resolve individual peaks which are closely-positioned, such as GaAs (004) and AlAs (004). RSM data is also automatically converted by the PANalytical software into reciprocal space coordinates where R is the radius of the Ewald sphere, which is set to $1/2$ in the analysis software produced by PANalytical. This produces the vectors:

$$\vec{Q}_x = R[\cos\omega - \cos(2\theta - \omega)]\hat{x}, \tag{2.9}$$

and:

$$\vec{Q}_y = \mathrm{R}[\sin\omega + \sin(2\theta - \omega)]\hat{y}. \tag{2.10}$$

Raw RSM data is taken using Cartesian coordinates defined by unit vectors in ω-2θ space. As a consequence, the $\vec{Q}_x$ and $\vec{Q}_y$ vectors derived from ω and 2θ do not lie in Cartesian space, but rather according to a curved grid. The effect is shown below in Figure 2.11. Because of this data contortion, plotting real data with respect to a line drawn along the major and minor ellipsoidal axes is also convoluted. Rather than plotting a curve using interpolated values from the curved

grid, real data points of closest fit to the ellipse lines are selected and fit with a Gaussian function to determine FWHM. This eliminates the error of interpolation (which should not be linear in this case anyways), while also applying a fitting curve which adheres to the RSM spot theory of a Gaussian intensity distribution.

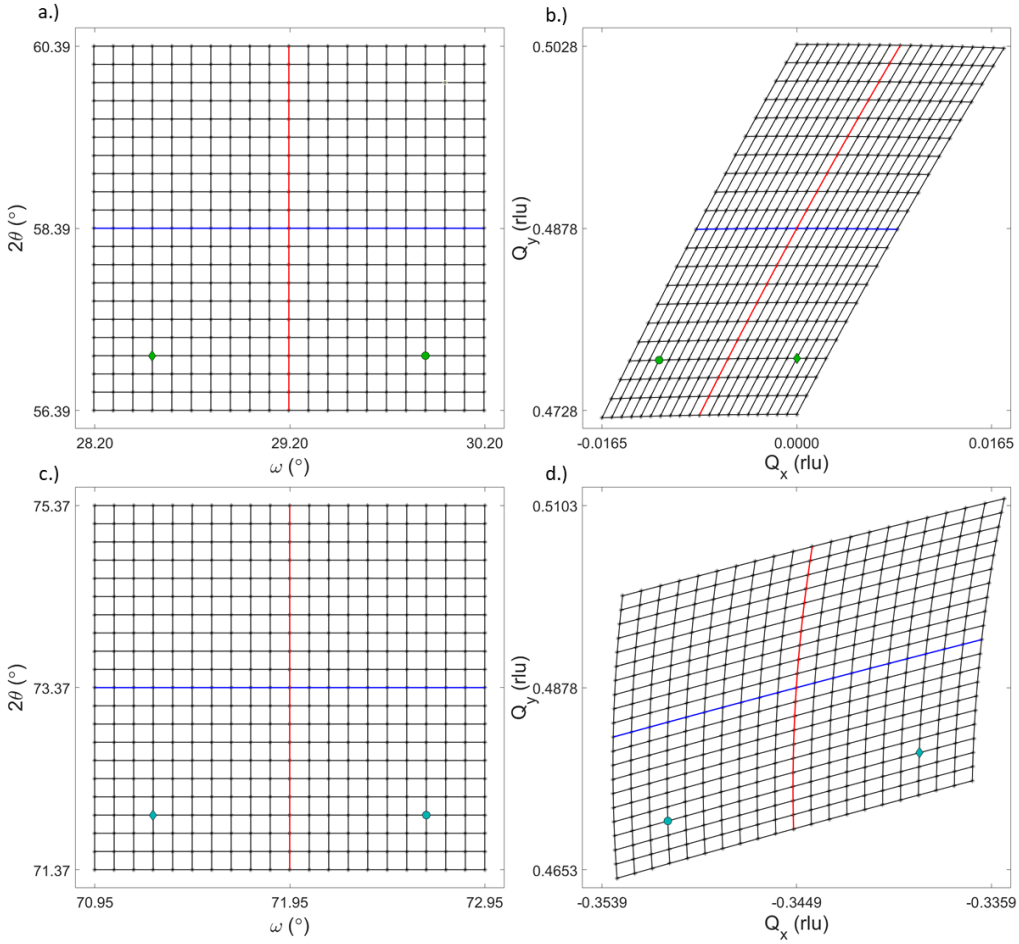

Figure 2.11: Illustration of conversion from ω,2θ to Q_x,Q_y coordinates for both the symmetric (004) and asymmetric $(\bar{2}\bar{2}4)$ reciprocal space scan areas. These grids are centered according to reflections for a cubic unit cell where a = 6.317 Å. The square grid from a.) a symmetric (004) ω-2θ scan with uniform measurement points becomes b.) the curved grid for the same (004) reflection in Q_x-Q_y space. Likewise, the square grid from c.) an asymmetric $(\bar{2}\bar{2}4)$ ω-2θ scan with uniform measurement points becomes d.) the curved grid for the same $(\bar{2}\bar{2}4)$ reflection.

An important function of RSM is the ability to determine the in-plane lattice parameter of a heterostructure layer. This requires the measurement of an asymmetric scan where the reciprocal space vector magnitude Q_x is not zero (or not centered close to zero due to error in real measurements). The asymmetric III-V $(\bar{2}\bar{2}4)$ and Cd_3As_2 $\left(\bar{4}\bar{4}\underline{16}\right)$ peaks are therefore used in the case of these measurements. These peaks were chosen due do their easy identifiability, close proximity in reciprocal space, and practical acquisition according to tool limits. Indices such as $(\bar{2}\bar{2}4)$ containing negative vector components were chosen because the goniometer geometry for diffraction is at a lower ω,2θ for the (001) sample orientation than for all-positive index cases like (224). A more glancing diffraction angle aligns the X-ray interaction volume to diffract in the shallower heterostructure layers. The thin film crystals generally require greater counting times due to their nanoscale thicknesses, as opposed to the bulk substrate. The use of shallower geometry peaks therefore has the benefit of reducing the scan time necessary to identify the ternary and Cd_3As_2 crystal peaks.

For a particular diffraction peak, the in-plane lattice parameter is derived using the fundamental equations relating d-spacing (d_{hkl}) to the plane's Miller indices (hkl) and the unit cell parameters (lattice spacings and cell angles). It is the horizontal vector component which is parallel to the Q_x axis. Fortunately, the use of cubic III-V ternaries and a tetragonal functional layer excludes the need for complex consideration of unit cell angles as they are all 90°. The d-spacing for cubic materials is:

$$\frac{1}{{d_{hkl}}^2} = \frac{h^2 + k^2 + l^2}{a^2}. \tag{2.11}$$

The d-spacing for tetragonal materials is:

$$\frac{1}{{d_{hkl}}^2} = \frac{h^2 + k^2}{a^2} + \frac{l^2}{c^2}. \tag{2.12}$$

For a tetragonal unit cell as well as nominally cubic structures which experience a biaxial in-plane strain (making them effectively tetragonal), the in-plane and out-of-plane lattice parameters are a and c. Symmetric scans readily measure the out-of-plane d-spacing, but the in-plane d-spacings can only be determined from the $\vec{Q}_x$ component of an asymmetric RSM. For the asymmetric peak $(\bar{2}\bar{2}4)$ measured in these experiments, both the in-plane and the out-of-plane lattice parameters may be computed from the horizontal component where:

$$\vec{Q} = \vec{Q}_x + \vec{Q}_y \text{ and } \vec{Q}_x = {d_x}^{-1}, \vec{Q}_y = {d_y}^{-1}, \tag{2.13}$$

and for and the asymmetric $(\bar{2}\bar{2}4)$ peak:

$$\left|\vec{Q}_x\right| = \left|\hat{Q}_{220}\right| = {d_{220}}^{-1}, \ \left|\vec{Q}_y\right| = \left|\hat{Q}_{004}\right| = {d_{004}}^{-1}. \tag{2.14}$$

The elastic tensor C_{ijkl} is a fourth-order tensor relating the second-order tensors of stress σ_{ij} and strain ε_{kl}:

$$\sigma_{ij} = C_{ijkl}\varepsilon_{kl}. \tag{2.15}$$

It is also known as the stiffness tensor, and its inverse is the compliance tensor S_{klij}:

$$\varepsilon_{kl} = S_{klij}\sigma_{ij} \tag{2.16}$$

The application of these equations requires a linearly elastic response from the considered crystal, and so does not hold for films which have a significant level of relaxation. The degree of lattice matching may be calculated by comparing the in-plane lattice parameters of Cd_3As_2 and its ternary buffers according to the biaxial, internal strain felt due to lattice mismatching. Using the conventional Voigt notation, the symmetry for orthorhombic systems enables the matrix representation:

$$\begin{bmatrix}\sigma_1\\ \sigma_2\\ \sigma_3\\ \sigma_4\\ \sigma_5\\ \sigma_6\end{bmatrix} = \begin{bmatrix}C_{11} & C_{12} & C_{13} & 0 & 0 & 0\\ C_{21} & C_{22} & C_{23} & 0 & 0 & 0\\ C_{23} & C_{32} & C_{33} & 0 & 0 & 0\\ 0 & 0 & 0 & C_{44} & 0 & 0\\ 0 & 0 & 0 & 0 & C_{55} & 0\\ 0 & 0 & 0 & 0 & 0 & C_{66}\end{bmatrix}\begin{bmatrix}\varepsilon_1\\ \varepsilon_2\\ \varepsilon_3\\ \varepsilon_4\\ \varepsilon_5\\ \varepsilon_6\end{bmatrix}. \tag{2.17}$$

The elastic tensor may be further reduced using the symmetry for tetragonal systems:

$$\begin{bmatrix}\sigma_1\\ \sigma_2\\ \sigma_3\\ \sigma_4\\ \sigma_5\\ \sigma_6\end{bmatrix} = \begin{bmatrix}C_{11} & C_{12} & C_{13} & 0 & 0 & 0\\ C_{12} & C_{11} & C_{13} & 0 & 0 & 0\\ C_{13} & C_{13} & C_{33} & 0 & 0 & 0\\ 0 & 0 & 0 & C_{44} & 0 & 0\\ 0 & 0 & 0 & 0 & C_{44} & 0\\ 0 & 0 & 0 & 0 & 0 & \frac{C_{11}-C_{12}}{2}\end{bmatrix}\begin{bmatrix}\varepsilon_1\\ \varepsilon_2\\ \varepsilon_3\\ \varepsilon_4\\ \varepsilon_5\\ \varepsilon_6\end{bmatrix}. \tag{2.18}$$

For systems with cubic symmetry such as the zinc blende III-Vs, symmetry produces the stiffness matrix:

$$\begin{bmatrix}\sigma_1\\ \sigma_2\\ \sigma_3\\ \sigma_4\\ \sigma_5\\ \sigma_6\end{bmatrix} = \begin{bmatrix}C_{11} & C_{12} & C_{12} & 0 & 0 & 0\\ C_{12} & C_{11} & C_{12} & 0 & 0 & 0\\ C_{12} & C_{12} & C_{11} & 0 & 0 & 0\\ 0 & 0 & 0 & C_{44} & 0 & 0\\ 0 & 0 & 0 & 0 & C_{44} & 0\\ 0 & 0 & 0 & 0 & 0 & C_{44}\end{bmatrix}\begin{bmatrix}\varepsilon_1\\ \varepsilon_2\\ \varepsilon_3\\ \varepsilon_4\\ \varepsilon_5\\ \varepsilon_6\end{bmatrix}. \tag{2.19}$$

Considering that biaxial stress between Cd_3As_2 and its ternary buffers is exclusively in-plane, the geometry dictates that $\sigma_1 = \sigma_2$ and that all other stresses are zero. In addition, $\varepsilon_1 = \varepsilon_2 \neq \varepsilon_3$ and all shear strains are zero. Matrix multiplication yields a series of equations for the vector components of stress, For Cd_3As_2 they are:

$$\sigma_1 = C_{11}\varepsilon_1 + C_{12}\varepsilon_2 + C_{13}\varepsilon_3 = \sigma, \tag{2.20}$$

$$\sigma_2 = C_{12}\varepsilon_1 + C_{11}\varepsilon_2 + C_{13}\varepsilon_3 = \sigma, \tag{2.21}$$

$$\sigma_3 = C_{13}\varepsilon_1 + C_{13}\varepsilon_2 + C_{33}\varepsilon_3 = \sigma. \tag{2.22}$$

Solving these equations for out-of-plane stress yields:

$$\varepsilon_3 = \frac{-2C_{13}\varepsilon_1}{C_{33}} \tag{2.23}$$

Similarly for the cubic zinc blende materials:

$$\varepsilon_3 = \frac{-2C_{12}\varepsilon_1}{C_{11}} \tag{2.24}$$

The in-plane biaxial strain in the nominally-cubic zinc blende ternary III-V alloys are of particular interest because these buffers should have approximately zero in-plane stress if they are truly metamorphically-grown. For materials with known bulk lattice constants such as binary III-V compounds and Cd_3As_2, the out-of-plane lattice constant is directly measured by symmetric XRD scans. Three lattice parameters are therefore considered: the relaxed cubic crystal lattice parameter a_0, the strained in-plane lattice parameter $a = b$, and the strained out-of-plane lattice parameter c. They are related to the in-plane (ε_1) and out-of-plane (ε_3) strains. The literature values

for the material-specific stiffness tensor components are utilized to solve for ε_1 knowing the literature value of a_0 and the experimental value of d_{hkl} (47). For cubic materials:

$$d_{hkl} = \frac{a_0}{\sqrt{h^2 + k^2 + l^2}}\left(1 - \frac{2C_{12}\varepsilon_1}{C_{11}}\right), \tag{2.25}$$

and for Cd_3As_2:

$$d_{hkl} = \frac{a_0}{\sqrt{h^2 + k^2 + l^2}}\left(1 - \frac{2C_{13}\varepsilon_1}{C_{33}}\right). \tag{2.26}$$

2.2.3 X-ray reflectivity

X-Ray Reflectivity (XRR) is a glancing angle measurement using the same geometry as XRD, where extremely small $\omega/2\theta$ ranges are scanned to produce an interference pattern. In contrast to XRD, XRR measurements measure the signal of a reflected beam and not a diffracted beam. The periodicity of oscillations in the interference pattern scales inversely with film thickness, as illustrated by three XRayUtilities simulations of Cd_3As_2 on 2 µm AlInSb/GaAs (001).

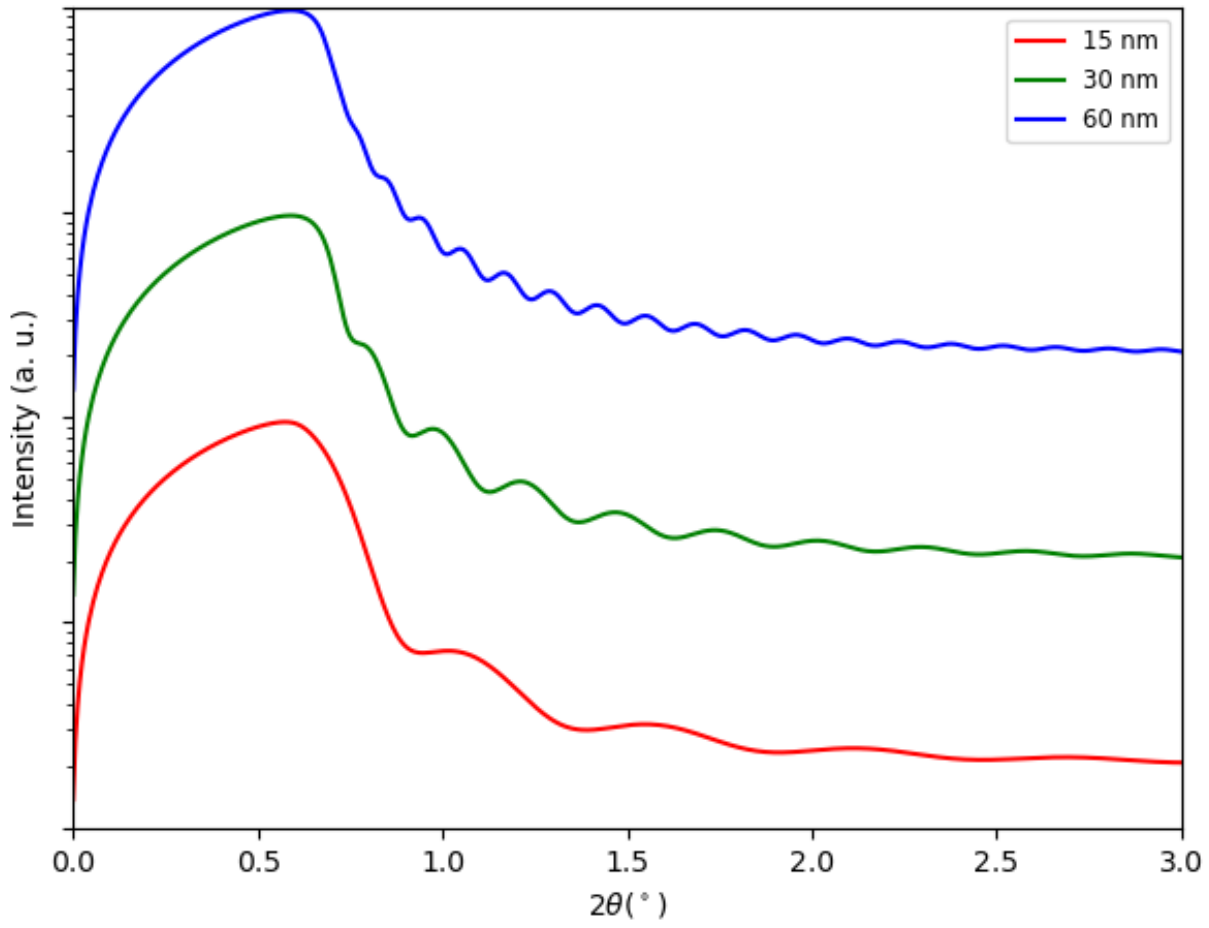

Figure 2.12: X-ray reflectivity simulations for Cd_3As_2 films of varying thicknesses on 2 µm AlInSb/GaAs (001).

Here the simulated XRR curves are shown for Cd_3As_2 thicknesses of 15 nm, 30 nm, and 60 nm. Note that the spectra are staggered into a waterfall plot to compare the oscillation periodicity between them, so inter-plot intensities cannot be compared. As the Cd_3As_2 thickness increases, the spacing becomes fine enough to make peak identification difficult. In addition, the oscillation amplitude with respect to the XRR background decreases with increasing film thickness. Fortunately, the ~30 nm Cd_3As_2 films measured in these experiments have wide enough oscillations of sufficient amplitude for easy peak identification and thickness determination.

2.3 Atomic force microscopy

Atomic Force Microscopy (AFM) is an excellent post-process technique for characterizing the surface character of these MBE-grown layers. It is conducted here using a Bruker ICON AFM system placed within an isolation hood to reduce noise. All shown measurements are conducted using a standard Si AFM tip in tapping mode with its drive frequency automatically tuned through the instrument software. AFM is useful in determining the extent of surface roughening during each heterostructure growth step, and its characterization of the ternary III-V systems is necessary for the objective of lattice-matching these buffers with a Cd_3As_2 overlayer.

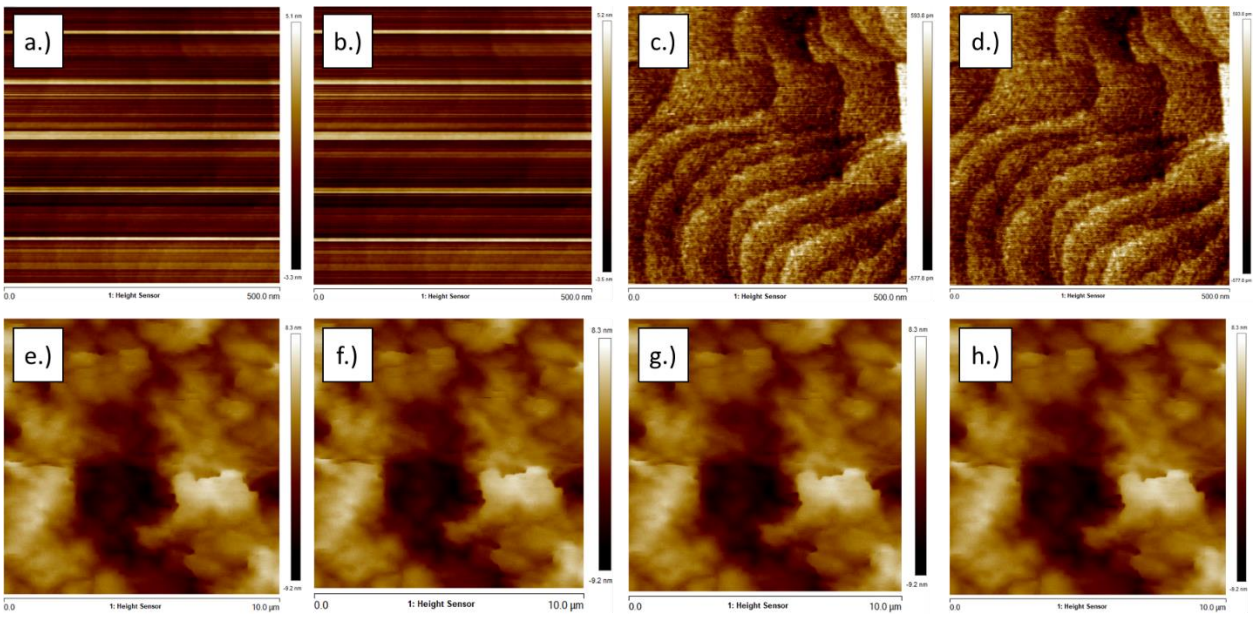

Figure 2.13: Examples of a.) raw (no change), b.) plane-fitting, c.) flattening, and d.) combined plane-fitting/flattening operations applied to a 500 nm × 500 nm atomic force microscopy image of $Al_{49.8}In_{50.2}Sb$/ AlAs/GaAs (001). All operations are first-order. The same order of operations is applied to a 10 µm × 10 µm image of the same sample over e.) through h.).

AFM done here shows that the variance in ternary layer surface roughness is highly dependent on growth temperature, with more variance existing within the same III-V systems than between them. In general, for all three experimental systems the surface of the epitaxially grown Cd_3As_2 has followed the same topography of its ternary buffer. Image analysis is supplemented by 1st-order plane-fitting and flattening operations, both of which are commonly used in the literature. Bruker's Nanoscope Analysis software is used for these image changes. The first-order plane-fitting applies a polynomial adjustment to the data set to account for long-range changes in topography not based on local surface conditions, such as substrate curvature. The 1st-order flattening operation accounts for sample tilt owing to the nonzero angle between the probed surface normal and the AFM tip z-axis.

2.4 Scanning electron microscopy

Cross-Sectional Scanning Electron Microscopy (XS-SEM) is employed to measure the approximate layer thicknesses of ternary buffers in the cross sections of key samples.

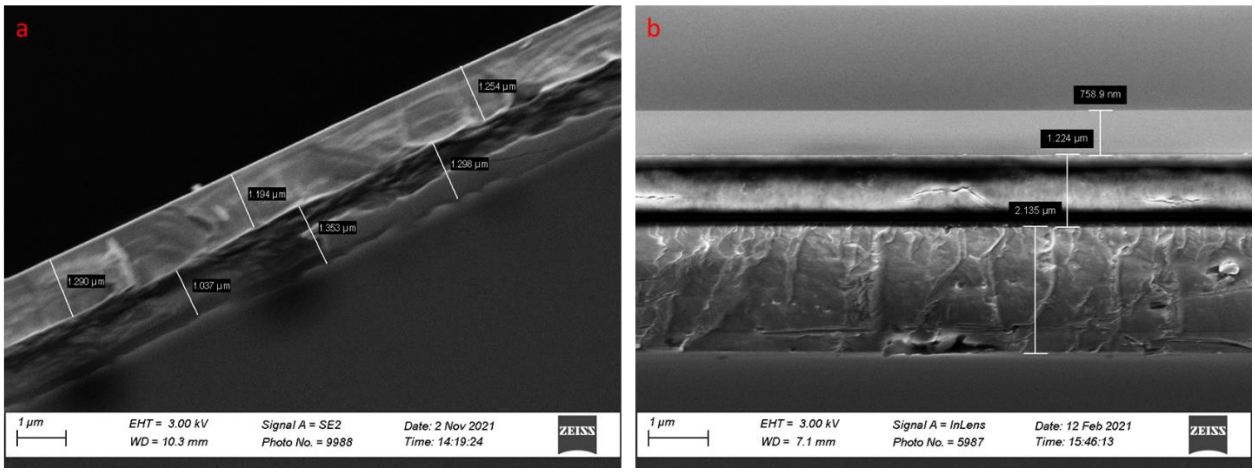

Figure 2.14: Cross-sectional scanning electron microcopy of a) $Al_{49.8}In_{50.2}Sb$/AlAs/GaAs (001) and b) Cd_3As_2/ $Al_{39.0}In_{61.0}Sb$/AlAs/GaAs (001). These images were taken using an in-lens detector at a relatively low accelerating voltage (3.00 kV).

The imaging system is a Zeiss GeminiSEM 300 high-resolution field-emission SEM. XS-SEM conducted here utilizes cleaved wafer sections without the need for any additional sample preparation. This is because the semimetallic and semiconducting natures of the layer materials provide sufficient conduction to prevent charging from the electron beam. The high magnification and good elemental contrast allow for thickness measurements that have an accuracy approaching tens of nanometers. These measurements have consistently been used for initial growth rate calculations.

2.5 Transmission electron microscopy

Transmission Electron Microscopy (TEM) was conducted on representative ternary III-V samples by collaborators Edwin Supple and Dr. Brian Gorman at the Colorado School of Mines. The transmission of electrons through very thin foil (lamella) made from those samples allows for crystalline defects such as dislocations to be identified through contrast caused by beam scattering. The primary objective in conducting these measurements is to estimate Threading Dislocation Density (TDD), which is generally a measure of crystalline quality as it pertains to electronic properties. Naturally, lower TDDs are associated with higher electron mobilities. Despite some deviation in lamella thickness, heterostructures covering all experimental III-V ternaries and their buffer material variations produced consistent, reasonable results for their TDDs. These results are analyzed for their correlation with the processing parameters of their respective samples.

The methodology for determining TDD follows the counting of threading dislocations in a given lamella's cross-section. Knowing the width of the considered section, the depth of the film is calculated geometrically from the known layer thickness and sample tilt with respect to the incident electron beam. The TDD is the threading dislocation count divided by the product of the considered section width and the calculated layer depth.

2.6 Van der Pauw measurements

The electronic properties of Cd_3As_2 films were measured via Van der Pauw measurements according to the geometry in Figure 2.15. This measurement applies a current along a longitudinal axis x and an external magnetic field $\overrightarrow{B_Z}$ so that a mutually orthogonal, transverse Hall voltage is generated along the y axis (68).

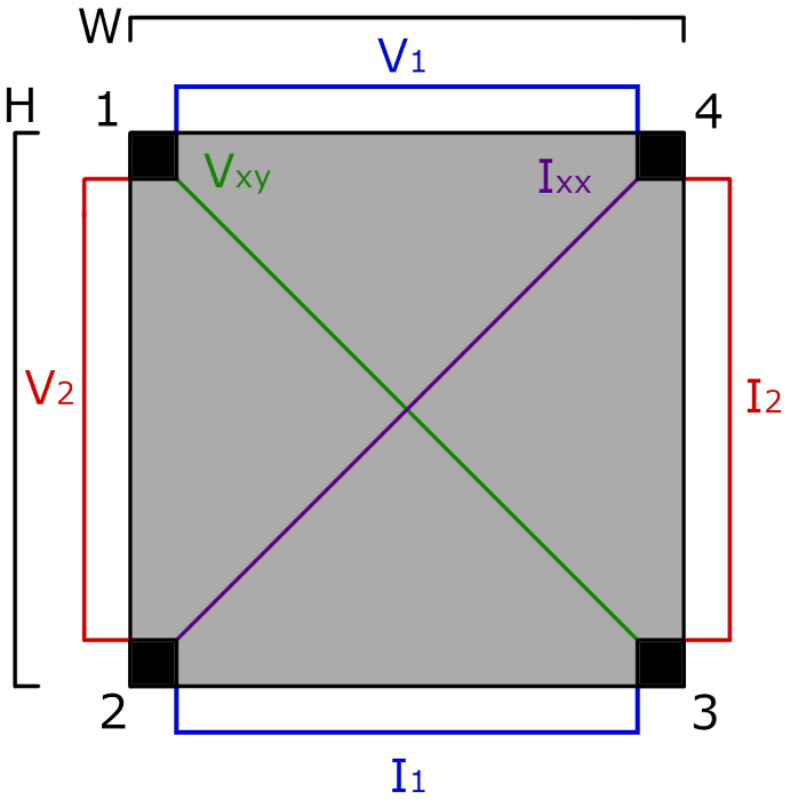

Figure 2.15: Van der Pauw Hall measurement geometry with relevant parameters.

Here, four contacts are attached in a square geometry and a current is run along orthogonal directions (I_1 and I_2) to determine the voltage drops V_1 and V_2, and subsequently through Ohm's law $R_i = V_i / I_i$. The contact pairs used for the two directional non-Hall measurements are

(1,2)/(3,4) and (1,4)/(2,3). R_2 is taken as the larger value so that $R_2 > R_1$. These values are used to solve the Van der Pauw equation for the ideal sheet resistance R_S in units of Ω/square:

$$\exp\frac{-\pi R_1}{R_S} + \exp\frac{-\pi R_2}{R_S} = 1. \tag{2.27}$$

The contacts should be on the sample corners and the contact area should be less than 10% of the sample area for these measurements to be valid. While the longitudinal resistances should be the same for a perfect sample, in reality they vary due to non-square contact and sample geometries (69). So long as $1 \leq R_2/R_1 \leq 10{,}000$, a geometric factor f may be solved to account for this effect:

$$\frac{R_2 - R_1}{R_2 + R_1}\frac{\ln 2}{f} = \cosh^{-1}\left[0.5 * exp\left(\frac{\ln 2}{f}\right)\right]. \tag{2.28}$$

The product fR_S is a more accurate estimation of the sheet resistance and is used for further calculations. The bulk resistivity $\rho = fR_S * t$ where t is the conductive film thickness, which should be less than 1 mm for ρ to be accurate. The Hall measurement is conducted by applying a longitudinal current I_{xx} between either contact pair 1,3 or 2,4. When a current is applied across contacts 1,3 a Hall voltage is measured across contacts 2,4, and vice-versa. A reverse current measurement is also conducted and the four voltage drops are averaged as the final Hall voltage V_{xy}. This eliminates error due to asymmetry in the sample and contact geometries. A Hall voltage is measured for every change in $\overrightarrow{B_Z}$ as it moves to its setpoints in linear increments. The Hall resistance R_{xy} is the Hall voltage V_{xy} divided by the applied longitudinal current I_{xx}. A representative Van der Pauw measurement is shown in Figure 2.16. Shubnikov-de Haas oscillations in the longitudinal bulk resistivity correspond with transitions in between the Landau levels. Plateaus in R_{xy} correspond to specific Landau filling factors υ.

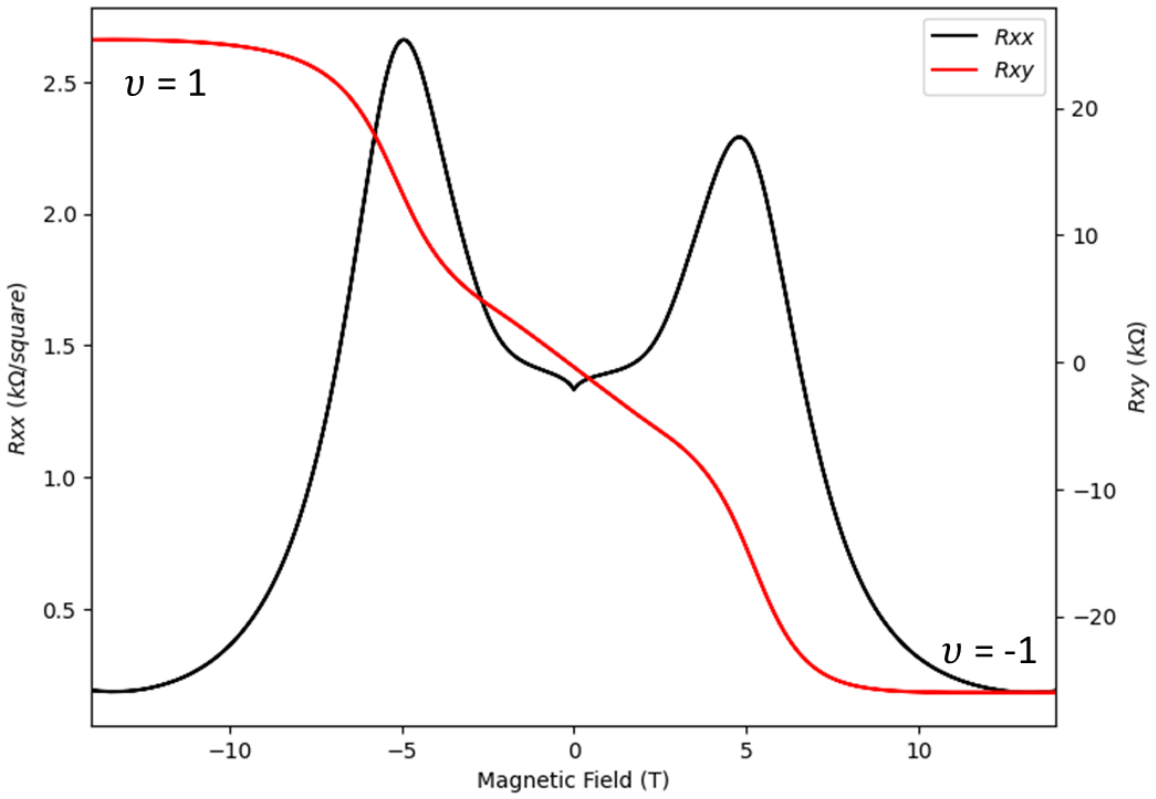

Figure 2.16: Van der Pauw Hall data for a nearly-lattice matched Cd_3As_2/AlInSb heterostructure.

Real measurement curves are asymmetric due to the mixing of the longitudinal R_{xx} signal with the transverse R_{xy} data. This can be caused by inhomogeneity in the applied B-field. Other external B-fields may also contribute to the Hall effect. Asymmetrization and symmetrization of the $R_{xy}(B)$ data are used to isolate the transverse signal $R_{xy,iso}$ and the longitudinal signal $R_{xx,iso}$:

$$R_{xy,iso} = \frac{R_{xy}(B) - R_{xy}(-B)}{2}, \tag{2.29}$$

and:

$$R_{xx,iso} = \frac{R_{xy}(B) + R_{xy}(-B)}{2}. \tag{2.30}$$

All zero-field bulk resistivity measurements are averaged for a mean bulk resistivity value ρ_{xx}. The Hall coefficient R_H is the slope of a linear fit of the linear region of $R_{xy,iso}$ vs. $\overrightarrow{B_Z}$, generally within the bounds of $\overrightarrow{B_Z} = \pm 2$ T:

$$R_H = \left.\frac{\delta R_{xy}}{\delta\left|\overrightarrow{B_Z}\right|}\right|_{\left|\overrightarrow{BZ}\right| \cong 0}. \tag{2.31}$$

The utilized R_H is the mean average of the positive sweep slope (0 to +14 T, -14 T to 0) and the negative sweep slope (-14 T to +14 T). This value, along with the charge of an electron e, is used to calculate the sheet carrier density n_{sheet}:

$$n_{\mathrm{sheet}} = \frac{1}{R_H e}, \tag{2.32}$$

the bulk carrier density n_{bulk}:

$$n_{bulk} = \frac{1}{R_H e t}, \tag{2.33}$$

and the carrier mobility μ:

$$\mu = \frac{1}{\rho_{xx} n_{bulk} e t} = \frac{R_H}{\rho_{xx}}. \tag{2.34}$$

Chapter 3: Ternary III-V Alloys for Virtual Substrate Engineering

3.1 Selection of III-V alloy systems

3.1.1 Considerations for lattice-matched cadmium arsenide

A virtual substrate is a thin film buffer layer or heterostructure of such films designed to achieve or improve a certain quality of a functional overlayer. The development of these virtual substrates allows for material growth that would otherwise be economically prohibitive or even impossible due to the inaccessibility of an equivalent substrate wafer with thickness on the order of hundreds of microns. For example, reverse linearly graded SiGe buffers on easily accessible Si (001) wafers act as virtual substrates for high-quality $Si_{0.2}Ge_{0.8}$ growth with low TDDs on the order of 4×10^{6} cm^{-2} (70). There are many more examples of these compositionally graded buffers in the literature: linear and non-linear alike. They may be step graded or continuously graded based on the necessity of reducing the TDD and/or other considerations. The potential for a virtual substrate here, however, is in its use for lattice-matching with a Cd_3As_2 overlayer to preserve the surface electronic band structure so that its TS properties are maintained. The electronic properties of the buffer layer are not critically linked to overlayer growth outside of the requirement that it not be conducting (for device incorporation). The use of a graded buffer is forgone with a compositionally constant buffer being used instead.

The epitaxial processes considered here are divided into the categories of homomorphic, pseudomorphic, and metamorphic growth paradigms (71). Homomorphic growth is defined as the

growth of a thin film with the same crystal as its substrate. This type of growth is essentially the extension of the substrate material, e.g. GaAs homomorphically grown on GaAs. Because the grown crystal matches the substrate there is no in-plane biaxial strain due to interfacial mismatch. The initial homomorphic growth of a 300 nm GaAs buffer acts to reduce the roughness of the substrate surface and to bury surface contaminants (72). The other two modes involve the growth of a different crystal than the substrate and are distinguished by the nature of the interface between the two phases, especially the similarities regarding in-plane lattice geometries. Pseudomorphic growth occurs when the lattice mismatch is small enough that that the thin film may be elastically strained to match the in-plane lattice parameter(s) of the substrate at the interface. In cases where the interfacial lattice mismatch is great enough, an ordered array of edge dislocations spontaneously forms during film nucleation (73,74). This metamorphic interface is created in lieu of extreme biaxial strain, and so the subsequent metamorphic film is ideally totally relaxed.

The metamorphic growth of ternary III-V alloys, like that shown in this dissertation, may still facilitate the high-quality epitaxial growth one might expect from the use of a graded or stepped buffer while also providing excellent and relatively facile compositional tunability for acquiring a lattice-matched Cd_3As_2 overlayer.

3.1.2 Use of metamorphic buffers for virtual substrates

Neither homomorphic nor pseudomorphic buffers are suitable here as no III-V binary substrates, including GaAs (001), possess lattice parameters which are closely lattice matched with Cd_3As_2 (15,47). More specifically, the FCC sublattice of the As positions within the Cd_3As_2 unit cell has an a lattice parameter of 6.317 Å which is dissimilar from that of any zinc blende binary III-V compound. The ternary III-V systems GaInSb, AlInSb, and InAsSb are chosen for metamorphic growth on GaAs (001) substrates because they can be lattice matched to the As sublattice interatomic distance demarcated in Figure 3.1. InPSb can also be lattice-matched with Cd_3As_2, but a P source is not available in this experimental setup so InPSb was not explored.

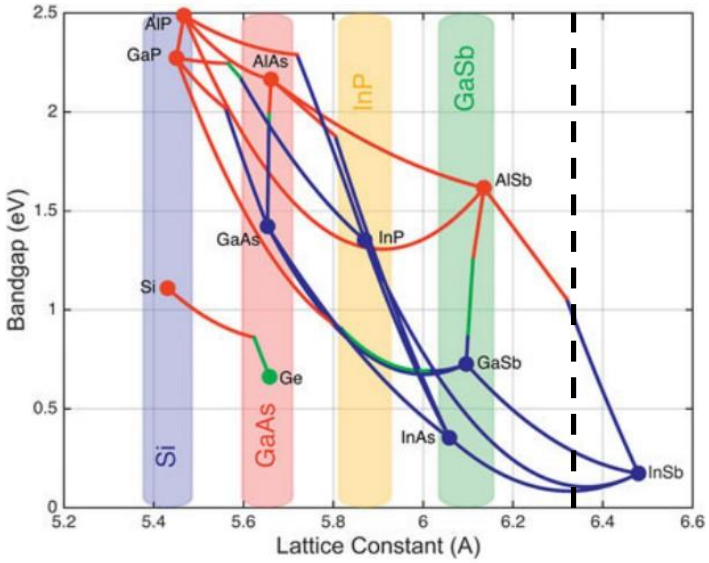

Figure 3.1: Direct (blue), sixfold symmetric indirect (red), and eightfold symmetric indirect (green) band gaps of III-V compounds and their alloys. Si, Ge and their alloys are also included for reference. A black dashed line is added to the original figure to indicate the interatomic distance of the Cd_3As_2 As face-centered cubic sublattice. It can be seen that the four ternary III-V alloy systems GaInSb, AlInSb, InAsSb, and InPSb may all be lattice matched to this value (71).

There is a critical thickness h_c where the Gibbs free energy of misfit dislocation formation becomes equal to the elastic strain energy of a growing lattice-mismatched thin film:

$$h_c \cong \left(\frac{1-\nu}{1+\nu}\right)\left(\frac{1}{16\pi\sqrt{2}}\right)\left[\frac{b^2}{a}\right]\left[\left(\frac{1}{f^2}\right)\ln\left(\frac{h_c}{b}\right)\right]. \quad (3.1)$$

It is possible that no physical solution (positive and not complex) exists for the critical thickness. In these cases, there is no overlayer thickness where pseudomorphic growth is preferred over its metamorphic counterpart. Regarding this strain energy balance only, the three experimental systems GaInSb, AlInSb, and InAsSb all possess a negative critical thickness when grown on GaAs (001) and will therefore form a metamorphic interface (73). Here b is the Burgers vector which is $\frac{1}{2}\langle 110\rangle$-type for these zinc blende systems (75,76). The Poisson ratio ν, the film lattice parameter a, and the lattice mismatch f (also called misfit) are also factors.

3.1.3 Temperature control during MBE

For the three ternary alloy systems explored here, a significant increase in pyrometer signal was observed during film nucleation at a constant substrate temperature setpoint. A cause for this discrepancy may be the change in radiative heating efficiency during ternary nucleation, as it would raise the sample temperature from the initial setpoint without any change in heater output power. Figure 3.2 reports *in situ* pyrometry which illustrates this radiative heating effect well. Here, a representative sample from each of the experimental systems shows how the recorded substrate temperature increases with respect to the initially chosen growth setpoint.

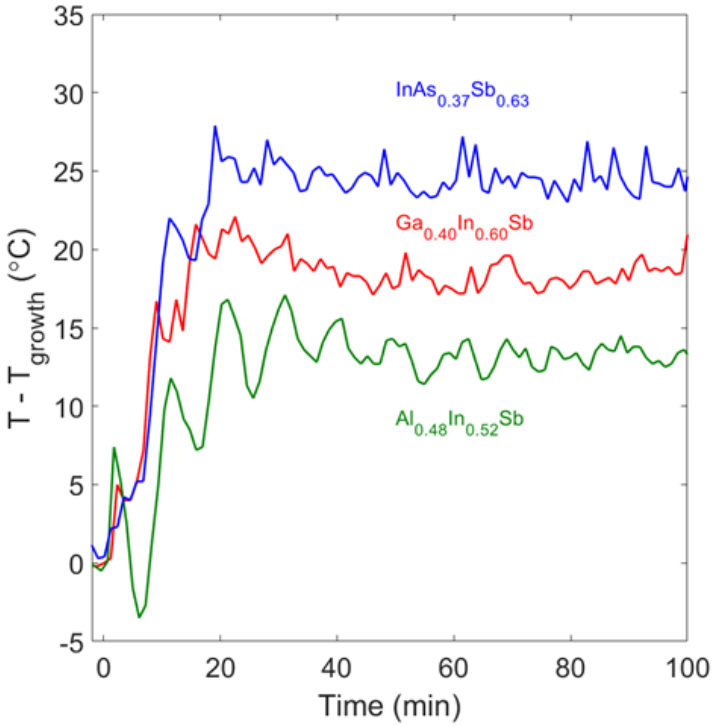

Figure 3.2: Representative *in situ* pyrometry showing the growth of AlInSb, GaInSb, and InAsSb over the first hundred minutes of molecular beam epitaxy. The y-axis is adjusted to report the jump in pyrometer signal $T-T_{growth}$.

The theoretical optical band gaps E_g of these systems are calculated using Equation 2.8, which takes the parabolic bowing parameters into account, and are listed in Table 3.1.

Table 3.1: Calculated direct optical band gaps for selected experimental samples covering all six ternary/binary heterostructure permutations.

Experimental Alloy	Theoretical Band Gap (eV)
$Ga_{43.9}In_{56.1}Sb/GaAs$	0.309
$Ga_{41.9}In_{58.1}Sb/AlAs$	0.300
$Al_{51.5}In_{48.5}Sb/GaAs$	1.145
$Al_{49.8}In_{50.2}Sb/AlAs$	1.108
$InAs_{40.7}Sb_{59.3}/GaAs$	0.102
$InAs_{39.0}Sb_{61.0}/AlAs$	0.101

These calculated E_g values are substantially different between the ternary systems, with lattice-matched composition InAsSb alloys possessing $E_g = 0.10\ eV$, GaInSb possessing $E_g = 0.30\ eV$, and AlInSb possessing $E_g = 1.07\ eV$ (47). The temperature jumps during film nucleation are inversely proportional to the direct optical band gaps of the ternary alloys. The shift in temperature is greatest when nucleating InAsSb layers, followed by GaInSb, and then AlInSb. Oscillations are clearly visible in the AlInSb curve, representing a real temperature effect which occurs as the initial layer thickness interferes constructively and deconstructively with the wavelengths absorbed by the pyrometer (77). The temperature jump during nucleation explains why InAsSb growths required lower starting temperatures between 440 °C and 460 °C to prevent phase separation caused by InSb constituent melting.

Furthermore, the theoretical spinodal decomposition range for InAsSb is the largest for all three systems as shown later in this chapter. The control software used in these experiments is capable of mediating substrate heater output with respect to pyrometer temperature. This control was applied in later samples to keep the pyrometer temperature at a set target, allowing for film nucleation and growth closer to the InSb melting point without causing thermal decomposition over longer growth periods.

3.2 Spinodal decomposition of ternary III-V alloys

These films were initially investigated for their stability during and after growth. One mode of instability is spinodal decomposition, which occurs when the Gibbs free energy $G_i(x)$ of a multi-constituent system, a function of composition x of constituent i, contains at least one set of points where $\frac{d^2G}{dx^2} = 0$. The calculation of the Gibbs free energy was completed using the Delta Lattice Parameter (DLP) model where the internal strain effects of the ternary constituent lattices are taken into account (78). This strain effect is encompassed by the variable Ω that is added to the standard Gibbs free energy equation:

$$\Delta G(x) = (1-x)[\Delta H - T\Delta S + x\Omega] + TR[x\ln x + (1-x)\ln(1-x)]. \quad (3.2)$$

Here, ΔH is the ternary's enthalpy of formation, T is the system temperature, ΔS is the change in entropy, and R is the combined gas constant. Thermodynamic data for Group III arsenides and antimonides are readily available within the literature (79,80). The arsenide enthalpy and entropy values here are static within the same phase, but the reported antimonide values are temperature-dependent in 100 °C increments within the same phase, giving their Gibbs free energy contributions greater accuracy. The Ω term is a function of the difference between constituent lattice parameters Δa and the average constituent lattice parameter $\bar{a}$:

$$\Omega = 4.375k\frac{(\Delta a^2)}{\bar{a}^{4.5}}. \quad (3.3)$$

The constant $k = 1.527\times10^7$ J/(mol•Å). The theoretical spinodal decomposition curves are calculated according to where $\frac{d^2G}{dx^2} = 0$, for all three ternary systems.

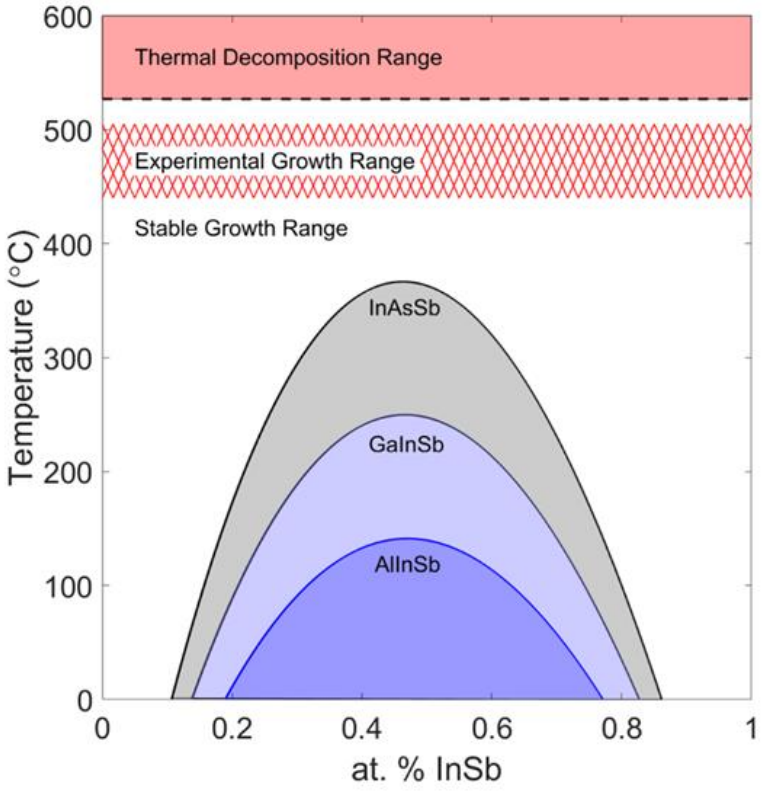

Figure 3.3: Theoretical spinodal decomposition ranges for the experimental ternary systems GaInSb, AlInSb, and InAsSb. The experimental growth range for these alloys is denoted by the cross-hatching between 440 °C and 505 °C.

According to these calculations, the minimum required growth temperatures to prevent spinodal decomposition at the most susceptible compositions are 141 °C for $Al_{52.6}In_{47.4}Sb$), 250 °C for $Ga_{53.1}In_{46.9}Sb$, and 367 °C for $InAs_{53.4}Sb_{46.6}$. These are metastable alloys that rely on the kinetic limiting of diffusion at low temperature to remain single-phase. The InAsSb alloys are in the greatest danger of spinodal decomposition when samples are cooled from their growth temperatures to room temperature for MBE chamber removal.

3.3 Thermal decomposition of ternary III-V alloys

During the initial growth of these ternary systems, it was found that a common form of failure was thermal decomposition. This effect occurred during growths as monitored by both pyrometry and RHEED, where upon passing a certain temperature threshold the crystalline quality would rapidly degrade. This effect corresponds to a significant increase in pyrometer signal with no corresponding heater output, as well as the vanishing of any RHEED pattern. This threshold was later identified as the melting point of the common constituent InSb at 527 °C. Growths which passed this threshold consistently produced XRD spectra with decomposed constituents.

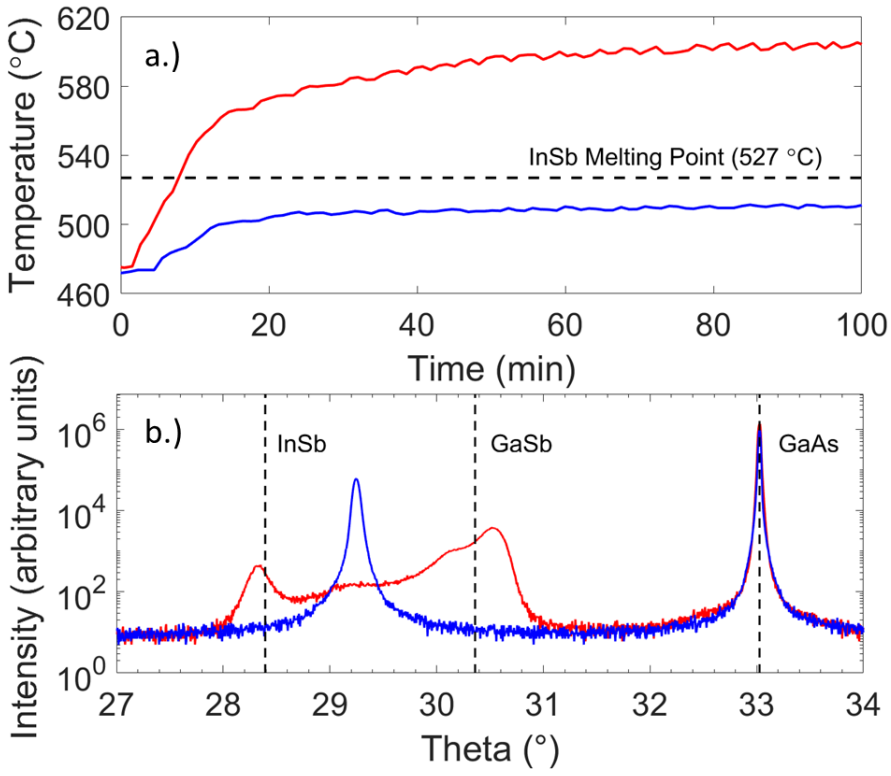

Figure 3.4: a.) *in situ* pyrometer signals of two InAsSb samples showing the behavior of thermal decomposition (red) and thermal stability (blue) during growth. b.) The corresponding X-ray diffraction III-V (004) peaks showing clear thermal decomposition leading to phase separation in the case that the melting point of InSb has been exceeded.

The continuing pyrometer temperature increase after passing the InSb melting point is in part due to roughening of the sample surface. Because the real sample temperature jumps quickly during ternary nucleation, these films are in danger of passing the thermal decomposition threshold if their initial growth temperature is too close to the InSb melting point. This extraordinary signal behavior acts as a good indicator that a ternary layer growth process has failed, and it has therefore facilitated the determination of the maximum initial growth temperatures for the three ternary systems.

3.4 Optimization of MBE parameters

The optimization of growth parameters during these ternary layer growths began with setting limits on the minimum and maximum growth temperatures. However, non-uniformity in substrate heating and pyrometer error both contribute to the danger of exceeding the thermal decomposition threshold when growth temperatures begin too close to it, so a 22 °C buffer was instituted to prevent exceeding the InSb melting point. In early experiments the radiative heating efficiency effect was the most common source of upper temperature limit overshoot. This required the further lowering of the maximal growth temperature for the alloys GaInSb and InAsSb to 500 °C and 460 °C respectively. Later growths also made use of pyrometer-corrected growth to lower substrate heater temperature in tandem with the rise in pyrometer signal during the increase in radiative heating efficiency. This allows for a raised maximal growth temperature closer to 505 °C once the substrate heater power has been lowered to account for the new efficiency.

The minimum growth temperatures for these alloys followed current group recipes and literature III-V MBE growth ranges for binary constituents (81–84). It should be noted that InSb is usually grown in the range of 360-400 °C, and so the quality of these InAsSb ternaries may be in part affected by the compromise between ideal InAs and InSb growth ranges. Higher temperatures are preferred for the maximization of final crystalline quality as seen in these experiments, so the primary mode of growth optimization became finding the maximum possible initial growth temperatures which would not facilitate thermal decomposition of the ternary alloys.

The V:III flux ratio is an important consideration for the growth of these alloys, although it is made simpler by the fact that they are grown in the desorptive range of the As_2 and Sb_2 source fluxes. A V:III flux ratio greater than unity is therefore applied in all of these growths to ensure that no metallic Group-III structures are formed. In practice, the V:III BEP ratio (as a proxy for

flux ratio) has ranged from 6-7 for early samples to 20 in later growths. No significant change in structural quality could be linked to these increases in BEP ratio beyond the minimum applied value. For comparison, some successful V:III BEP ratios in the literature are 3.4 for GaSb and 2.7 for InAs (85).

3.5 Structural characterization

3.5.1 Alloy composition and source parameters

The primary mode of ternary alloy composition estimation is through XRD analysis. Initial flux starting points for these ternaries were chosen for Group-V rich growth conditions. Following these attempts, the Group-III fluxes were readjusted until the target compositions with desired lattice constants were achieved. The primary sample set acquired and characterized in this way contains seventeen ternary films and their four binary constituents. Each system shows the combined data of several ternary films which are distinguished by their plot color, as well as binary films for each of the four alloying constituents. All plots are laterally shifted so that the experimental GaAs (004) peak matches its literature value. This corresponds with a maximum horizontal axis error of 14 arcsec.

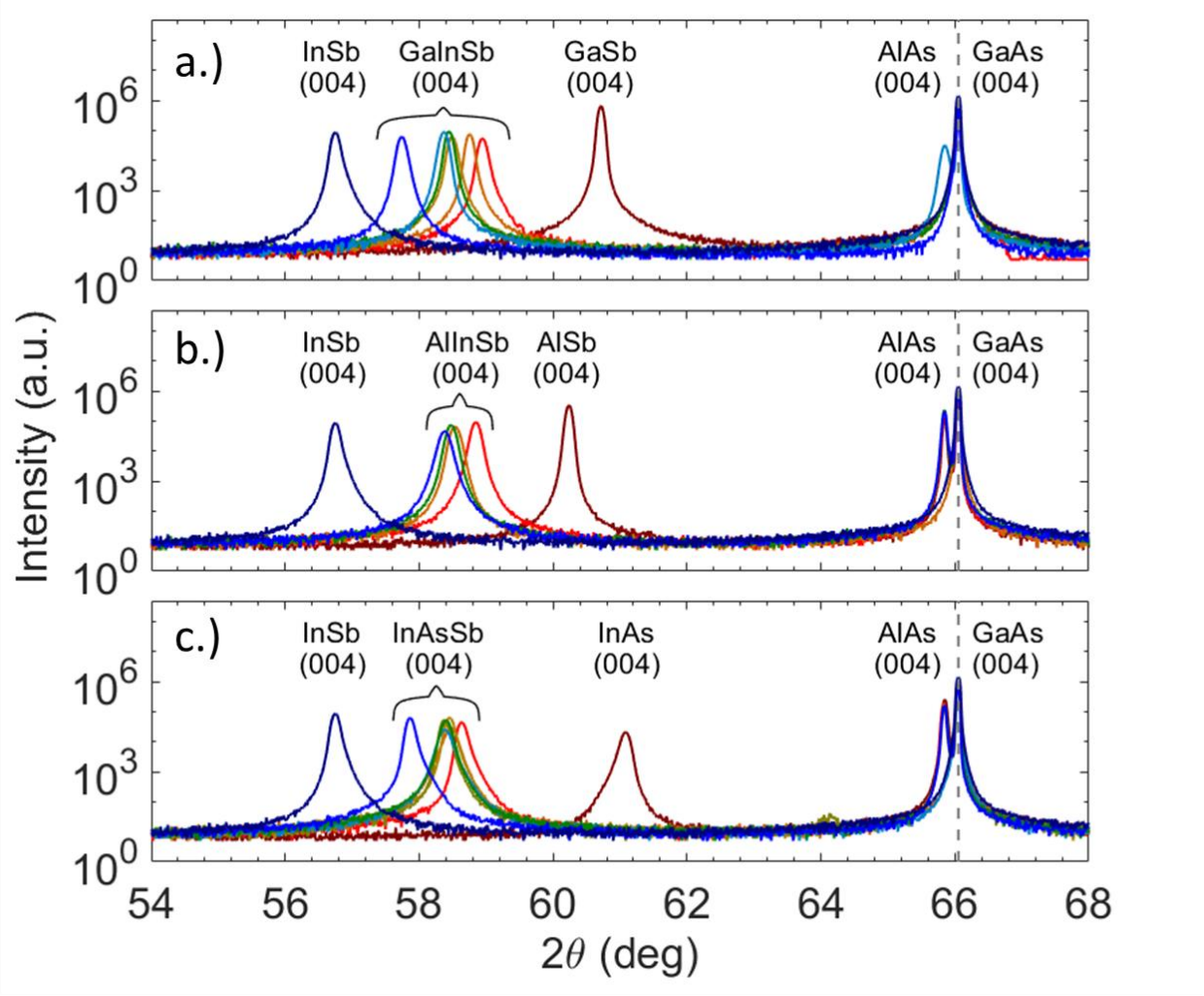

Figure 3.5: High-resolution X-ray diffraction (004) peak plots for samples in the GaInSb, AlInSb, and InAsSb ternary alloy systems. The gray dashed line marks the literature value of $2\theta = 33.026°$ for GaAs (004).

Here, multiple curves show the shifting of the ternary layer (004) peaks with respect to composition. These peaks are all within the bounds set by the (004) peak positions of their relevant binary constituents. The crystalline quality of these ternaries in Table 3.2, including the binary constituents, is measured through the FWHMs of their (004) peaks.

Table 3.2: Ternary alloy parameters including those derived from X-ray diffraction conducted after growth. The compositions listed here are calculated using the linear interpolation of binary constituent zinc blende a lattice parameters, following Vegard's law.

Experimental Alloy (2 μm)	Buffer (300 nm)	Alloy Growth Temperature (°C)	Alloy (004) Peak FWHM (arcsec)
$Ga_{56.6}In_{43.4}Sb$	GaAs	473	227
$Ga_{25.5}In_{74.5}Sb$	GaAs	473	227
$Ga_{51.6}In_{48.4}Sb$	GaAs	473	205
$Ga_{45.1}In_{54.9}Sb$	GaAs	473	227
$Ga_{41.9}In_{58.1}Sb$	AlAs	460	228
$Ga_{43.9}In_{56.1}Sb$	GaAs	460	207
$Al_{60.2}In_{39.8}Sb$	AlAs	460	243
$Al_{46.8}In_{53.2}Sb$	AlAs	460	290
$Al_{49.8}In_{50.2}Sb$	AlAs	500	255
$Al_{51.5}In_{48.5}Sb$	GaAs	500	279
$InAs_{26.3}Sb_{73.7}$	AlAs	460	225
$InAs_{44.5}Sb_{55.5}$	AlAs	460	249
$InAs_{38.3}Sb_{61.7}$	AlAs	460	240
$InAs_{40.1}Sb_{59.9}$	AlAs	440	247
$InAs_{39.0}Sb_{61.0}$	AlAs	440	270
$InAs_{38.5}Sb_{61.5}$	GaAs	440	332
$InAs_{40.7}Sb_{59.3}$	GaAs	440	325
GaSb	GaAs	505	173
AlSb	AlAs	500	169
InAs	AlAs	440	259
InSb	GaAs	505	220

The MBE-grown AlSb and GaSb films are of higher quality than their InAs and InSb counterparts. While the InSb shown here is grown at a higher temperature than within the common 360-400 °C range, it is more representative of the higher-temperature growth that occurs when it is grown as a constituent of the experimental ternary alloys.

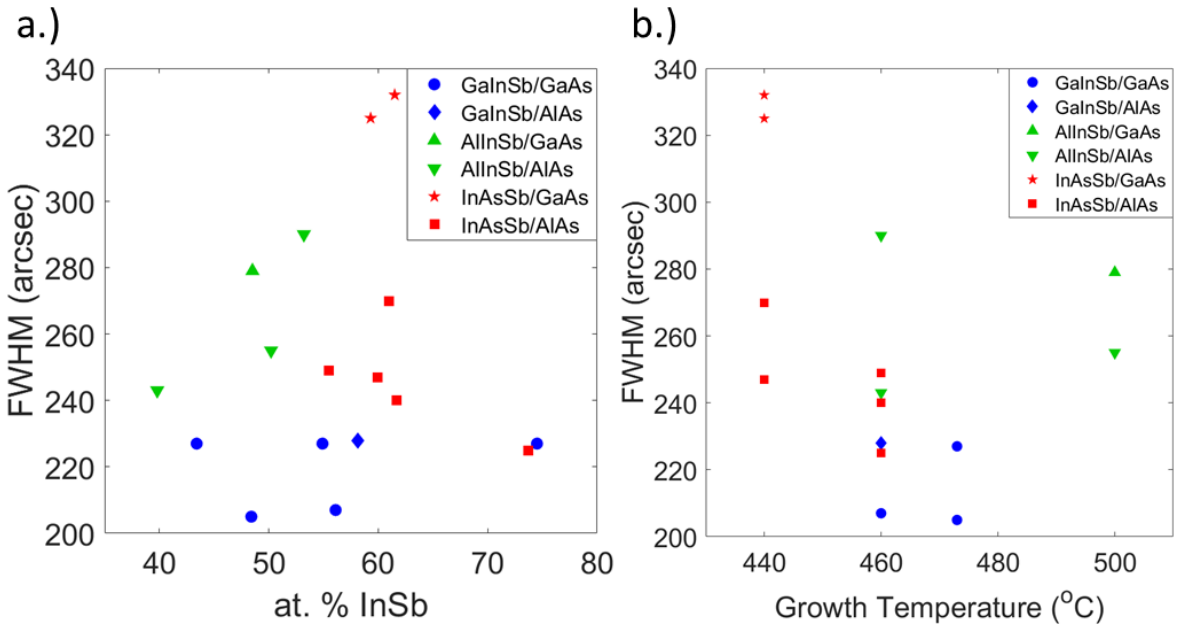

Figure 3.6: Full-widths at half-maxima of ternary buffers listed in Table 3.2 plotted with respect to both a.) composition and b.) growth temperature.

These results do not appear to show a strong trend matching crystalline quality (FWHM) with composition, growth temperature, nor choice of binary buffer. There is, however, a small reduction in AlInSb FWHM content with increasing AlSb alloy fraction. In addition, the InAsSb ternaries grown on AlAs are of higher quality those grown on GaAs, with FWHMs averaging 246 and 329 arcsec. It should be noted, however, that the InAsSb ternaries suffered from variation in quality in general over the course of these experiments, and that this is a relatively small sample set. Still, the consistency of quality across the range of ternary compositions bodes well especially for the use of GaInSb and AlInSb ternary layers with average FWHMs of 220 and 267 arcsec. These systems show no evidence of spinodal decomposition during cooldown as their ternary (004) peaks remain singular with no emergent binary constituent peaks or off-composition satellites.

3.5.2 Defect analysis through reciprocal space mapping

The RSMs in Figure 3.7 and Figure 3.8 show GaAs, AlAs, and ternary alloy $(\bar{2}\bar{2}4)$ peaks scanned from a single heterostructure. The dashed diagonal line in a.) is traced from the origin to the asymmetric GaAs $(\bar{2}\bar{2}4)$ peak, demarcating the line of relaxation. The GaInSb $(\bar{2}\bar{2}4)$ peak almost perfectly intersects this line, demonstrating the fully relaxed nature of the ternary layer.

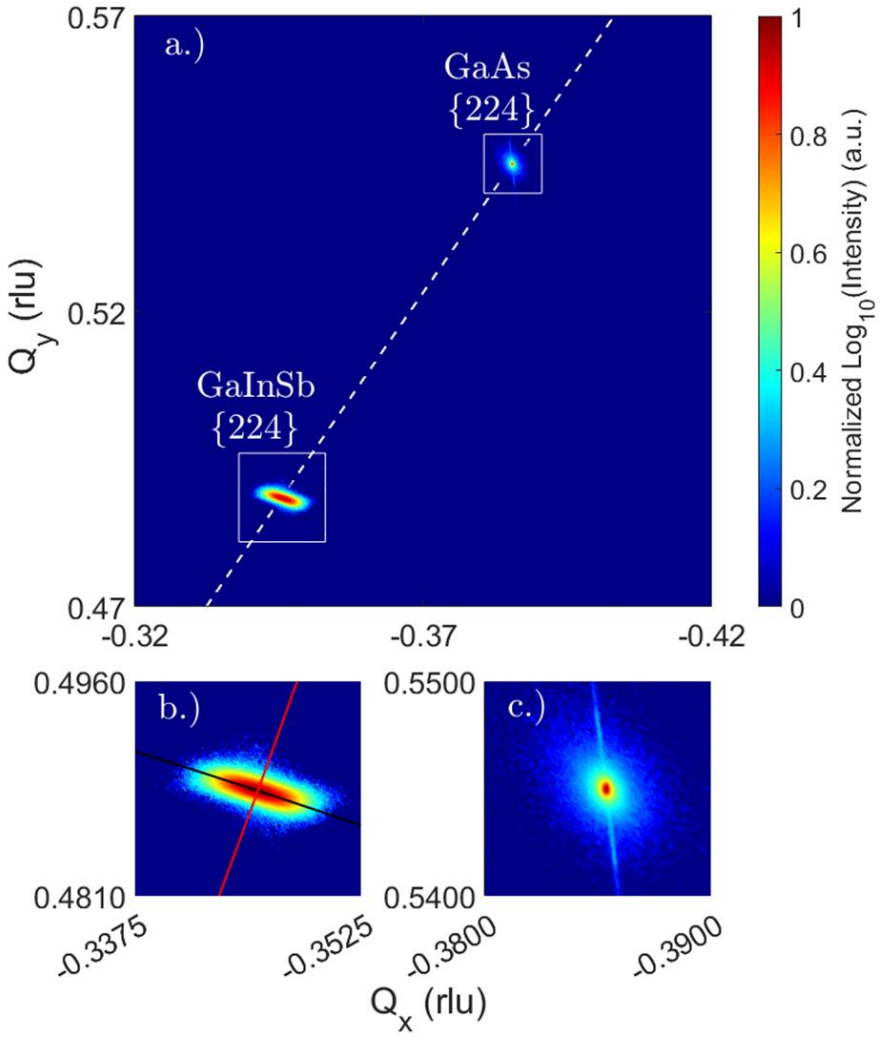

Figure 3.7: a.) Reciprocal space map of $Ga_{43.9}In_{56.1}Sb$ grown on a GaAs homomorphic buffer/GaAs (001). b.) and c.) show magnified maps of the GaInSb $(\bar{2}\bar{2}4)$ and GaAs $(\bar{2}\bar{2}4)$ peaks, respectively. The major (black) and minor (red) axes of the GaInSb $(\bar{2}\bar{2}4)$ spot are marked in b.).

Figure 3.8 shows the full RSMs of all six ternary/binary heterostructures. All dashed diagonal lines of relaxation trace from the origin to the GaAs substrate $(\bar{2}\bar{2}4)$ peak. In the case of AlAs pseudomorphic binary buffers there is a distinct, smaller AlAs $(\bar{2}\bar{2}4)$ peak which is vertically offset ($-Q_y$ direction) from the bulk substrate GaAs $(\bar{2}\bar{2}4)$ peak. The Q_x and Q_y coordinates of all data are shifted so that the experimental GaAs $(\bar{2}\bar{2}4)$ peak corresponds to the reciprocal lattice coordinates of the cubic crystal with a literature-value lattice a parameter of 5.65368 Å.

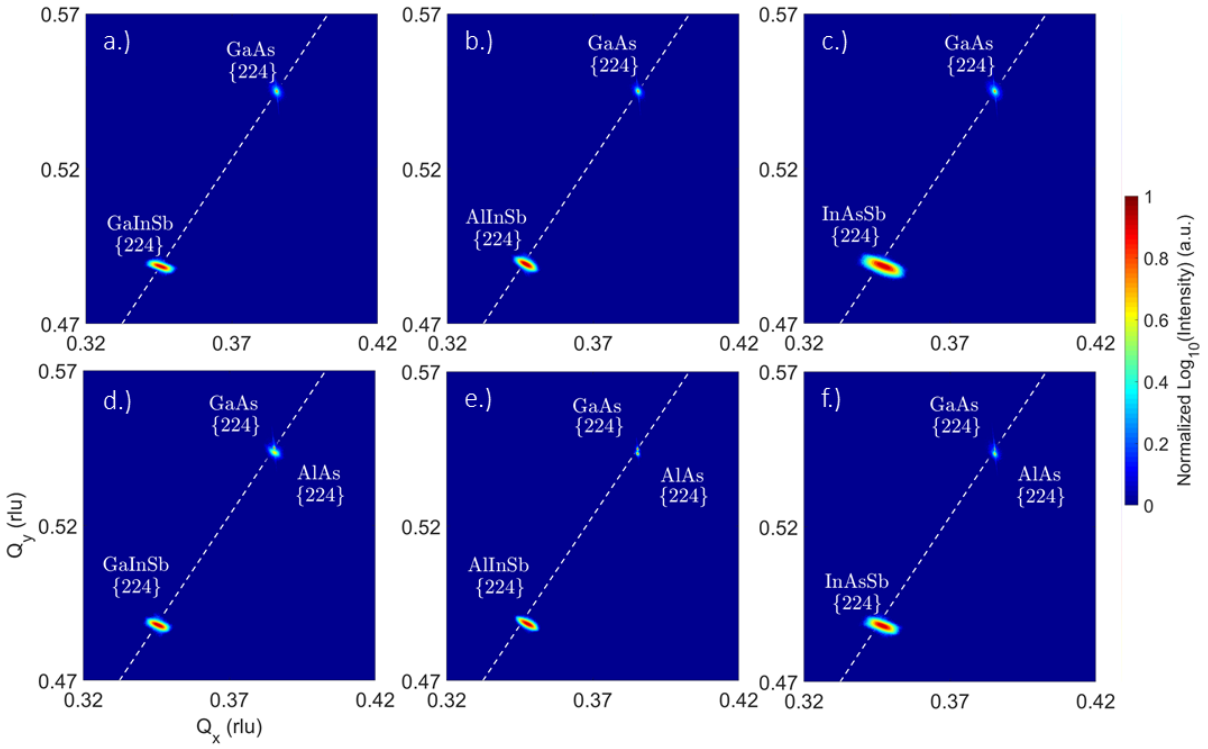

Figure 3.8: Asymmetric reciprocal space maps of all six ternary/binary permutations a.) GaInSb/GaAs, b.) AlInSb/GaAs, c.) InAsSb/GaAs, d.) GaInSb/AlAs, e.) AlInSb/AlAs, and f.) InAsSb/AlAs.

Figure 3.9 shows a magnified image of a heterostructure a featuring both AlAs $(\bar{2}\bar{2}4)$ and GaAs $(\bar{2}\bar{2}4)$ (Figure 3.8e). The scan area in Q-space is relatively small as zinc blende GaAs and AlAs have very similar lattice parameters.

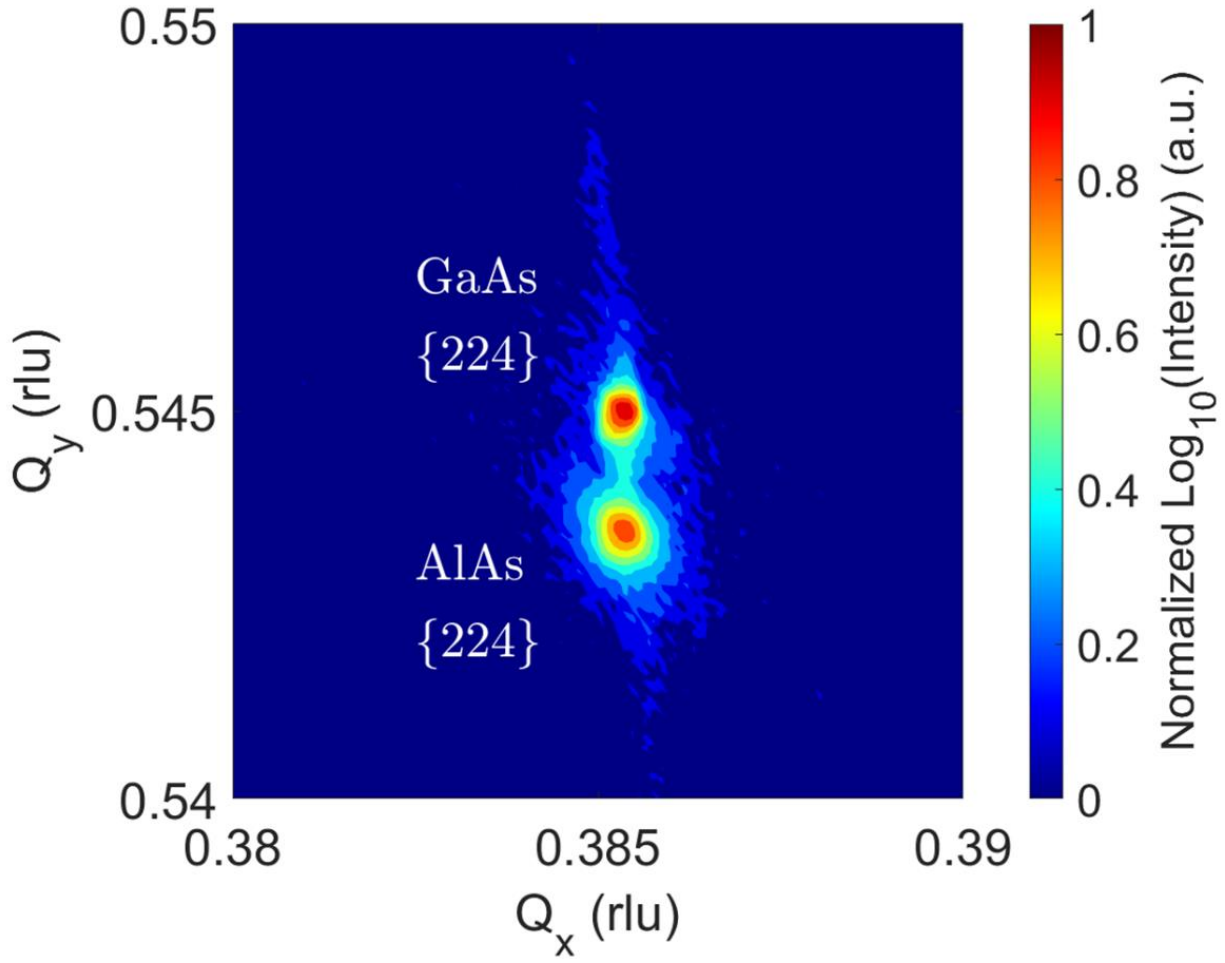

Figure 3.9: Magnified reciprocal space map of AlInSb/AlAs/GaAs (001) (Figure 3.8e) showing the AlAs $(\bar{2}\bar{2}4)$ and GaAs substrate $(\bar{2}\bar{2}4)$ peaks.

RSM is used to assess the degree of strain, and therefore the relaxation in these films. The in-plane and out-of-plane lattice parameters should be nearly identical for relaxed films and can be assessed for these cubic ternaries without knowing their bulk lattice constants. As shown in Table 3.3, the lattice parameters and the corresponding in-plane strains are catalogued. The stiffness matrix constants taken are from *Vurgaftman et al.* and are linearly interpolated (86). There is a slight mismatch between the a lattice parameters of the zinc blende GaAs and AlAs crystals, which are 5.65330 Å and 5.66139 Å (47). Following the pseudomorphic growth of an AlAs binary on GaAs (001), only the Q_y coordinate should show disparity as the buffer will be strained in-plane to match the a parameter of the GaAs substrate. This is indeed the case as shown in Figure 3.9 where the Q_x coordinates of the peaks are extremely close. The AlAs $(\bar{2}\bar{2}4)$ peaks exist at a smaller, positive Q_y coordinate in reciprocal space corresponding to their larger, real out-of-plane lattice parameter.

Table 3.3: Reciprocal space map-derived lattice parameters for ternary alloy samples grown on both GaAs and AlAs binary buffers. The in-plane strain is calculated from these values.

Experimental Heterostructure	In-Plane Lattice Parameter (Å)	Out-of-Plane Lattice Parameter (Å)	In-Plane Strain
$Ga_{43.9}In_{56.1}Sb/GaAs$	6.2967	6.3109	-1.1261E-03
$Ga_{41.9}In_{58.1}Sb/AlAs$	6.2916	6.3185	-2.1290E-03
$Al_{51.5}In_{48.5}Sb/GaAs$	6.2690	6.3022	-2.5984E-03
$Al_{49.8}In_{50.2}Sb/AlAs$	6.2728	6.3081	-2.7584E-03
$InAs_{40.7}Sb_{59.3}/GaAs$	6.2690	6.3081	-2.9766E-03
$InAs_{39.0}Sb_{61.0}/AlAs$	6.2753	6.3152	-3.0342E-03

These RSM peaks offer more in terms of ternary film defect analysis following the work of *Kaganer et al.*, which mathematically links the ratio of the FWHMs of the Gaussian RSM peaks to the densities of pure edge and mixed dislocations in their crystals (74). There is a minimum ellipticity associated with the formation of a metamorphic interface composed entirely of misfit dislocations. The deviation in experimental spot ellipticity from the minimum ellipticity of the idealized model is an indicator of sample quality, as it pertains to the increase in dislocations with screw-like character. The Gaussian in-plane width parameter,

$$w_{x,edge} = \frac{\rho Q_y^2 b_x^2}{8\pi d}, \tag{3.4}$$

is determined by the FWHM taken parallel to $\vec{Q}_x$ for a (004) symmetric RSM. Similarly, the Gaussian out-of-plane width parameter,

$$w_{y,edge} = \left[\frac{\nu}{(1-\nu)}\right]^2 \frac{\rho Q_y^2 b_x^2}{4\pi d}, \tag{3.5}$$

is determined by the FWHM taken parallel to $\vec{Q}_y$. The linear density of misfit dislocations ρ along the ternary/binary III-V interface and the metamorphic ternary thickness d produce the parameter ρd which correlates with the level of strain. When $\rho d \gg 1$, as in these completely relaxed ternary films, the theoretical shape of their RSM spots may be accurately approximated using this theory. The in-plane Burgers vector b_x is $\langle 110 \rangle$-type for these zinc blende systems. It is equal to $a/\sqrt{2}$ (87). The ratio of the Gaussian width parameters:

$$\left[\frac{1-\nu}{\sqrt{2}\nu}\right]^2, \tag{3.6}$$

is independent of thickness and misfit dislocation density. In contrast to the parameters of the pure misfit dislocation case, the Gaussian width parameters for an array of mixed dislocations are:

$$w_{x,mixed} = \frac{\rho Q_y^2 \left(b_x^2 + 5b_y^2\right)}{8\pi d}, \tag{3.7}$$

and

$$w_{y,mixed} = \left[\frac{\nu}{(1-\nu)}\right]^2 \frac{\rho Q_y^2 \left(b_x^2 + b_y^2\right)}{4\pi d}. \tag{3.8}$$

The ratio of the Gaussian width parameters now becomes:

$$\frac{w_{x,mixed}}{w_{y,mixed}} = \frac{b_x^2 + 5b_y^2}{b_x^2 + b_y^2}\left[\frac{1-\nu}{\sqrt{2}\nu}\right]^2. \tag{3.9}$$

The first term in the ratio containing the Burgers vectors is equal to or greater than unity in all cases. This causes the ratio $w_{x,mixed}/w_{y,mixed}$ to always be equal to or greater than the ideal case ratio $w_{x,edge}/w_{y,edge}$. RSMs of the symmetric (004) peaks for these ternary samples are therefore taken to determine the FWHMs of the their major and minor 2D cross-sections. Their ratio $FWHM_x/FWHM_y$, which is equal to $w_{x,mixed}/w_{y,mixed}$, is compared to the theoretical ideal ratio $w_{x,edge}/w_{y,edge}$. The RSMs of six experimental heterostructures covering the permutations of three ternary alloys and two binary buffers are subjected to this analysis.

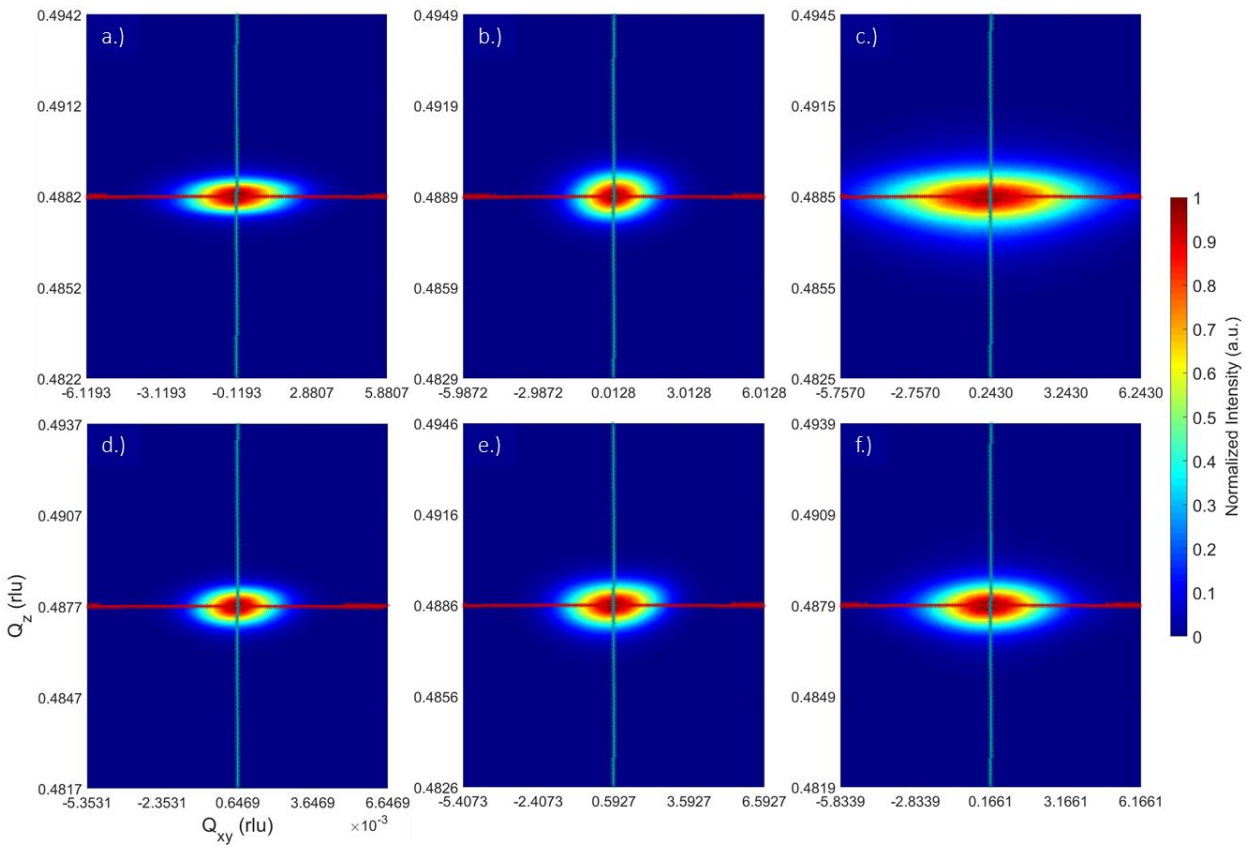

Figure 3.10: Symmetric reciprocal space maps of all six ternary/binary permutations a.) GaInSb/GaAs, b.) AlInSb/GaAs, c.) InAsSb/GaAs, d.) GaInSb/AlAs, e.) AlInSb/AlAs, and f.) InAsSb/AlAs. The major and minor axes of these ellipses are represented by red and teal lines, respectively.

Cross-sections of the major and minor axes of these heterostructures further illustrate the ellipticity of these RSM peaks. The method of FWHM determination through 1D Gaussian fitting is also shown in Figure 3.11. The cross sections are centered at zero along their relevant Q-space axes for easier comparison by eye.

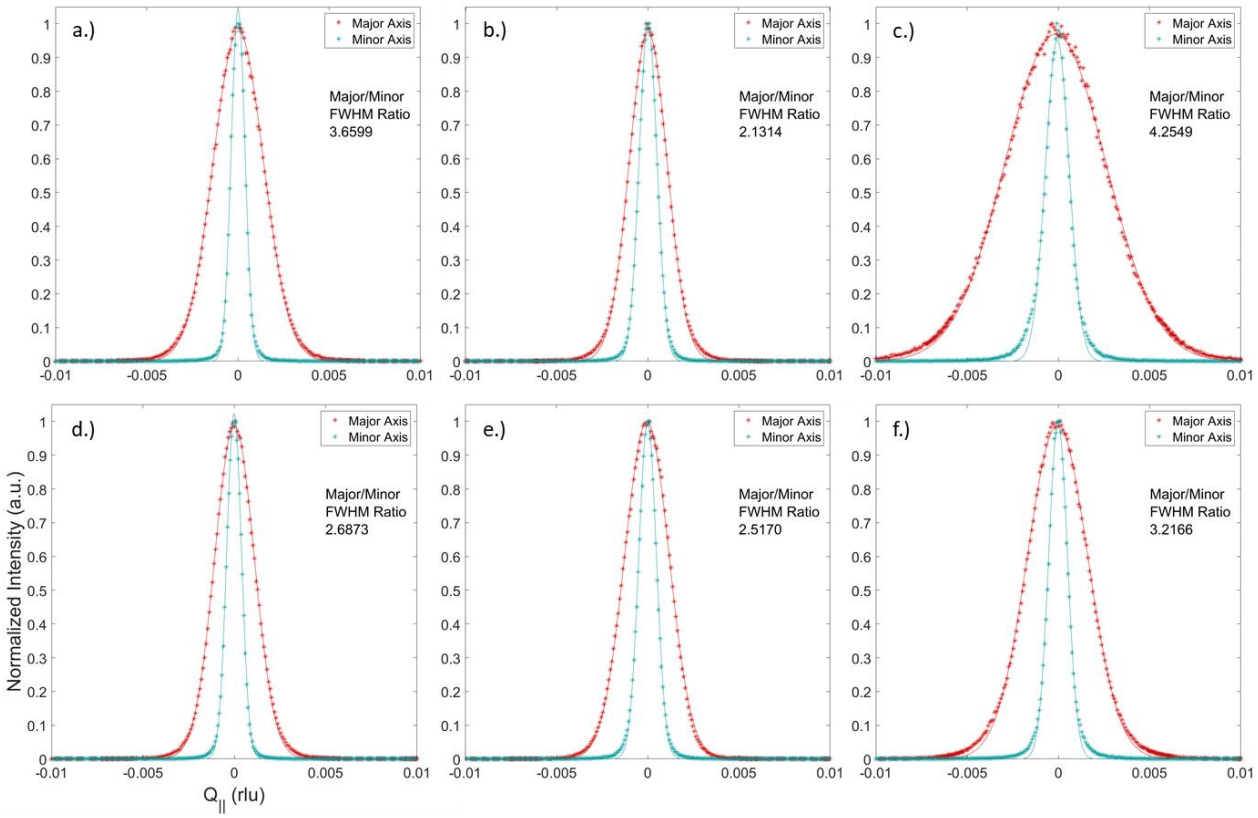

Figure 3.11: Cross sections of major (red) and minor (teal) reciprocal space map spot axes. These plots represent a.) GaInSb/GaAs, b.) AlInSb/GaAs, c.) InAsSb/GaAs, d.) GaInSb/AlAs, e.) AlInSb/AlAs, and f.) InAsSb/AlAs. The full-widths at half-maxima of these cross-sections are used to calculate the experimental full-width at half-maximum ratios in Table 3.4.

Table 3.4 contains the experimental and theoretical FWHM ratios, which are equal to the Gaussian width parameter ratios, and the percent deviation of the experimental from the ideal is calculated. While the percent deviation cannot be directly tied to a specific crystal defect type such as threading dislocations, stacking faults, or decomposition, it is still a valuable process variable in terms of sample growth condition refinement. For example, the AlInSb samples here are clearly most in line with their theoretical ideal misfit dislocation value, followed by GaInSb and then InAsSb.

Table 3.4: Theoretical in-plane/out-of-plane Gaussian Full-Width at Half-Maximum (FWHM) ratios for the metamorphically-grown ternary heterostructures in the ideal pure misfit edge dislocation scenario and the tabulation of corresponding experimental FWHM ratios. The percent difference between the theoretical and experimental cases is also calculated.

Experimental Heterostructure	Theoretical Ideal FWHM Ratio	Experimental FWHM Ratio	Percent Difference (%)
$Ga_{43.9}In_{56.1}Sb/GaAs$	1.418	3.660	158.1
$Ga_{41.9}In_{58.1}Sb/AlAs$	1.413	2.687	90.16
$Al_{51.5}In_{48.5}Sb/GaAs$	1.376	2.131	54.87
$Al_{49.8}In_{50.2}Sb/AlAs$	1.374	2.517	83.19
$InAs_{60.7}Sb_{59.3}/GaAs$	1.314	4.255	223.8
$InAs_{39.0}Sb_{61.0}/AlAs$	1.315	3.217	144.6

3.5.3 Surface character of virtual substrates

Both RHEED and AFM provide data on the ultimate surface character of these ternary III-V alloys as they pertain to growth temperature, binary buffer selection, and XRD-derived crystalline quality (through FWHM). RHEED is primarily analyzed for the surface reconstructions of these ternary alloys for comparison with the literature patterns of their primary constituents. Figure 3.12 shows three representative RHEED patterns derived from GaInSb, AlInSb, and InAsSb which have just finished deposition and are still at the growth temperature.

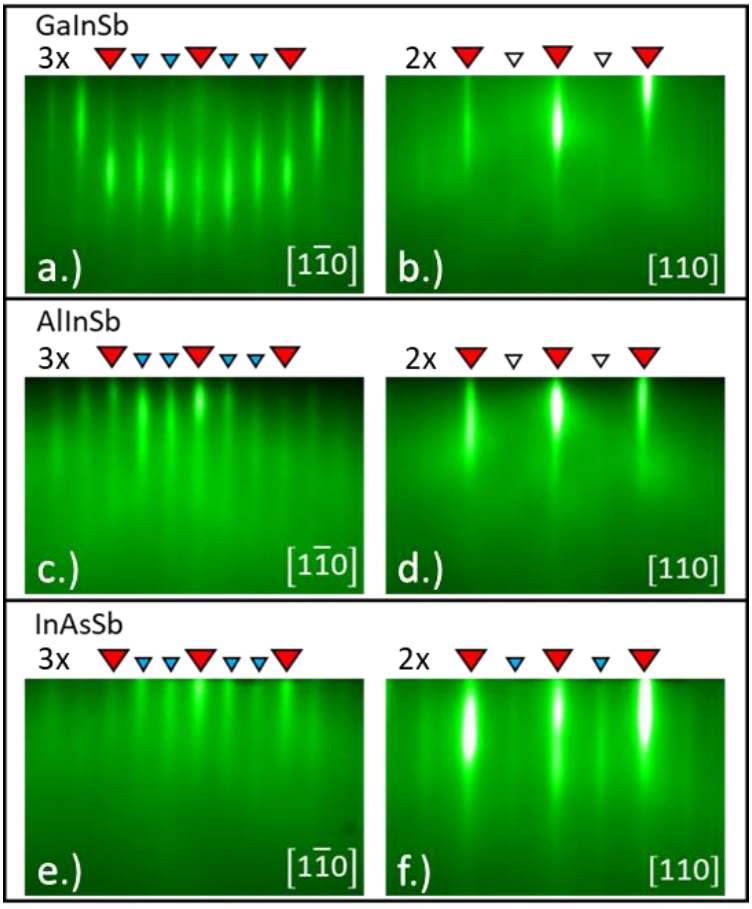

Figure 3.12: a-b.) $Ga_{0.43}In_{0.57}Sb$, c-d.) $Al_{0.48}In_{0.52}Sb$, and e-f.) $In_{0.38}As_{0.62}Sb$ surface reconstructions. The 2× patterns are taken at 90° rotations from their 3× counterparts. Primary (red), clear secondary (blue), and faint secondary (white) diffraction streaks are marked.

These surface reconstructions are doubly useful in that their absence provides evidence of poor growth conditions and that their nature is a consideration for the epitaxial growth of an overlayer. All three ternary alloys exhibit a (2×3) surface reconstruction so long as neither spinodal nor thermal decomposition occur. However, the binary constituents GaSb and AlSb are reported to exhibit (1×3) reconstructions over similar temperature and pressure ranges as the ternary alloy growths (88,89). InAs deviates even more from its ternary alloy, as it is nominally a (2×4) reconstruction (89). These ternary surface reconstructions may be altered by their common InSb constituent, which exhibits a pseudo-(1×3) reconstruction generated by the superstructure combination of its (2×4) phases (90,91). However, the ternary reconstructions featured here do not show the same pseudo-pattern behavior as InSb where the streaks are not equally spaced. Instead, the 3× streaks are clear and equidistant in all cases. The 2× streaks are a bit more diverse, as GaInSb an AlInSb do not show the same intensity in their minor streaks as with InAsSb. Still, the full (2×3) pattern is visible in all three cases. No discernment in surface reconstruction could be made between layers of the same ternary system grown on either homomorphic GaAs or pseudomorphic AlAs buffers.

Figure 3.13 shows three representative AFM images of the GaInSb, AlInSb, and InAsSb ternary alloy systems.

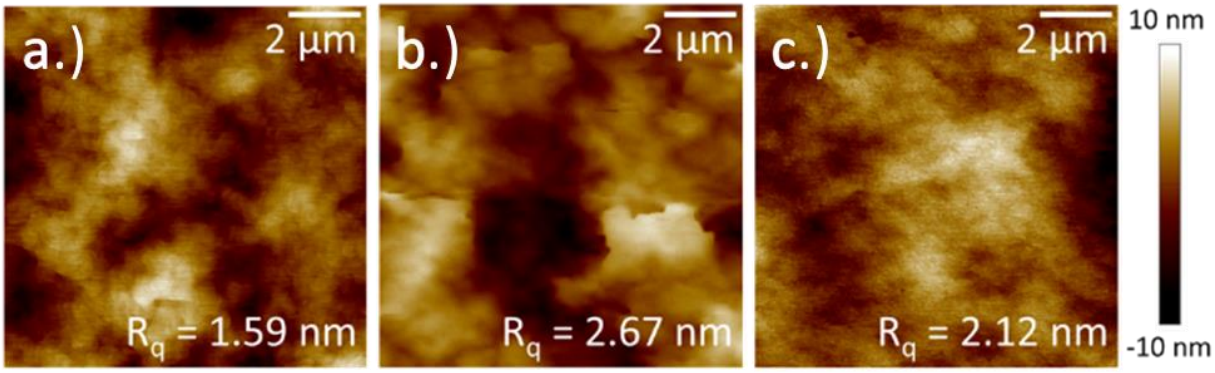

Figure 3.13: 10×10 µm atomic force microscopy images of the ternary III-V alloys a.) $Ga_{0.43}In_{0.57}Sb$, b.) $Al_{0.48}In_{0.52}Sb$, and c.) $InAs_{0.36}Sb_{0.64}$. Root mean square roughness values (R_q) for each sample are listed in their respective figures.

In all cases, mounded 3D growth is apparent and there are no visible islands or step edges even over smaller scan areas. The root mean square roughnesses R_q in Table 3.5 vary quite significantly even across samples in the same ternary system. It appears as though growth conditions have a strong effect on the final roughness and that the current recipes are not fully optimized. The most variation exists across the samples of the InAsSb system. The growth temperatures for this system are the lowest amongst the three, which necessarily lowers the diffusion rate of atoms across the sample surface during growth. It would be prudent to grow a selection of InAsSb alloys at higher temperatures to see if the surface roughnesses produced there are on the order of those found in the GaInSb and AlInSb samples.

Table 3.5: Atomic force microscopy derived Root Mean Square (RMS) R_q values of ternary alloys in comparison to composition, binary buffer system, and growth temperature.

Experimental Alloy (2 µm)	Buffer (300 nm)	Alloy Growth Temperature (°C)	RMS Roughness (10×10 µm^2, R_q, nm)
$Ga_{56.6}In_{43.4}Sb$	GaAs	473	1.85
$Ga_{25.5}In_{74.5}Sb$	GaAs	473	3.47
$Ga_{51.6}In_{48.4}Sb$	GaAs	473	1.32
$Ga_{45.1}In_{54.9}Sb$	GaAs	473	1.54
$Ga_{41.9}In_{58.1}Sb$	AlAs	460	5.07
$Ga_{43.9}In_{56.1}Sb$	GaAs	460	1.55
$Al_{60.2}In_{39.8}Sb$	AlAs	460	3.26
$Al_{46.8}In_{53.2}Sb$	AlAs	460	6.89
$Al_{49.8}In_{50.2}Sb$	AlAs	500	2.67
$Al_{51.5}In_{48.5}Sb$	GaAs	500	3.33
$InAs_{26.3}Sb_{73.7}$	AlAs	460	6.40
$InAs_{44.5}Sb_{55.5}$	AlAs	460	5.62
$InAs_{38.3}Sb_{61.7}$	AlAs	460	2.12
$InAs_{40.1}Sb_{59.9}$	AlAs	440	3.89
$InAs_{39.0}Sb_{61.0}$	AlAs	440	5.50
$InAs_{38.5}Sb_{61.5}$	GaAs	440	6.27
$InAs_{40.7}Sb_{59.3}$	GaAs	440	11.6

3.5.4 Analysis of electron micrographs

TEM was conducted on three representative ternary alloy samples: GaInSb, AlInSb, and InAsSb on homomorphic GaAs buffers. These micrographs and the calculations of their defect densities were produced by Edwin Supple and Brian P. Gorman at Colorado School of Mines. Samples underwent focused ion beam milling followed by lift-out to produce TEM-worthy lamella with thicknesses of 251 nm ($Ga_{43.9}In_{56.1}Sb$), 168 nm ($Al_{51.5}In_{48.5}Sb$), and 207 nm ($InAs_{40.7}Sb_{59.3}$). Gas injection was used to coat the lamella in conducting Pt to prevent charging during imaging. The Pt appears dark in contrast to the heterostructure layers in the TEM micrographs. Striations in the lamella are parallel to the plane-normal, and are mechanically derived from the sample preparation process. The thickness range allows for TDD counting through the entire ternary layer as the electron beam is capable of passing through the sample while enough thickness is left to give consistent and reasonable densities. Five images per sample produced TDD counts at the layer midpoints (50% ternary thickness) and near the heterostructure surfaces (95% ternary thickness) for a total of thirty total density counts. The averages of each five-image set are divided by their respective cross-sectional (in-plane) areas to give an estimate of TDD as shown in Table 3.6.

Table 3.6: Threading dislocation densities and their standard deviations (σ) derived from transmission electron microscopy of GaInSb. AlInSb, and InAsSb films approximating 1.5-2 μm in thickness.

Experimental Alloy	TDD at 50 % thickness (cm^{-2})	σ at 50 % thickness (cm^{-2})	TDD at 95 % thickness (cm^{-2})	σ at 95 % thickness (cm^{-2})
$Ga_{43.9}In_{56.1}Sb$	4.27×10^9	8.58×10^8	3.26×10^9	6.98×10^8
$Al_{51.5}In_{48.5}Sb$	7.16×10^9	1.92×10^9	2.20×10^9	8.04×10^8
$InAs_{40.7}Sb_{59.3}$	3.57×10^9	1.06×10^9	2.97×10^9	1.28×10^9

This cross-sectional area is the image width multiplied by a depth determined geometrically from the film thickness and the angle of the sample with respect to the imaging plane. The standard deviations made available through the use of multiple images are also included, and are significant with respect to their TDDs. A greater number of images would produce a more refined result with smaller deviations, but the general conclusion would remain the same: that these measured TDDs are much larger than typical TDDs in the range of 10^6-10^7 cm^{-2} (78,92).

The crystalline mistilts with respect to the substrate normal along [001] towards $[01\bar{1}]$ were also determined. They are 10°, 4°, and 0° towards $[01\bar{1}]$ for $Ga_{43.9}In_{56.1}Sb$, $Al_{51.5}In_{48.5}Sb$, and $InAs_{40.7}Sb_{59.3}$. The TEM images do not show evidence of phase separation in these ternaries even though they are below their theoretical spinodal decomposition temperatures. Regions with significant atomic (Z) contrast in the images would suggest that phase separation has occured, but the lamella are homogenous. There are regions which appear brighter than the matrix along the surface normal [001], but this effect is due to the milling process and is known as curtaining. Contrast distortion near clusters of dislocations is visible, particularly in the $Al_{51.5}In_{48.5}Sb$ micrograph. Two consistent dislocation directionalities are identified in these images. Those parallel to the surface normal are necessarily ⟨100⟩-type. Threading dislocations run along the {111} planes of the zinc blende ternary alloys, so they appear at a 45° angle from the surface normal.

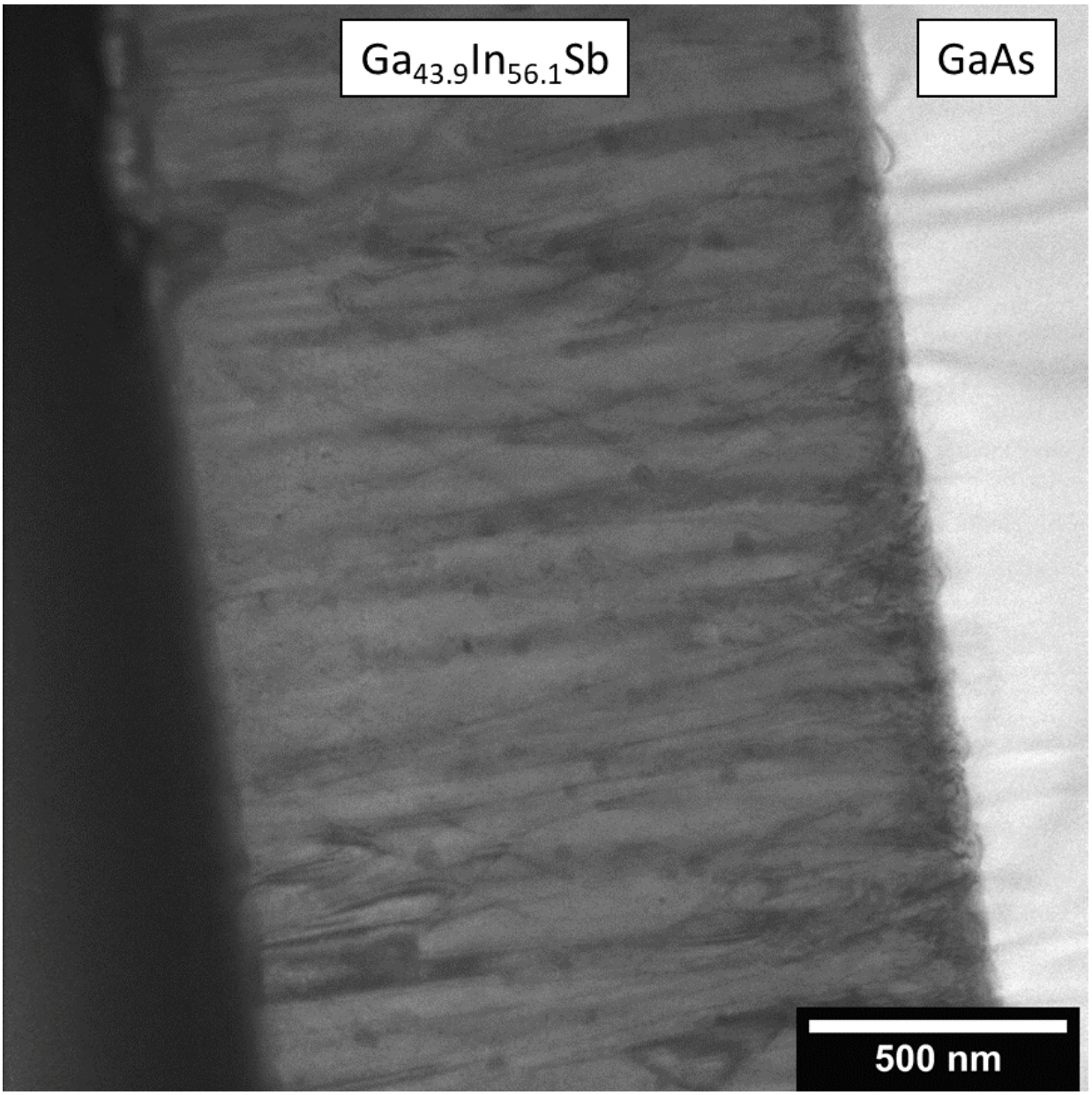

Figure 3.14: High-magnification transmission electron micrograph of $Ga_{43.9}In_{56.1}Sb$ deposited on GaAs/GaAs (001). Threading dislocations appear as thin, dark lines in the ternary layer.

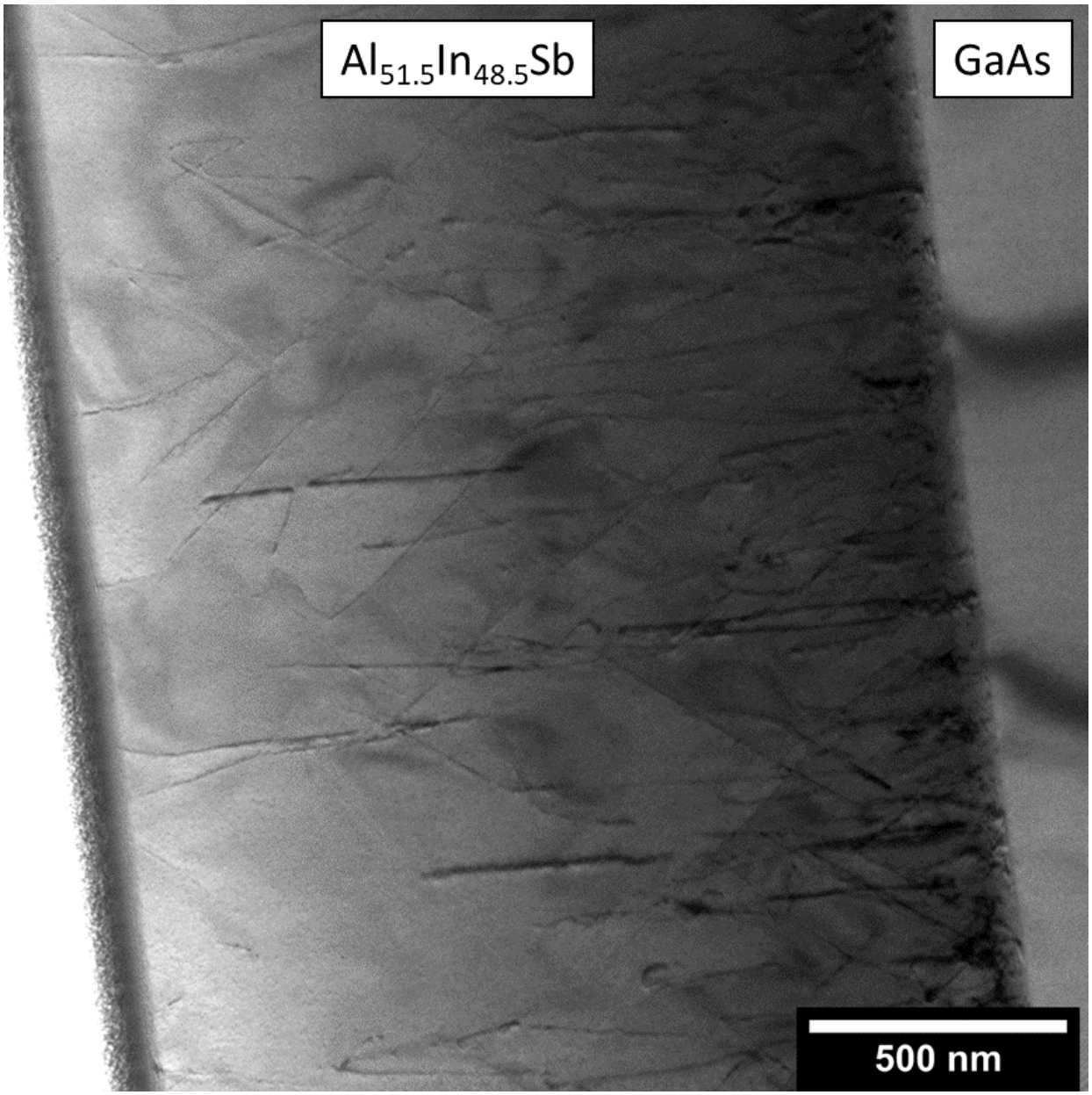

Figure 3.15: High-magnification transmission electron micrograph of $Al_{51.5}In_{48.5}Sb$ deposited on GaAs/GaAs (001). Threading dislocations appear as dark grooves in the ternary layer.

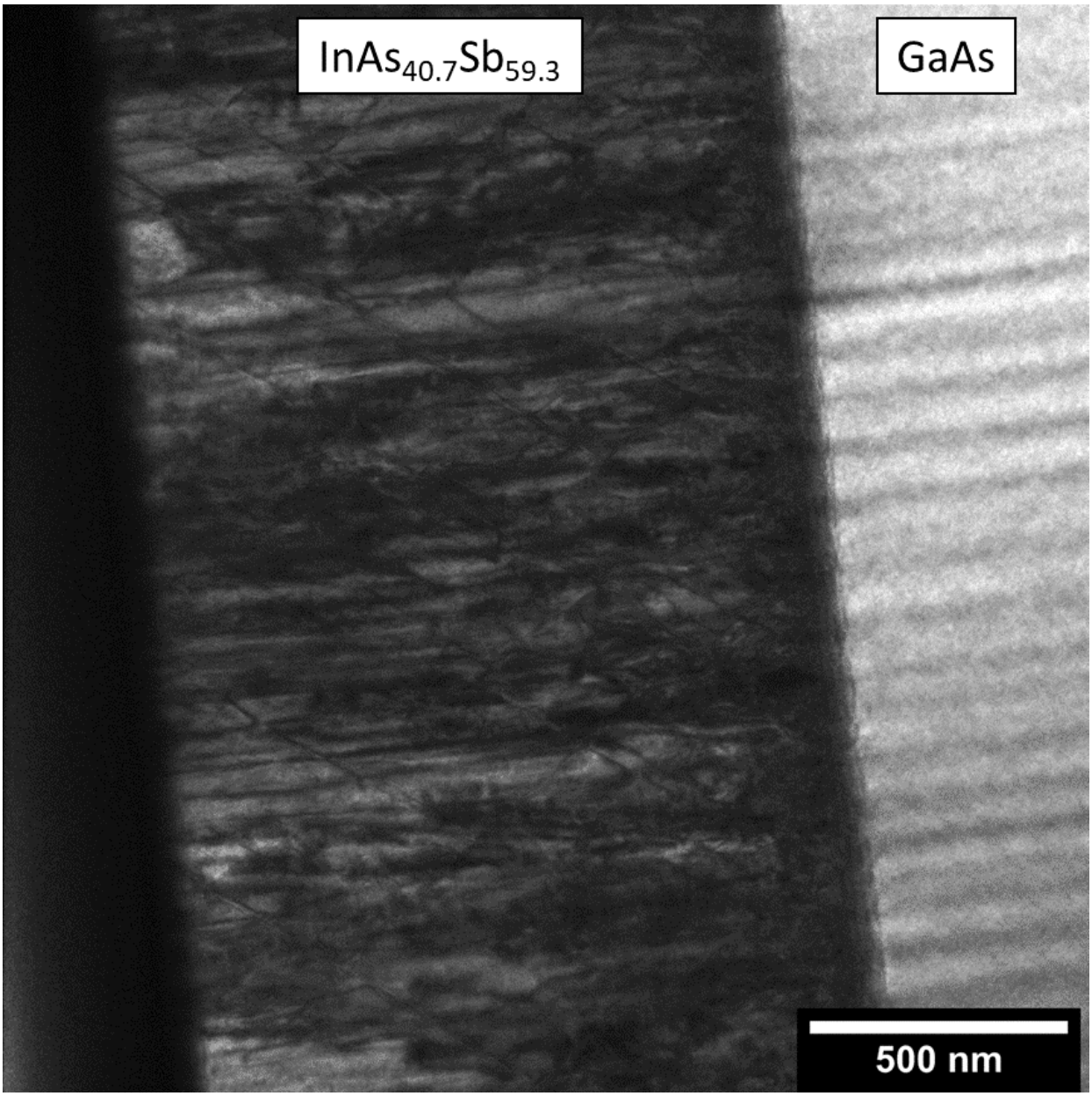

Figure 3.16: High-magnification transmission electron micrograph of $InAs_{40.7}Sb_{59.3}$ deposited on GaAs/GaAs (001). Threading dislocations appear as dark lines which are somewhat occluded by contrast in the ternary layer.

Chapter 4: Growth of Topological Semimetal Cadmium Arsenide

4.1 Gibbs free energy considerations

The potential interaction between a Cd_3As_2 layer its ternary III-V buffer, as well as As_2 and Sb_2 overpressures, were calculated via Gibbs free energy equations following the DLP model over a range 100-600 °C. The motivation for these calculations is the avoidance of intermixing at the interface which may lead to the formation of threading dislocations. Ternary alloy atoms which substitute into the Cd_3As_2 overlayer may also quench its topological character by modifying its crystal structure, particularly through the breaking of rotational symmetry. The thermodynamic data for the considered reactions are taken from literature sources on the enthalpies and entropies of arsenides and antimonides (79,80). The arsenide data is temperature-independent, but the antimonide data is given in 100 °C increments along with points at relevant phase changes. These calculations are conducted for the lattice-matched ternary compositions $Al_{0.47}In_{0.53}Sb$, $Ga_{0.42}In_{0.58}Sb$, and $InAs_{0.39}Sb_{0.61}$. Variance in the specific compositions of these ternaries will have an effect on the final Gibbs free energies of their proposed reactions. Therefore, the full composition windows are considered for reactions which have exothermic energies regarding the lattice matched compositions.

Chemical interactions at the Cd_3As_2-AlInSb interface are considered first. Here, the low-temperature interaction between any As_2 overpressure and the ternary AlInSb alloy must be considered as in:

$$Al_xIn_{1-x}Sb + 1/2\,As_2 \rightarrow Al_xIn_{1-x}As + 1/2\,Sb_2. \quad (4.1)$$

This reaction is relevant as additional As_2 overpressure is applied during one of the Cd_3As_2 growth series. The danger is the formation of AlInAs at the interface which would no longer be lattice matched with the intended Cd_3As_2 overlayer. The reactions:

$$Al_xIn_{1-x}Sb + Cd_3As_2 + 1/6\,As_2 \rightarrow Al_xIn_{1-x}As + Cd_3As_{1.33}Sb, \quad (4.2)$$

and

$$Al_xIn_{1-x}Sb + Cd_3As_2 \rightarrow Al_xIn_{1-x}As + Cd_{2.5}AsSb + Cd_{0.5}, \quad (4.3)$$

consider diffusion between the Cd_3As_2 and AlInSb layers both with and without the presence of latent As_2 overpressure. These reactions are highly unfavorable over the considered temperature range, boding well for the use of AlInSb as a stable buffer for Cd_3As_2 overlayer growth. Discrete jumps in the curves appear most noticeably in Figure 4.1a. These are due to changes in the enthalpy of compound formation when one of its constituents undergoes a phase change.

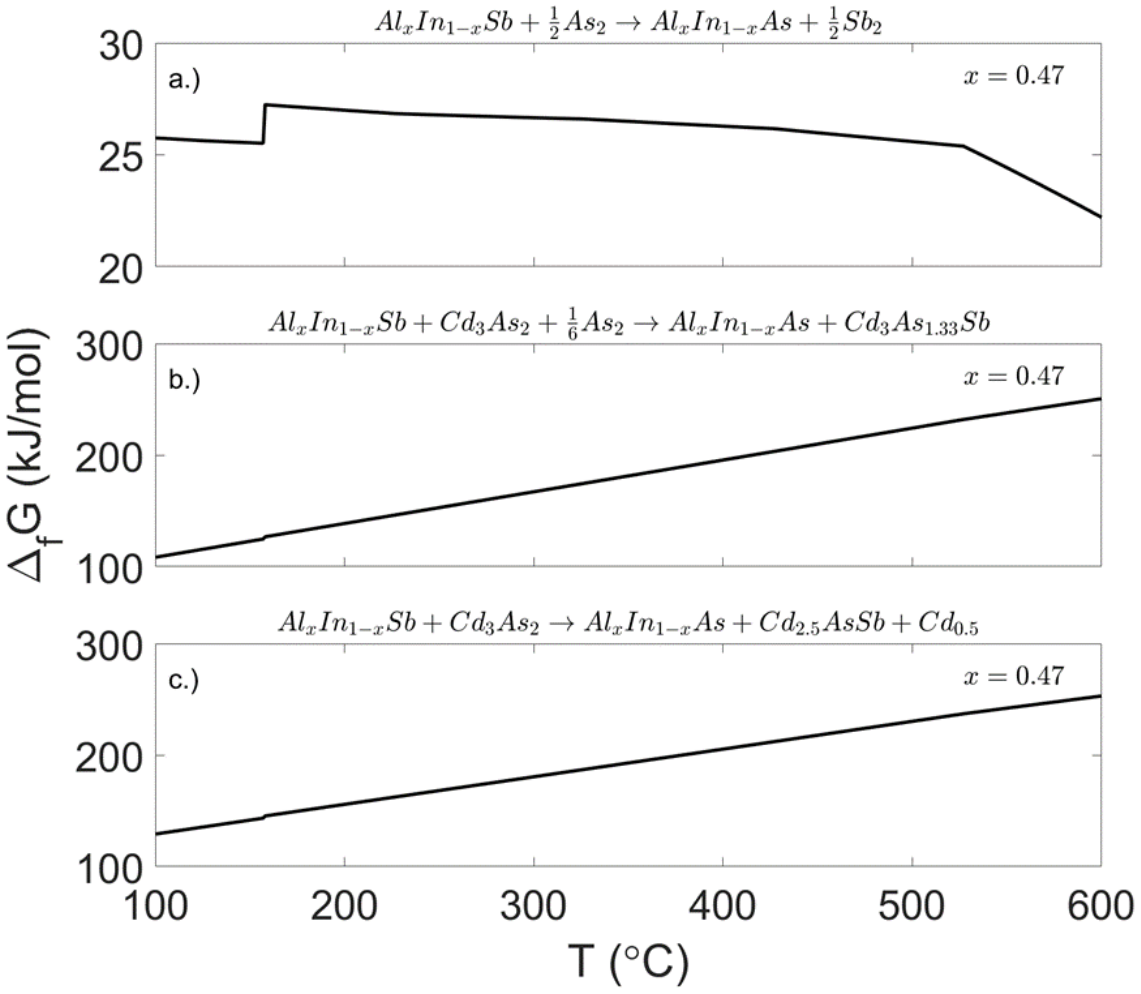

Figure 4.1: The Gibbs free energy of formation ΔG_f for Reactions 4.1-4.3 considering a.) $Al_{0.47}In_{0.53}Sb$ under As_2 overpressure as well as the interaction between a Cd_3As_2 overlayer and a lattice-matched $Al_{0.47}In_{0.53}Sb$ buffer, both b.) in the presence of latent As_2 overpressure and c.) in vacuum.

GaInSb is similarly considered for its reaction with both the Cd_3As_2 layer and any latent As_2 overpressure. Regarding the As_2 overpressure,

$$Ga_xIn_{1-x}Sb + 1/2\,As_2 \rightarrow Ga_xIn_{1-x}As + 1/2\,Sb_2 \tag{4.4}$$

is actually exothermic over a small temperature window, but well into the range of thermal decomposition for the alloy which begins at the InSb melting point of 527 °C. The likelihood of Group-V exchange with and without As are considered through:

$$Ga_xIn_{1-x}Sb + Cd_3As_2 + 1/6\,As_2 \rightarrow Ga_xIn_{1-x}As + Cd_3As_{1.33}Sb, \tag{4.5}$$

and

$$Ga_xIn_{1-x}Sb + Cd_3As_2 \rightarrow Ga_xIn_{1-x}As + Cd_{2.5}AsSb + Cd_{0.5}. \tag{4.6}$$

Since Cd_3As_2 growth is conducted over temperatures from 80-145 °C, it follows that none of these reactions are prohibitive for the use of GaInSb as a lattice-matched buffer for the overlayer.

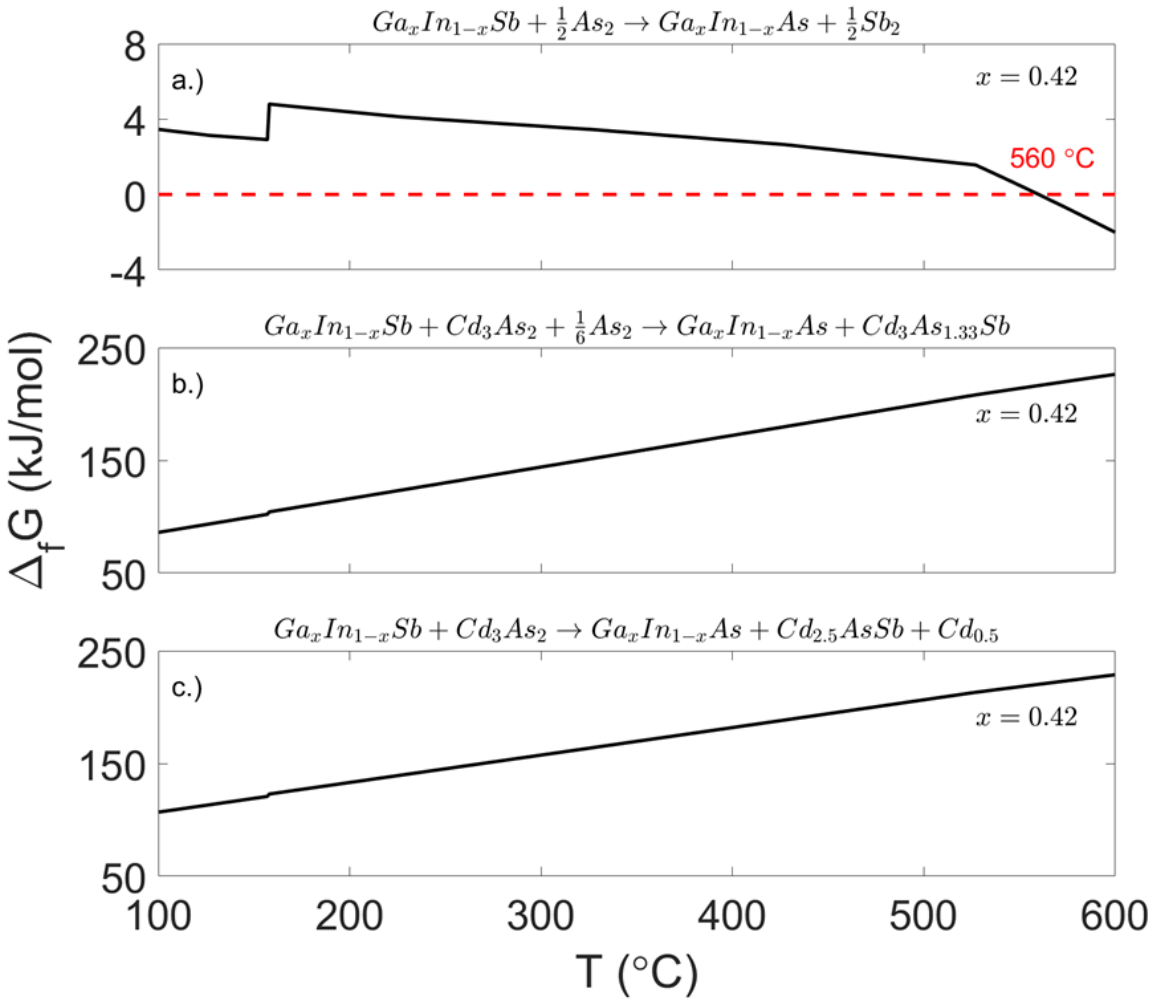

Figure 4.2: The Gibbs free energy of formation ΔG_f for Reactions 4.4-4.6 considering a.) $Ga_{0.42}In_{0.58}Sb$ under As_2 overpressure as well as the interaction between a Cd_3As_2 overlayer and a lattice-matched $Ga_{0.42}In_{0.58}Sb$ buffer, both b.) in the presence of latent As_2 overpressure and c.) in vacuum. The red dashed line in a.) demarcates the transition between an endothermic and an exothermic (spontaneous) reaction between $Ga_{0.42}In_{0.58}Sb$ and As_2 at a temperature of 560 °C.

A contour plot of the Gibbs free energy of formation for reaction 4.4 shows that it will occur spontaneously within a certain temperature window at the lattice-matched ternary conditions.

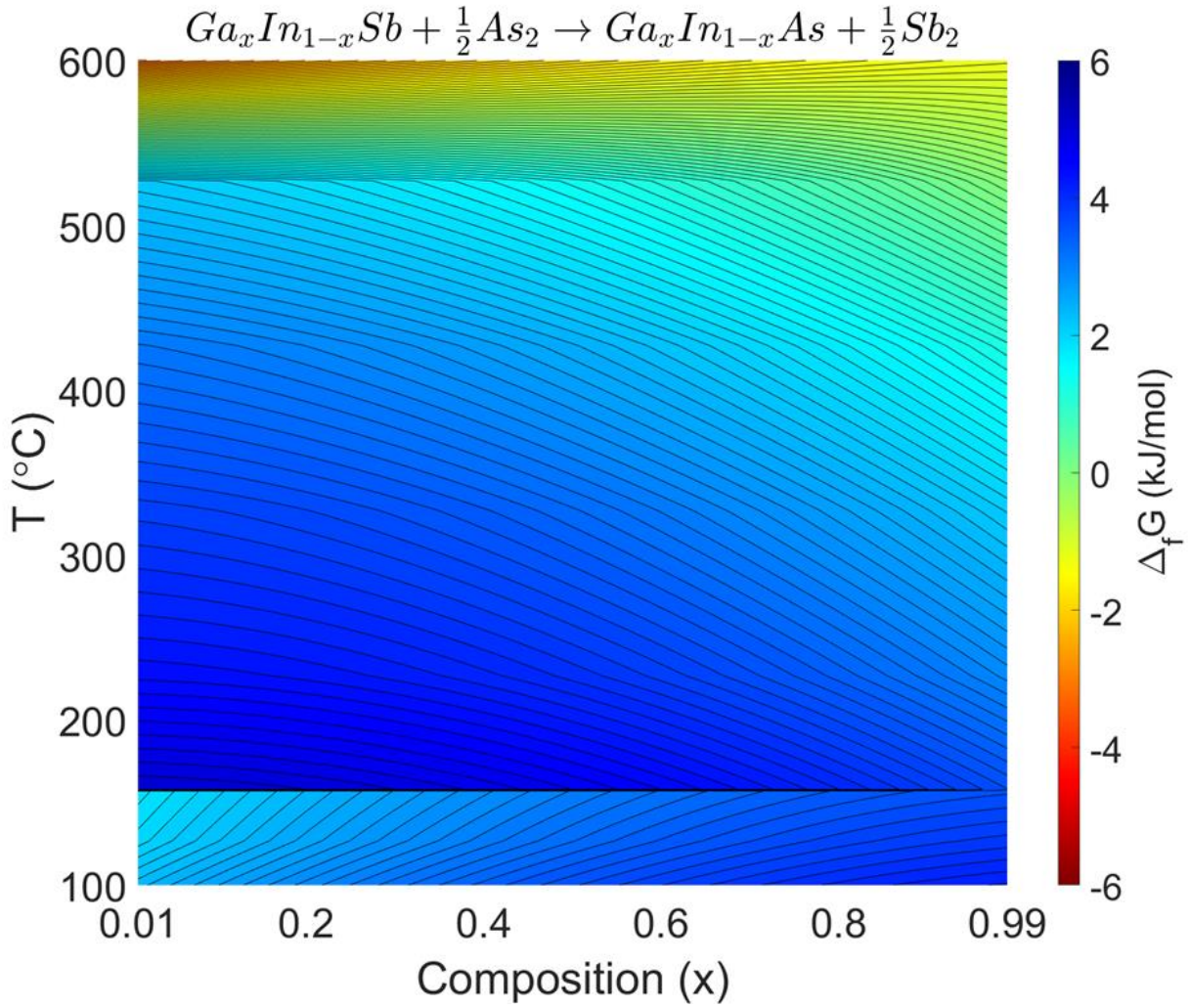

Figure 4.3: The Gibbs free energy of formation ΔG_f for Reaction 4.4 between $Ga_xIn_{1-x}Sb$ and As_2 overpressure as a function of both temperature and ternary alloy composition.

These energy calculations are explored across a larger ternary composition range $0.01 \leq x \leq 0.99$ to determine if off-stoichiometry layers are in danger of allowing Reaction 4.4 to occur over the

experimental Cd_3As_2 growth temperatures. The spontaneity of the reaction is far more dependent on temperature than composition and thusly may be avoided through the same controls devised for the lattice-matched ternary alloys. There are sharp changes in Gibbs free energy at temperatures of 157 °C and 527 °C which correspond to phase changes in the common InSb constituent. Reaction 4.4 between $Ga_xIn_{1-x}Sb$ and As_2 is not expected to occur so long as compositions are kept away from Ga-rich conditions like $x > 0.8$.

InAsSb has the greatest number of potential reactions as it contains both arsenic and antimony. Therefore, it must be also be considered for reactions that produce pure InSb through Group-V exchange. This includes the reaction with latent Sb_2 overpressure both with and without the presence of Cd_3As_2. A reaction where the Cd_3As_2 layer decomposes into CdAsSb and Cd is not considered. The results of this analysis show that:

$$InAs_xSb_{1-x} + \frac{(1-x)}{2}As_2 \rightarrow InAs + \frac{(1-x)}{2}Sb_2, \tag{4.7}$$

and

$$InAs_xSb_{1-x} + \frac{x}{2}Sb_2 \rightarrow InSb + \frac{x}{2}As_2, \tag{4.8}$$

possess a window of spontaneous reaction. For Reaction 4.7 it becomes clear that any As_2 overpressure available during Cd_3As_2 growth at low temperatures will interact with the InAsSb layer, reducing overlayer quality and potentially preventing epitaxy. To achieve quality growth of Cd_3As_2/InAsSb the wait period between InAsSb and Cd_3As_2 growth steps must be extended to allow for sufficient venting of any latent As_2 overpressure from the ternary layer deposition. Likewise, in Reaction 4.8 a pure Sb_2 overpressure will drive the ternary InAsSb towards its binary constituent InSb, which is not lattice-matched with a Cd_3As_2 overlayer. Even if the surface is not

fully converted, the localized reaction presents the danger of producing additional threading dislocations during Cd_3As_2 growth. This reaction is already avoided simply by removing the As_2 and Sb_2 overpressures used for growth at the same time at the transition temperature and growing Cd_3As_2 with stoichiometric fluxes. The full composition contour plot is produced for both reactions.

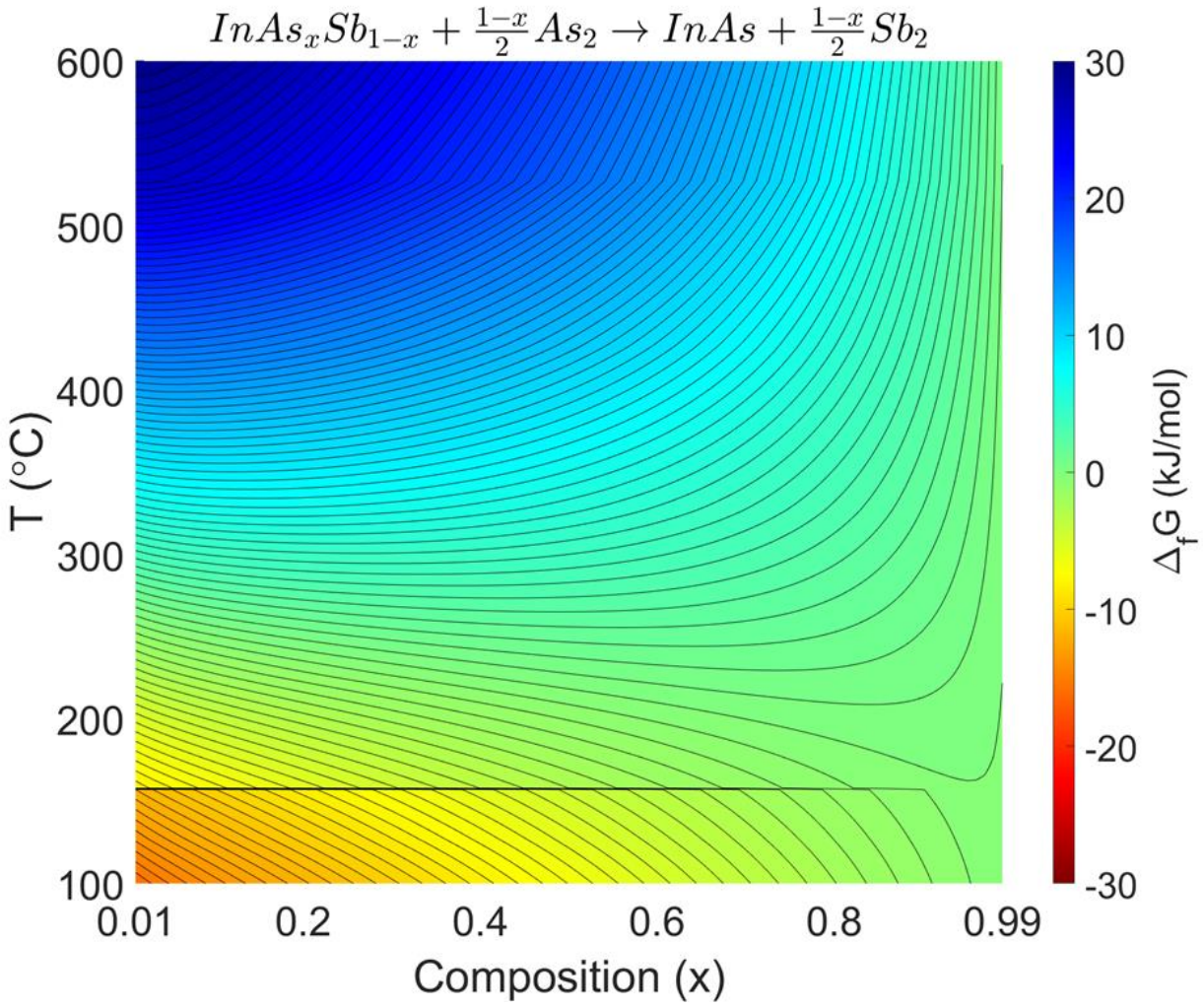

Figure 4.4: The Gibbs free energy of formation ΔG_f for Reaction 4.7 between $InAs_xSb_{1-x}$ and As_2 overpressure as a function of both temperature and ternary alloy composition.

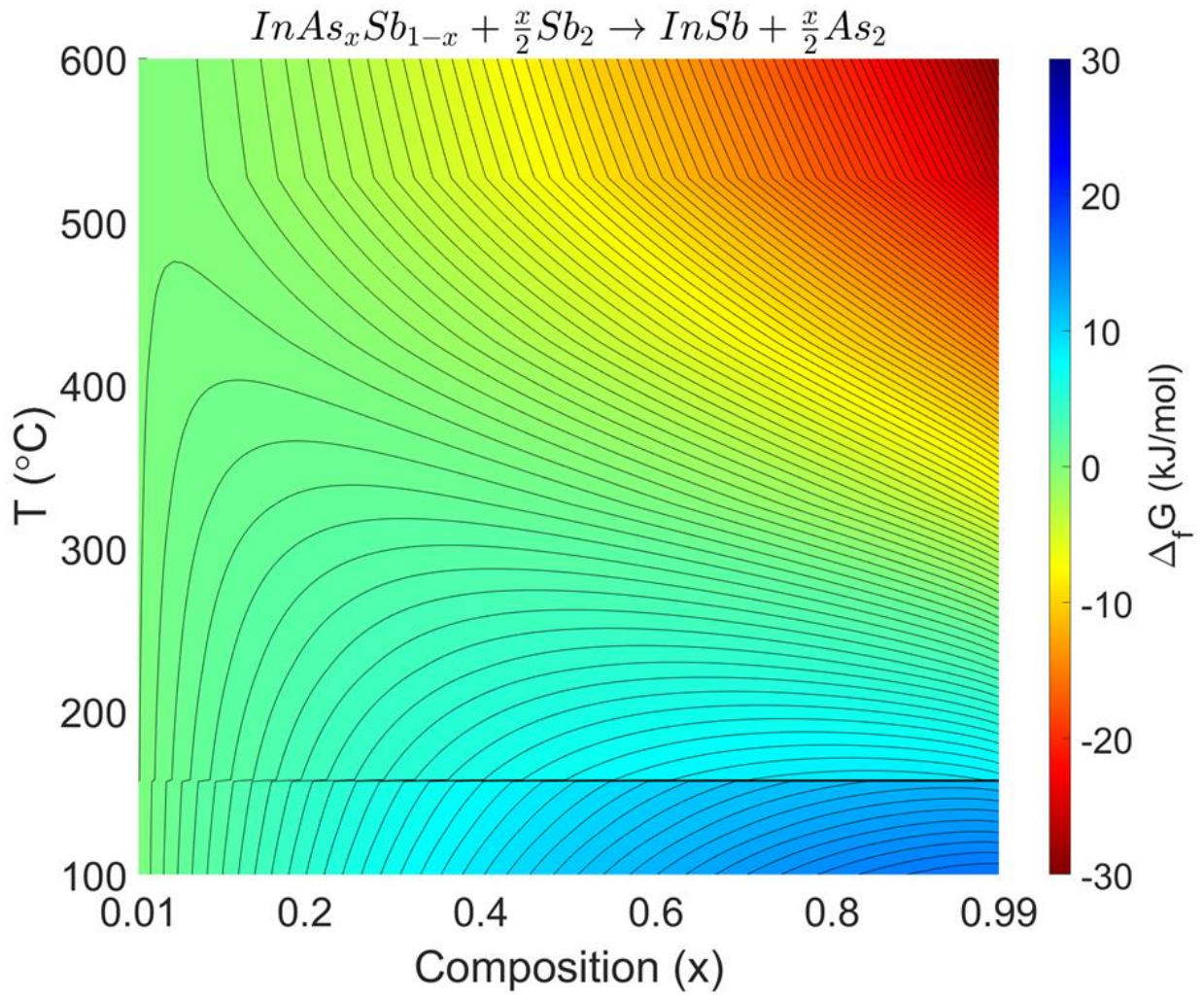

Figure 4.5: The Gibbs free energy of formation ΔG_f for Reaction 4.8 between $InAs_xSb_{1-x}$ and Sb_2 overpressure as a function of both temperature and ternary alloy composition.

The occurrence of Reaction 4.7 between $InAs_xSb_{1-x}$ and pure As_2 overpressure is not a danger so long as the InAs component is kept small. As seen in Figure 4.4, the Gibbs free energy becomes more exothermic for all temperatures above 157 °C as the InAs component becomes greater, changing substantially starting at compositions like $x > 0.6$. Likewise, in Figure 4.5 Reaction 4.8 between $InAs_xSb_{1-x}$ and pure Sb_2 overpressure becomes more exothermic as the InAs component

increases. Fortunately, the standard Gibbs free energy of formation for Reaction 4.8 remains positive over all compositions for temperatures below 200 °C. For InAsSb and Cd_3As_2 together, the proposed reactions are:

$$InAs_xSb_{1-x} + Cd_3As_2 + \frac{(1-x)}{6}As_2 \rightarrow InAs + Cd_3As_{\frac{2(2+x)}{3}}Sb_{1-x}, \quad (4.9)$$

and

$$InAs_xSb_{1-x} + Cd_3As_2 + \frac{(1-x)}{4}Sb_2 \rightarrow InSb + Cd_3As_{1+x}Sb_{\frac{3(1-x)}{2}}. \quad (4.10)$$

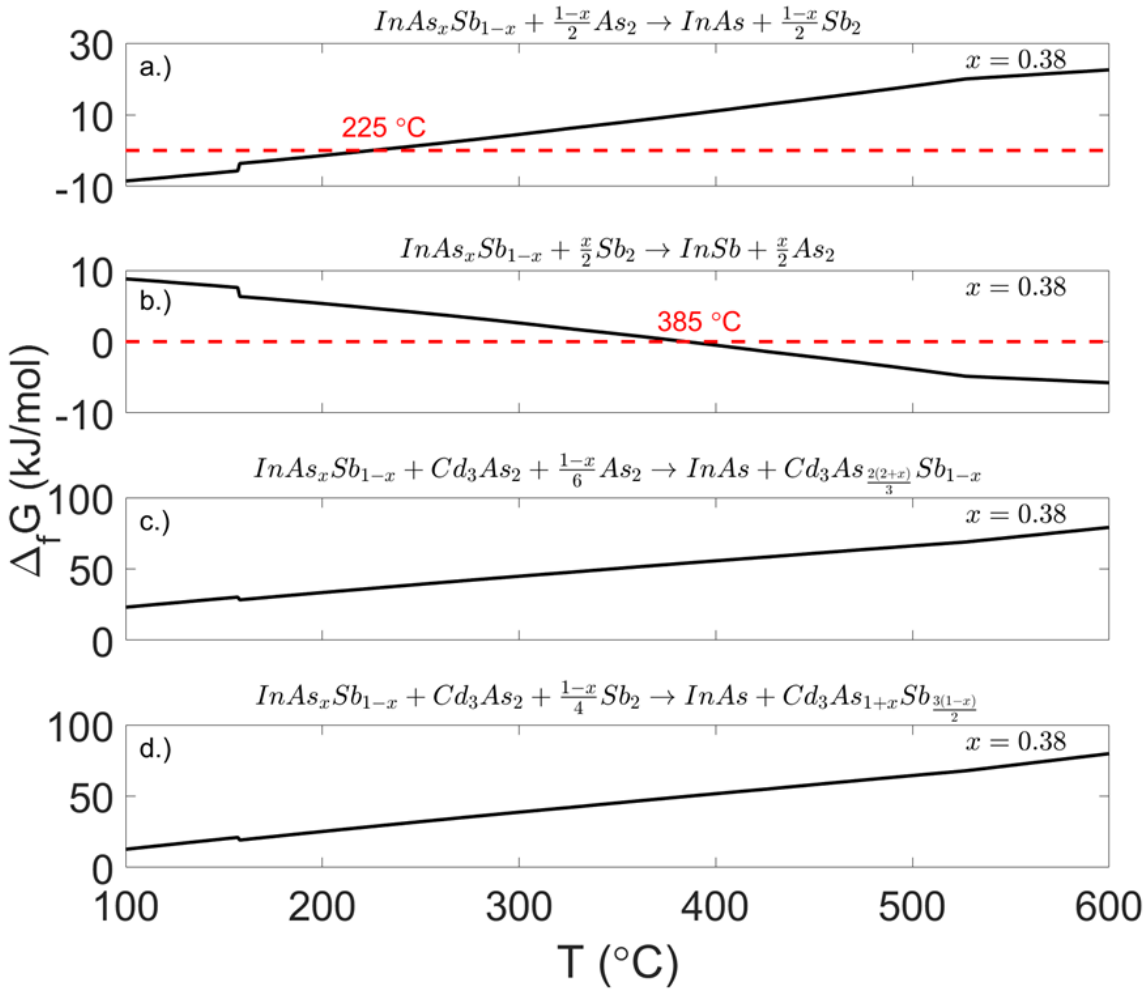

Figure 4.6: The Gibbs free energy of formation ΔG_f for Reactions 4.7-4.10 considering a-b.) $InAs_{0.38}Sb_{0.62}$ under As_2 or Sb_2 overpressure as well as the interaction between a Cd_3As_2 overlayer and a lattice-matched $InAs_{0.38}Sb_{0.62}$ buffer in the presence of latent c.) As_2 and d.) Sb_2 overpressures. The red dashed lines in a-b.) demarcate the transition between endothermic and exothermic reactions.

The red dashed lines in Figure 4.6a-b demarcate the transition between an endothermic reaction and an exothermic reaction between $InAs_{0.38}Sb_{0.62}$ and As_2/Sb_2 at 225 /385 °C.

Gibbs free energy calculations for Reaction 4.11 suggest that Sb_2 overpressure will not interact with the Cd_3As_2 overlayer to form CdSb over the experimental growth temperatures.

$$1/3\,Cd_3As_2 + 1/2\,Sb_2 \rightarrow CdSb + 1/3\,As_2. \tag{4.11}$$

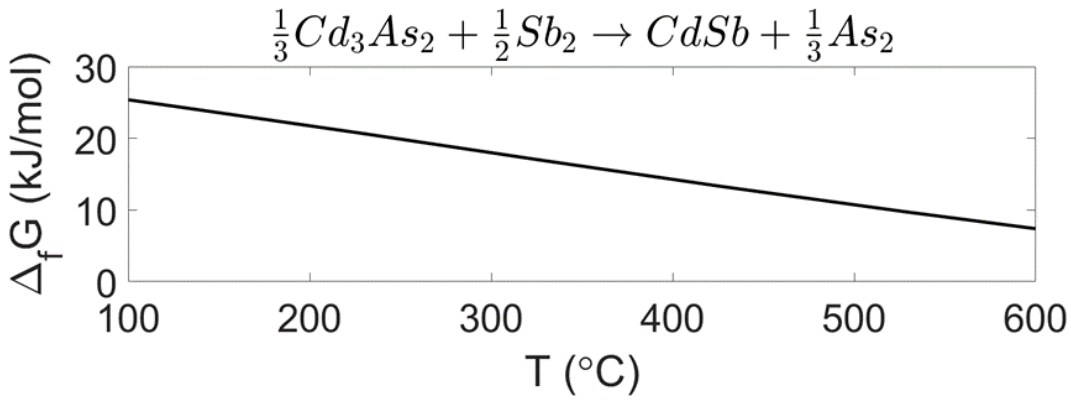

Figure 4.7: The Gibbs free energy of formation ΔG_f for Reaction 4.11 between Cd_3As_2 and any latent Sb_2 overpressure.

4.2 Optimization of Cd_3As_2 growth parameters

Initial MBE growth of Cd_3As_2 began with an open, dual-filament effusion cell before transitioning to the use of a valved, dual-filament cell. In both cases, molecular 99.999% pure (metals basis) Cd_3As_2 source material was used. The open cell setup required low initial effusion cell temperatures due to the high vapor pressure of the Cd component. Indeed, raising the cell temperature to 400 °C and beyond depleted the cell at extreme rates with BEP measurements approaching 10^{-5}-10^{-4} mbar. A sufficient growth rate was achieved using BEP rates on the order of 10^{-6} mbar with tip and base filament temperatures ranging from 300-330 °C. However, fine control of the atomic flux was made difficult considering the significant changes associated with even a 1 °C fluctuation at these low temperatures. The transition to a valved effusion cell therefore provided a twofold benefit. Firstly, the valved control of the cell at fixed temperature setpoints allowed for more reliable fine-tuning of Cd_3As_2 flux. Secondly, higher temperature setpoints with smaller relative temperature fluctuations could be used without depleting the cell of source material. More recent growths follow tip and base filament temperatures of 500 °C and 400 °C respectively, using the valve position to target BEP values in the range of $1\text{-}4\times10^{-7}$ mbar. A Cd_3As_2 valved cell BEP value of 1×10^{-7} mbar corresponds to a growth rate of approximately 0.009 Å/s, or about 30 nm/h. Most films targeted 30-50 nm, although films approaching 100-200 nm were grown to investigate the quality of higher-thickness films. Halved and doubled growth rates were also investigated with no apparent effect on Cd_3As_2 crystal quality.

4.3 Quality of pure cadmium arsenide crystal

4.3.1 Stable growth parameters

Initial Cd_3As_2 growths with the open effusion cell were attempted at substrate temperatures ranging from 110-200 °C. This range is near the upper limits published in literature on the growth of Cd_3As_2 thin films (40,41). The goal here was to grow Cd_3As_2 at the highest possible temperature to allow for a maximal rate of the growth-specific kinetic processes such as adsorption and adatom diffusion, while still retaining a net-positive deposition rate in spite of the high Cd vapor pressure. Because these growth temperatures are so low, the substrate temperature was not mediated by the precision of pyrometry but rather that of the substrate thermocouple. As such, the temperatures investigated here should be viewed more as values belonging to a process variable rather than specific temperature points for useful Cd_3As_2 growth across deposition systems. However, the behavior and magnitude of the temperature range should be consistent. Due to the depletion of the Ga cell at the time of these initial samples, the Cd_3As_2 films were exclusively grown on AlInSb/AlAs/GaAs (001) virtual substrate heterostructures. The results of this initial temperature stability investigation showed that Cd_3As_2 growth would occur at substrate temperatures at least up to 170 °C. This is supported by the presence of the Cd_3As_2 $(00\underline{16})$ peak in the XRD spectra of the 110-170 °C samples. This $(00\underline{16})$ peak may also be present in the 200 °C sample, whose spectrum features the overlap of what appears to be two Gaussian XRD peaks.

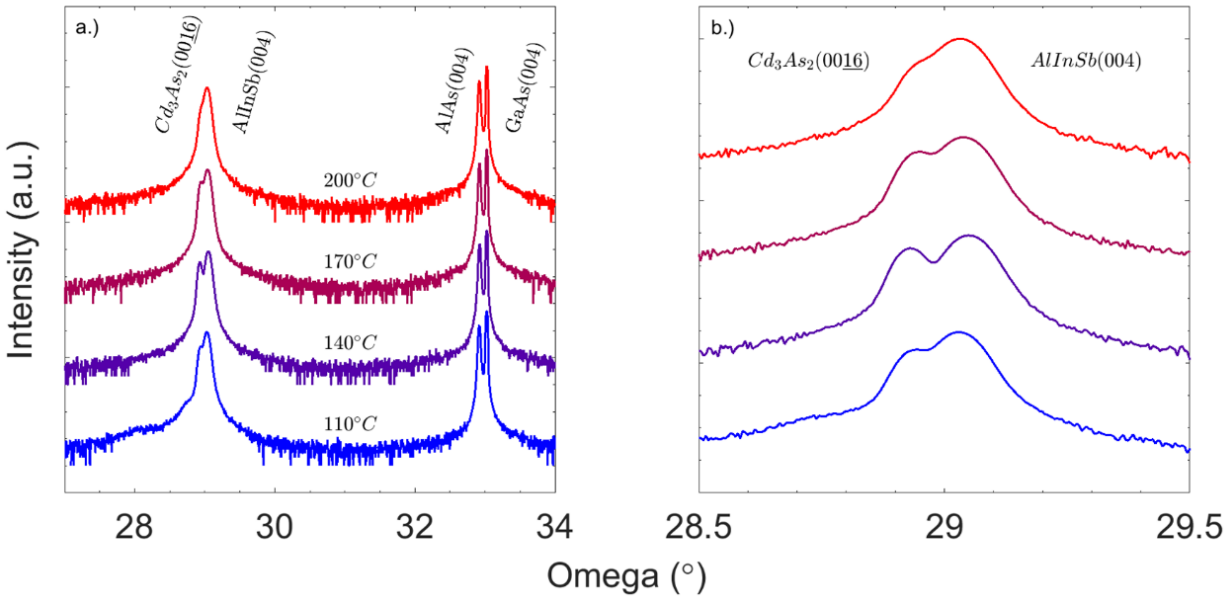

Figure 4.8: X-ray diffraction of Cd_3As_2 deposited using an open effusion cell setup. Four films were grown at substrate temperatures ranging from 110-200 °C. Both a.) the range containing the (004) peaks for the ternary AlInSb, binary buffer AlAs, and substrate GaAs and b.) the narrow region showing the overlap of Cd3As2 $(00\underline{16})$ and AlInSb (004) peaks are shown.

The substrate temperature was found to have a significant effect on the magnitude and FWHM of the Cd_3As_2 $(00\underline{16})$ XRD peak. Its positional differences, which are a function of its out-of-plane lattice parameters, cannot be attributed solely to temperature changes. This is because variance in buffer alloy composition between growths also has an effect on the in-plane strain seen by the Cd_3As_2 lattice, which accordingly modifies the crystal's lattice parameters. For certain ternary compositions the Cd_3As_2 $(00\underline{16})$ and AlInSb (004) peak overlap so that their individual FWHMs cannot be derived for comparison. Still, their relative magnitudes tell important information about the effect of substrate temperature on the net flux of Cd_3As_2 during MBE. The

largest Cd_3As_2 peak magnitude belongs to growth at a substrate of 140 °C, followed by 170 °C, 110 °C, and then if truly Cd_3As_2 $(00\underline{16})$, 200 °C.

Upon the switch to a valved Cd_3As_2 cell, it was discovered that the effective growth range maximum moved from 170-200 °C to 145 °C. This is due to the greater flux control allowed by the adoption of the valved Cd_3As_2 cell. When the open cell was at the active tip/base filament setpoints of 330/300 °C the BEP was approximately 4×10^{-6} mbar after a full cell charge. However, only a BEP on the order of $1\text{-}4\times10^{-7}$ mbar is necessary for reasonable growth rates. With the valved Cd_3As_2 cell these lower BEP values were put into practice for finer control of the Cd_3As_2 film thickness, also having the secondary effect of a lowered growth rate which in turn lowered the temperature point where incoming molecular flux matched the significant desorbing flux due to the high vapor pressure of Cd. The temperature-dependent series was therefore reinvestigated for the valved-cell setup over temperatures ranging from 60-160 °C so that a new maximum growth temperature threshold could be determined. Seven films were grown without reaching a low limit where crystalline Cd_3As_2 did not form.

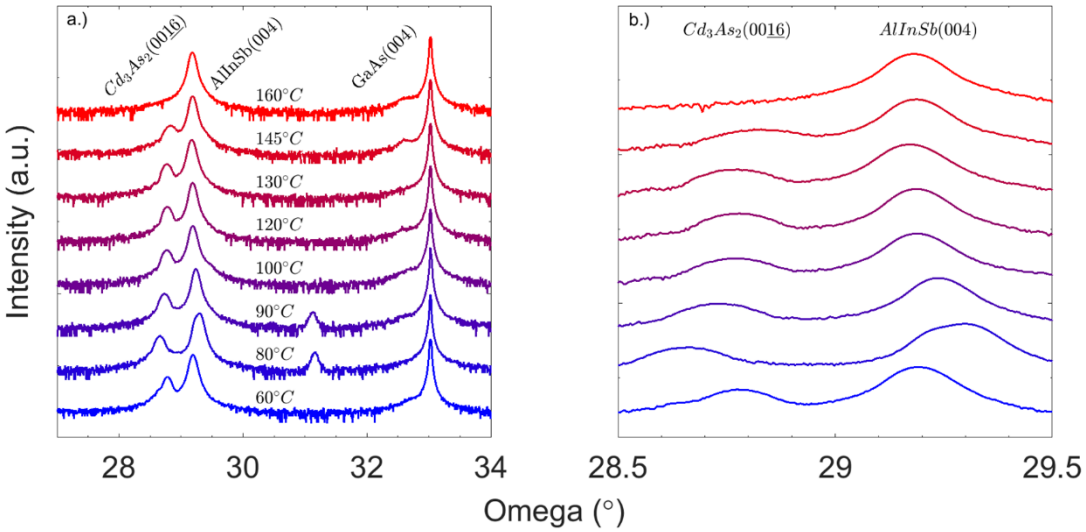

Figure 4.9: X-ray diffraction of Cd_3As_2 deposited using a valved effusion cell. Both a.) the range containing the (004) peaks for the ternary AlInSb and substrate GaAs and b.) the narrow region showing distinct Cd_3As_2 $(00\underline{16})$ and AlInSb (004) peaks are shown.

Here, heating to a substrate temperature of 160 °C produces a net-negative molecular flux because the decomposition rate is greater than the incorporation rate, resulting in no Cd_3As_2 deposition. This effect is confirmed by the absence of the Cd_3As_2 $(00\underline{16})$ peak despite the clear presence of the high-quality AlInSb (004) virtual substrate peak. Shifts in the Cd_3As_2 $(00\underline{16})$ peaks are more apparent in Figure 4.9b, and are due to variation in the ternary layer composition and therefore the Cd_3As_2 film strain state. An interesting artifact in the spectra here is the presence of a small, but real peak at $\theta = 31.1$ for the 80 and 90 °C samples. It has been identified as elemental Cd $(2\bar{1}0)$ via an XRayUtilities simulation of the polycrystalline element. Similar peaks at $\theta = 31.1°$ have occasionally appeared at lower temperatures in the growth range.

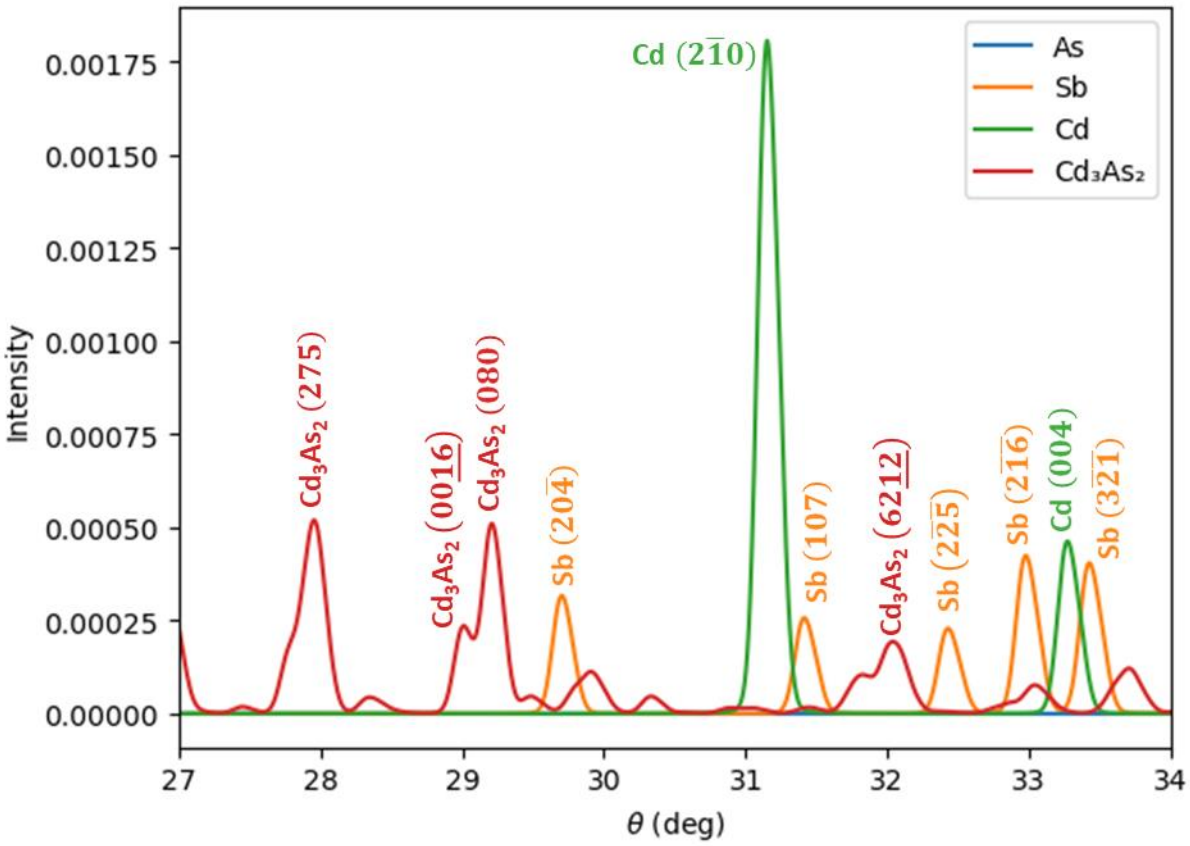

Figure 4.10: Simulated X-ray diffraction peaks of polycrystalline Cd, As, Sb, and CdAs in the region of interest for the Cd_3As_2 $(00\underline{16})$, ternary alloy (004), and GaAs (004) peaks. Peaks with over 4.00 % relative intensity with respect to their element/compound are labeled.

The role of As_2 overpressure in the MBE of Cd_3As_2 was investigated during the period of open effusion cell operation. The purpose of this growth series was to determine if the use of a Cd_3As_2 molecular flux alone would be sufficient to produce high quality Cd_3As_2 films, or if As_2 overpressure supplementation would facilitate more desirable growth. The behavior of overpressure here is much different than at the high temperatures used to grow the ternary alloy virtual substrates, as the Cd_3As_2 growth temperature range is well within the adsorptive range for

As_2 molecular flux. As such, even small changes in overpressure values will have a significant effect on thin film growth as there is no desorption of excess deposited As. Four samples were grown at a substrate temperature of 140 °C following the application of As_2 BEP values ranging from 2.5×10^{-7}-1.5×10^{-6} mbar. An additional sample with no As_2 overpressure was grown during the same time period to act as a control.

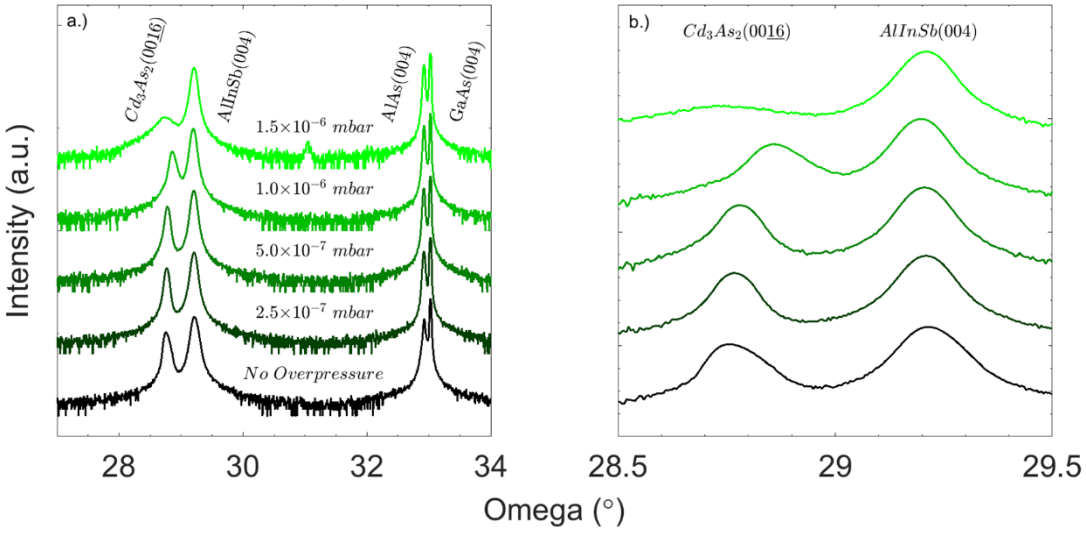

Figure 4.11: X-ray diffraction of Cd_3As_2 deposited at 140 °C using an open effusion cell setup with varying As_2 overpressure during growth. These five films represent beam-equivalent values ranging from zero to 1.5×10^{-6} mbar. Both a.) the range containing the (004) peaks for the ternary AlInSb, binary buffer AlAs, and substrate GaAs and b.) the narrow region showing distinct Cd_3As_2 $(00\underline{16})$ and AlInSb (004) peaks are shown.

Additional As_2 overpressure begins to degrade crystal quality starting at BEP values of 1.0×10^{-6} mbar. The degradation of the Cd_3As_2 $(00\underline{16})$ peak is substantially greater for an even higher BEP of 1.5×10^{-6} mbar. In order of increasing As_2 overpressure the FWHMs of these Cd_3As_2 $(00\underline{16})$

peaks are 293, 226, 226, 283, and 616 arcsec. The ideal Cd_3As_2 $(00\underline{16})$ 2θ value according to the literature c lattice parameter of 25.428 Å is 28.993°, which these spectra deviate from at a maximum of 28.755° corresponding to c = 25.619 Å. The film grown under the second-highest As_2 overpressure is the closest to the literature value at 28.861° corresponding to c = 25.533 Å. According to this result, a minor As_2 overpressure may have some positive effect on the final Cd_3As_2 quality, but more experiments should be done to see if this effect appears consistently across the stable Cd_3As_2 growth temperature range. Clearer, however, is the significant quality-reducing effect of As_2 overpressure at BEPs approaching 1.5×10^{-6} mbar.

4.3.2 Engineered-strain Cd_3As_2 series

The experimental heterostructure was grown using $Al_xIn_{1-x}Sb$/GaAs buffers targeting lattice-mismatched ternary compositions to induce biaxial strain in the pseudomorphically-grown Cd_3As_2 overlayers. Nominally 30 nm Cd_3As_2 films were grown to investigate the electronic behavior of basal-plane Cd_3As_2 with a thickness below 60 nm for surface state-dominated 2D electron transport. XRD shows four samples where the strain in the Cd_3As_2 layer ranges from essentially lattice matched at ε = -0.005 %, to significant tension where ε = +0.136 %. Plots covering both the θ = 27-34° region of interest and a θ = 5-55° long range scan present extraneous peaks not associated with the target heterostructure layers. One matches the simulation of Cd $(2\bar{1}0)$ and two match closely with monteponite (CdO) (93). Those marked with a single asterisk match at least one of the peaks belonging to the common As and Sb oxides arsenolite (As_2O_3), claudetite (As_2O_3), valentinite (Sb_2O_3), and senarmontite (Sb_2O_3) (94–96). More experimentation is required to definitively mark these compounds as present. The peak marked with a double asterisk is beyond the normal reported omega range for most XRD data.

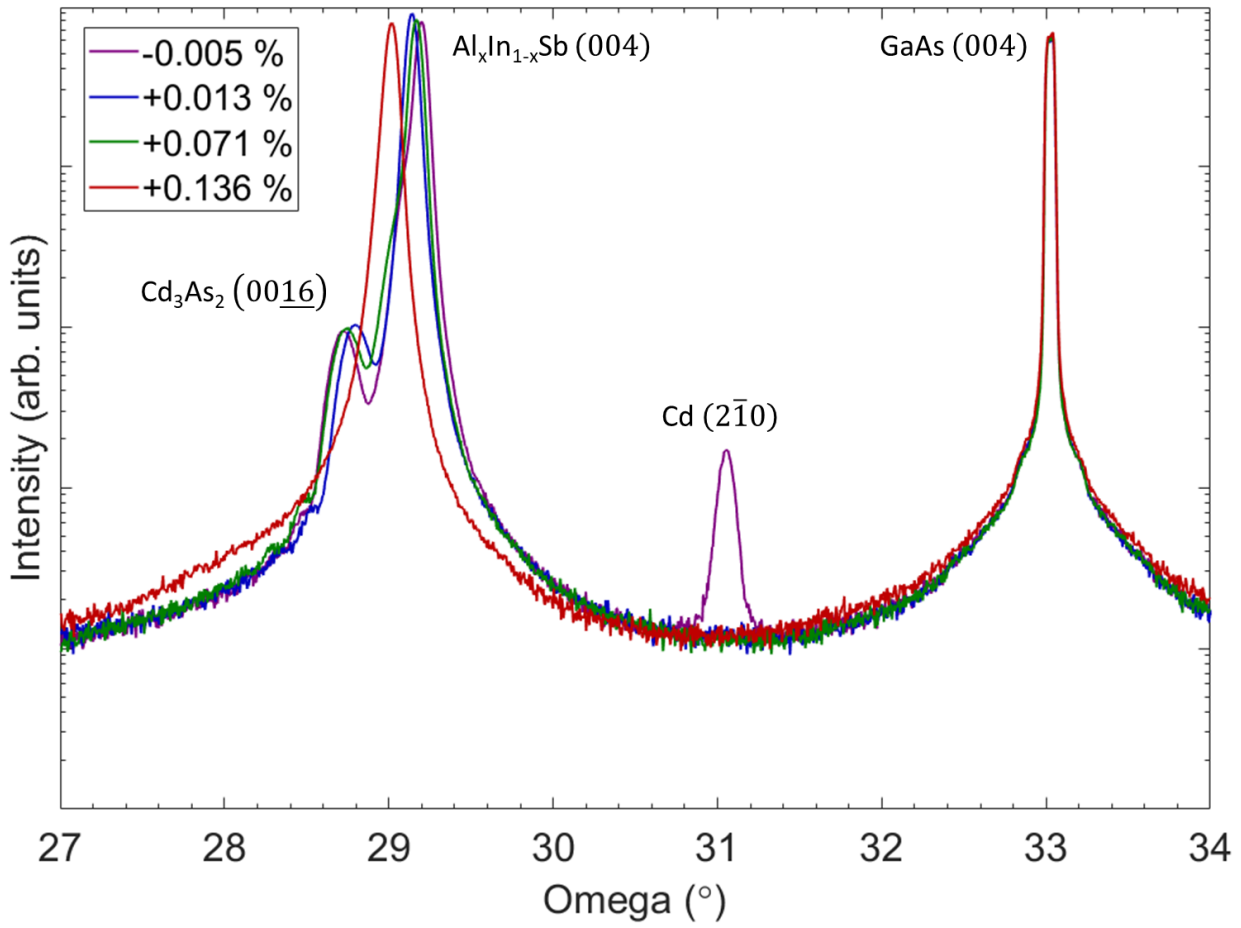

Figure 4.12: Short range X-ray diffraction of Cd_3As_2 grown on $Al_xIn_{1-x}Sb$ with varying composition x. The biaxial in-plane strains ε within the Cd_3As_2 films are listed in the legend.

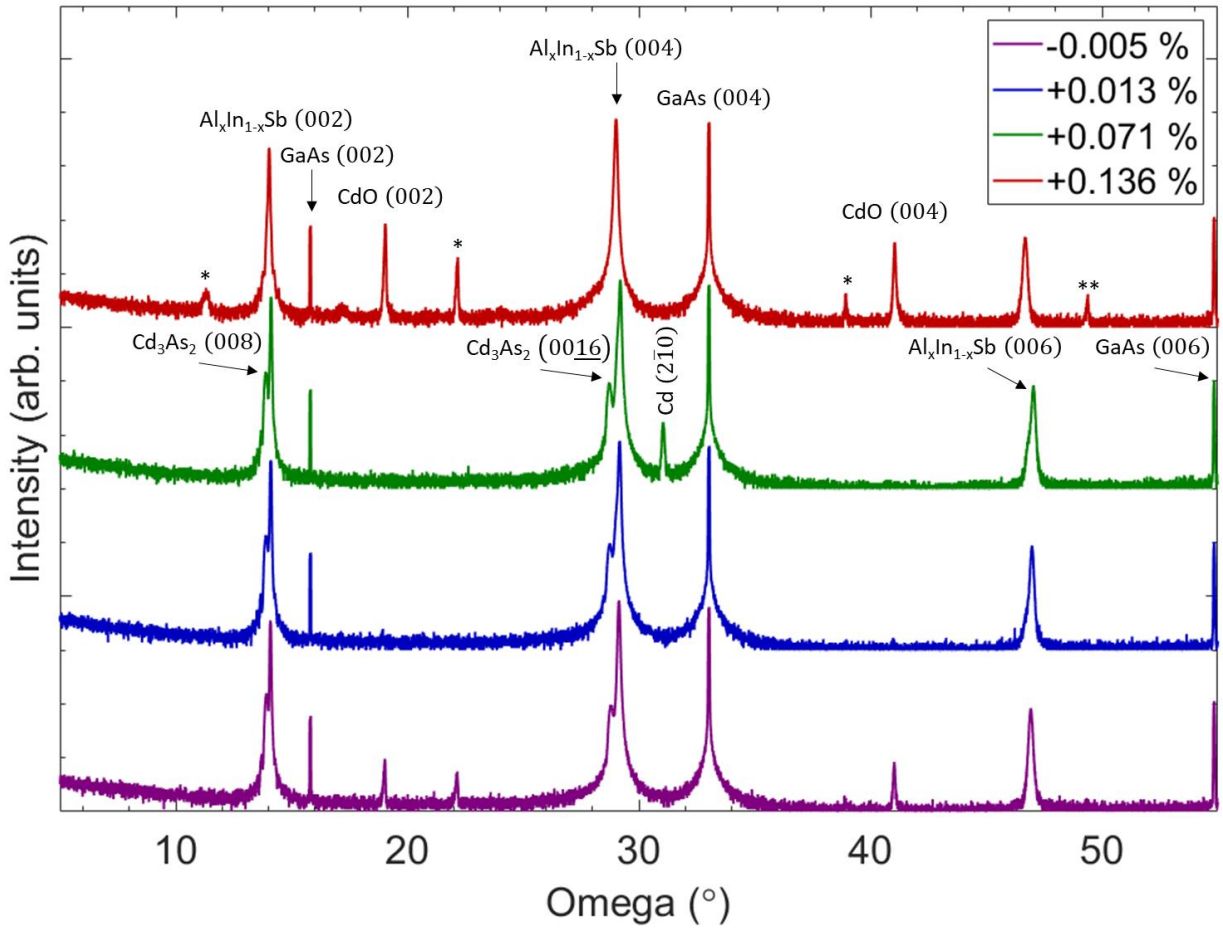

Figure 4.13: Long range X-ray diffraction of Cd_3As_2 grown on $Al_xIn_{1-x}Sb$ with varying composition x. The biaxial in-plane strains ε within the Cd_3As_2 films are listed in the legend.

Regarding thickness measurements using XRR, simulations for these strained samples like in Figure 4.14 show that they have top films with thicknesses between 28 and 33 nm.

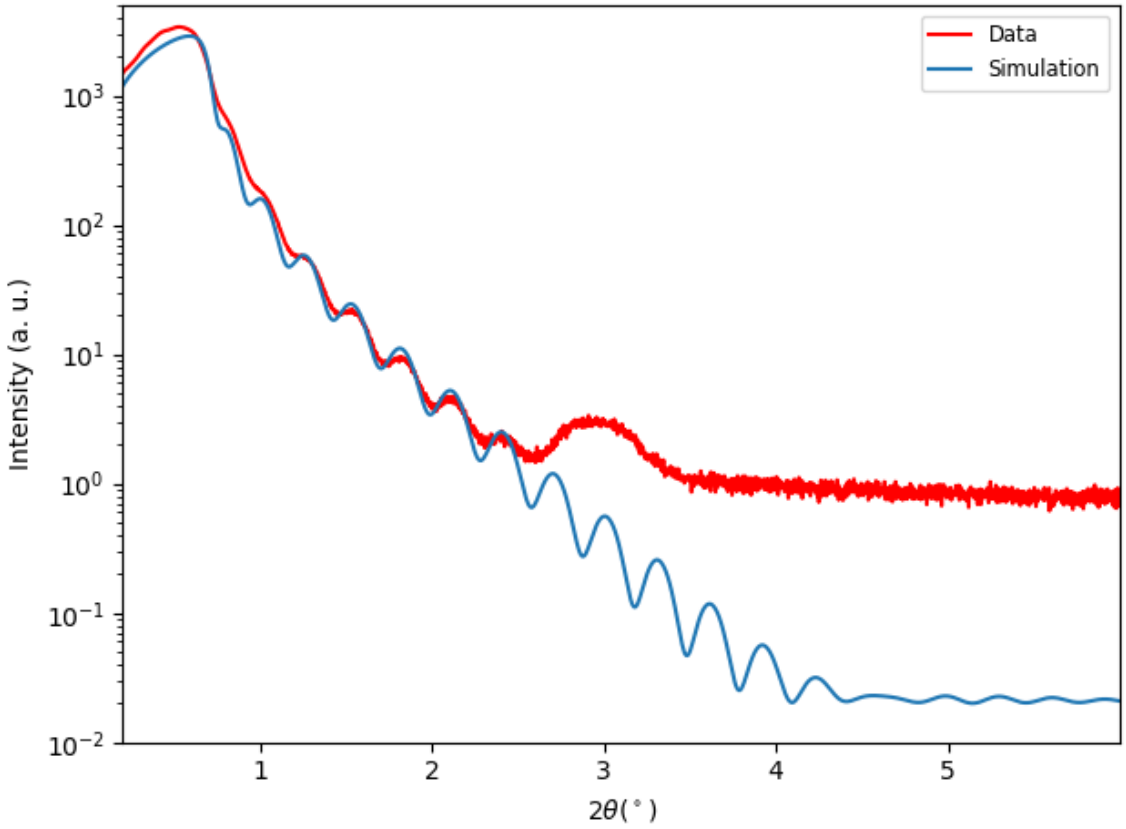

Figure 4.14: Representative X-ray reflectivity measurement for the ε = +0.136 % CdAs film comparing raw data to the simulated reflectivity pattern. The oscillation periodicity corresponds to a film thickness of approximately 33 nm.

Despite the presence of an overlayer according to XRR, the highest-strain sample does not exhibit a Cd_3As_2 $(00\underline{16})$ peak. The calculated strain value for this sample therefore applies to a basal plane-oriented $I4_1/acd$ Cd_3As_2 layer grown on the virtual substrate, but not necessarily the overlayer in this sample. The high tensile strain may be beyond the stable lattice-mismatch limit for pseudomorphic growth of basal-plane Cd_3As_2 growth.

4.4 Low-temperature Hall measurements

Van der Pauw measurements were conducted at 2 K on four cadmium arsenide films deposited with varying levels of engineered strain. The films close to the lattice-matched condition exhibit Shubnikov-de Haas oscillations ($\upsilon = 1$) corresponding to the QHE.

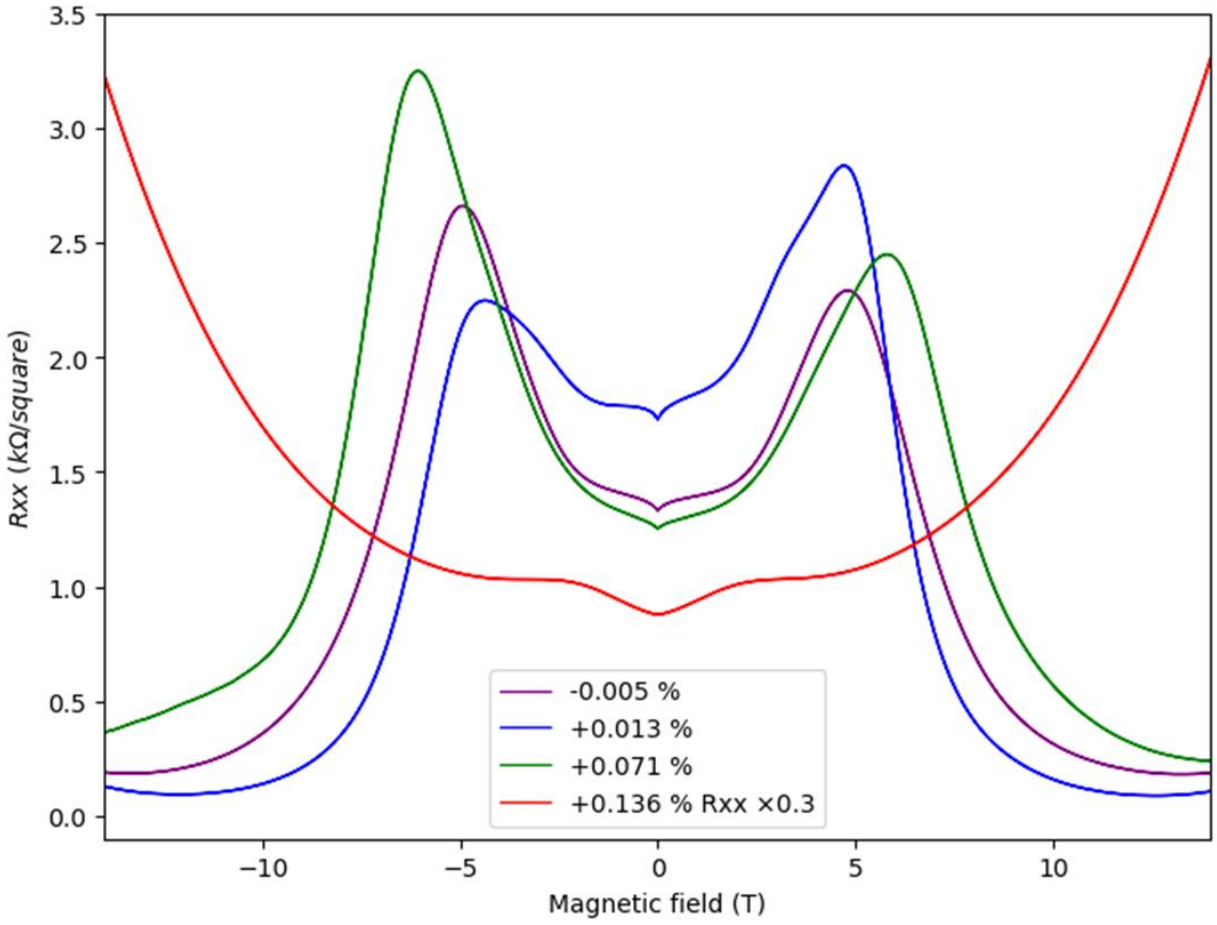

Figure 4.15: Longitudinal R_{xx} signal from Van der Pauw measurements of cadmium arsenide films with biaxial strains ranging from nearly lattice-matched to significant tension. The highest-tension data has been scaled by 0.3 for easier comparison with the other spectra.

The highest-strain sample, which does not exhibit the Cd_3As_2 $(00\underline{16})$ XRD peak, also does not produce any Shubnikov-de Haas oscillations. In addition, its maximum R_{xx} value is of a much higher magnitude than the other three films over the measured fields. The cusp in the center of these plots is the result of weak antilocalization due to high SOC in the TS Cd_3As_2 (97). This effect occurs due to quantum interference arising from spin-momentum locking in a high-SOC system, where backscattered partial electron waves destructively interfere with the forward electron movement at low magnetic fields (98).

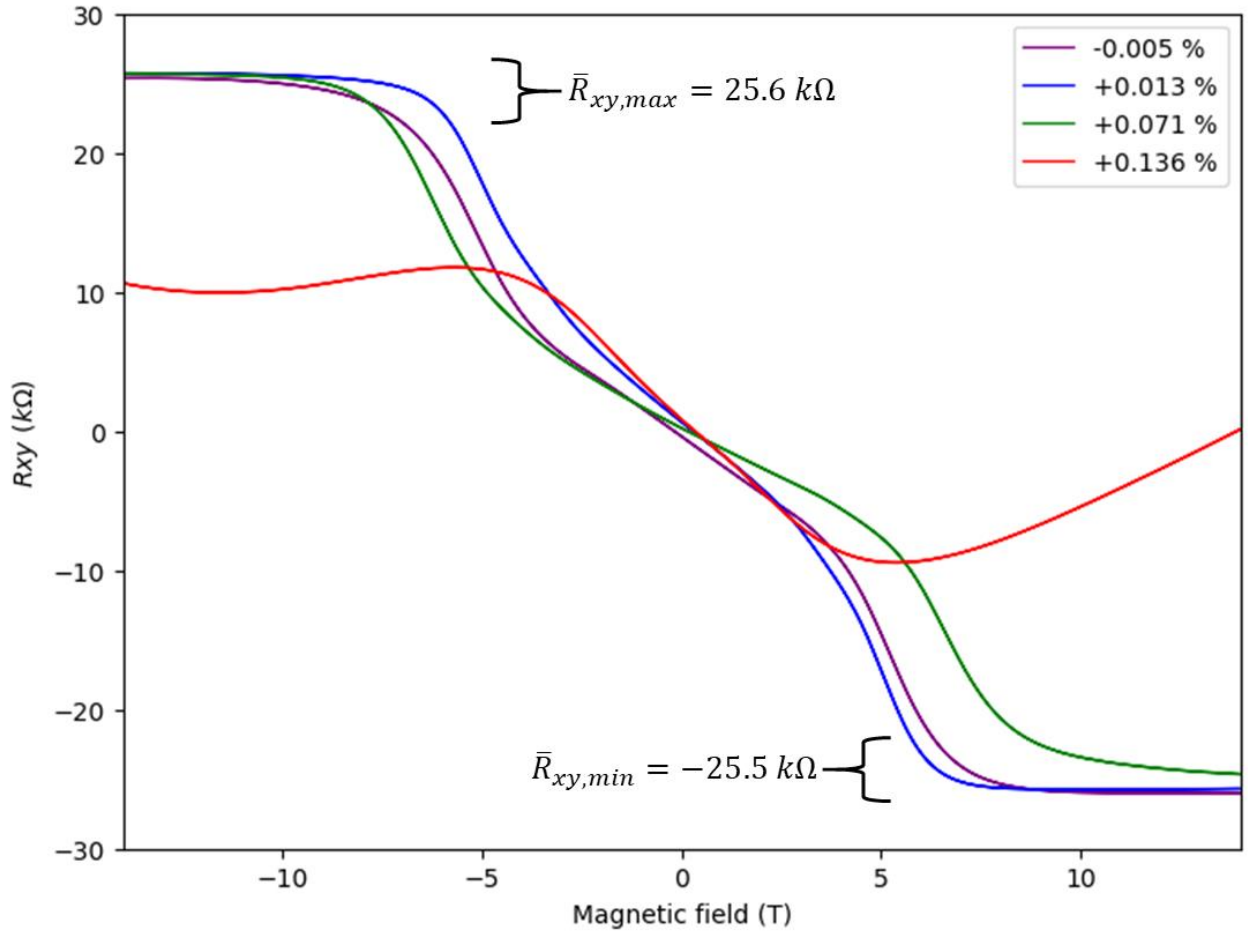

Figure 4.16: Transverse, Hall effect R_{xy} signal from Van der Pauw measurements of cadmium arsenide films under biaxial strains ranging from nearly lattice-matched to significant tension.

Three of the four films exhibit QHE resistivity plateaus according to the Landau filling factors υ = ±1. Because there is some variation in the plateau resistivity, their average maximum/minimum resistivities correspond to υ = 0.992/0.988. The QHE resistivity plateaus must be quantized according to either an integer or specific fractional multiple of h/e^2, so this deviation reflects non-ideal sample processing and measurement error. This measurement error also appears in the fact that R_{xy} is nonzero at the zero-field condition (instead being almost zero), which is clearly not in line with the expected physical behavior of the Hall effect. There is a possibility that the low mobility of the high-strain film is shifting any QHE plateaus beyond the experimental field range. However, the high-strain spectrum does not exhibit antisymmetric behavior centered on the zero-field resistivity which is expected from the QHE in a topological system. The presence of a local maximum and minimum in the R_{xy} signal and its deviation in curvature from the other spectra may be due to multi-carrier effects (68). Despite these differences, the near-linear portion of the spectrum $\left|\overrightarrow{B_Z}\right| \leq 2$ T is still sufficient for determining the mobility and density of the majority carrier. All linear fits possess a least-squares fit value $R^2 \geq 0.9997$.

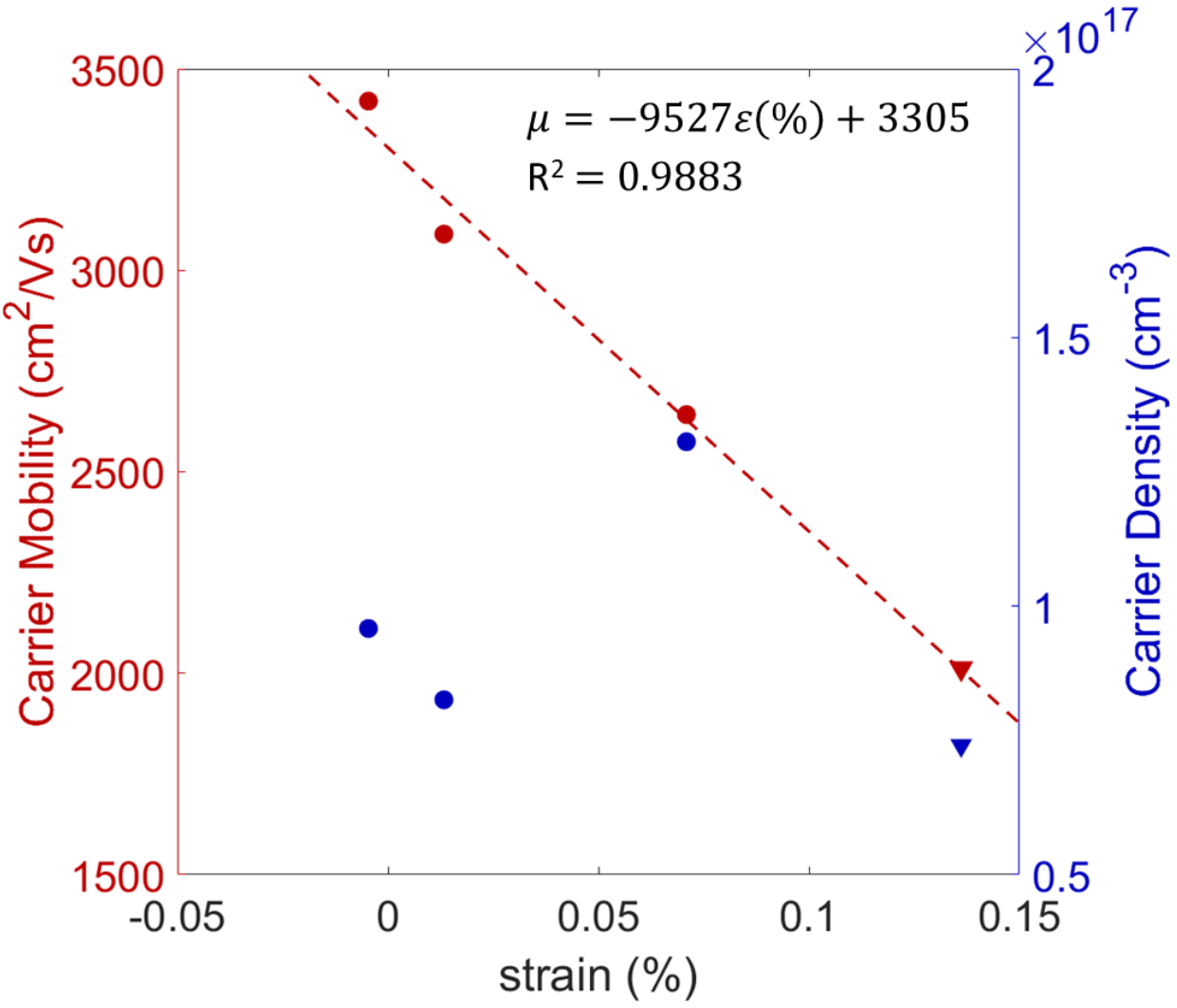

Figure 4.17: Carrier mobility and bulk carrier density as function of cadmium arsenide strain.

Carrier mobility and bulk carrier density change as a function of biaxial strain in these cadmium arsenide films. The mobility is maximized for the film closest to the lattice-matched condition and is minimized for the film in the highest amount of biaxial tension. A linear fit of the carrier mobility matches the data relatively well with R^2 = 0.9883. More experimental points, particularly for $\varepsilon \leq 0$, are required to see where the optimum in carrier mobility lies.

Chapter 5: Considerations for Magnetic Alloying of Cadmium Arsenide

5.1 Miedema model for metallic alloys

The magnetic alloying of Cd_3As_2 would be a significant step towards producing MTMs, TMETS, and other proposed devices requiring magnetic topological material. The influence of an internal magnetic field will break *T* symmetry so that the QAHE may be observed. However, the achievement of a magnetic, topological Cd_3As_2 alloy necessitates additional considerations beyond those of pure Cd_3As_2. They are that a potential alloying element must be magnetic and that it must be capable of substituting into the pure crystal without breaking certain symmetries.

The magnetic nature of potential alloying elements is a quality associated with the presence of unpaired electron spins in the outermost electron shell. Because of this, the Fourth-Row Transition Metals (FRTMs) and their compounds with unpaired 3d-shall electrons are common ferromagnets, antiferromagnets, and ferrimagnets. Likewise, the Rare Earth (RE) elements with unpaired 4f-shell electrons are frequent candidates for magnetic compounds. These FRTMs and RE elements are therefore considered for their incorporation into the Cd_3As_2 crystal. Not considered, however, are the FRTMs with full 3d shells (Cu, Zn) and REs with full 4f shells (Yt, Lu). In addition, the radioactive Pm is not a viable candidate for magnetic alloying at this time because of safety concerns.

Regarding substitution within the Cd_3As_2 crystal for magnetic alloying, twenty ions comprised of seven FRTMs and twelve REs are considered in Table 5.1.

Table 5.1: Effective ionic radii of Cd_3As_2 crystal ions and potential magnetic alloying elements considered for incorporation (99). Coordination Numbers (CNs) are listed next to their relevant ions. †Ionic radii corresponding to high-spin configurations are marked.

Ion (CN)	Ti^{2+} (6)	V^{2+} (6)	Cr^{2+} (6)	Mn^{2+} (4)	Fe^{2+} (4)	Co^{2+} (4)	Ni^{2+} (4)
Eff. Ion. Rad. (pm)	86	79	80†	66†	63†	58†	55
Ion (CN)	Ce^{3+} (6)	Pr^{3+} (6)	Nd^{3+} (6)	Sm^{3+} (6)	Eu^{2+} (6)	Eu^{3+} (6)	Gd^{3+} (6)
Eff. Ion. Rad. (pm)	101	99	98	96	117	95	94
Ion (CN)	Tb^{3+} (6)	Dy^{3+} (6)	Ho^{3+} (6)	Er^{3+} (6)	Tm^{3+} (6)	Cd^{2+} (4)	As^{3-}
Eff. Ion. Rad. (pm)	92	91	90	89	88	78	—

A substituted ion must not be significantly larger or smaller than the ion/ordered vacancy it replaces or else it will modify the TS host structure. Specifically, the Coordination Number (CN) of the atoms in a structure is modified by their relative sizes. This also means that the magnetic alloying element can only be incorporated in small atomic percentages in order to preserve the host structure. The ionic radii of the relevant atoms are taken from the work by *Shannon* (99). For ions where multiple configurations are available, the radius for a CN of four is preferentially chosen since the tetrahedrally coordinated Cd^{2+} would be the substituted ion site to maintain charge neutrality. The exception to this preference is As^{3-}, which is part of the host structure and has a coordination number of six. The term "high-spin configuration" refers to an ionic state with more unpaired electrons in the valence orbitals where available, and "low-spin configuration" refers to a state with fewer. For ions where the high- and low-spin configurations are available, the high spin radius is listed because it is more desirable for magnetic behavior.

The ionic radii of the 2+ oxidation state FRTMs vary significantly in part due to the availability of both low-spin and high-spin 3d electron configurations. The RE ions are generally larger than Cd^{2+} with exception of Eu^{2+} (117 pm), in part because the common oxidation state of

most considered RE elements is 3+. For both the FRTMs and the REs, the deviation in ionic radius from the common Cd^{2+} site is not so severe that their potential incorporation is impossible. According to Pauling's rules for the coordination number of ionic compounds, the CN of the alloying element substituting on a Cd^{2+} site is dependent on a minimal ionic ratio between the FRTM/RE substitute and the As^{3-} ions in the FCC sublattice (100). Data is not available of the effective radius of the As^{3-} ion, i.e. As (-III), but clues can be taken from the stable $I4_1/acd$ Cd_3As_2 structure in which the Cd^{2+} ion is tetrahedrally coordinated with the As^{3-} sublattice. Following Pauling's rules, the minimum ratio for tetrahedral coordination to remain geometrically stable is $\left(\sqrt{3}/\sqrt{2}\right) - 1 = 0.22474$ with a preference for octahedral coordination appearing at $\sqrt{2} - 1 = 0.41421$. Because a coordination number of four corresponds to the replacement of a Cd^{2+} ion, the substitutional atom should have a radius corresponding to a ratio within these two bounds. Following the geometric limits imposed through Pauling's rules, the radius of As (-III) should then be somewhere in the range of 229-423 pm for the Cd_3As_2 crystal to remain stable, although this is a rudimentary estimate. The importance of these considerations, however, is that substituted 3+ REs should be at least tetrahedrally coordinated as they are all larger the Cd^{2+} ionic radius. Depending on the As (-III) ionic radii estimate according to Pauling's rules, the transition from tetrahedral to octahedral coordination should occur for a substitutional ion radius of 95 to 175 pm.

The application of FRTMs as magnetic dopants in non-magnetic semiconductors to create dilute magnetic semiconductors is well-documented (101,102). The electronic and magnetic properties of these compounds are mediated by p-d orbital interaction originating from the introduction of the FRTM 3d orbital. The FRTMs have the doubled benefit of providing carriers for extrinsic semiconductor behavior and hosting localized electronic spins for potential spintronic devices. Studied dilute magnetic semiconductors include the III-V and II-VI systems GaAs and

CdTe, where cation substitution with Mn produces magnetic character. (Ga,Mn)As was produced via low-temperature MBE to limit MnAs phase formation, and reached a maximum Curie temperature of 110 K (102). This is above the low temperatures used in Van der Pauw measurements here, but it is also unfortunately well below room temperature where QAHE devices would be most practical. A significant concern in alloying FRTMs with Cd_3As_2 is the stability of the host crystal. The issue here is that the use of a low solubility magnetic element may lead to the nucleation of additional undesired phases. This is a common occurrence with FRTMs in dilute magnetic semiconductors, such as in the creation of a distinct ferromagnetic MnAs phase. Expounding on this, the low-temperature MBE of $Ga_{1-x}Mn_xAs$ has a composition limit of approximately x = 7.1 % before the appearance of a separate MnAs phase. Likewise, Mn and Cr have already been alloyed with Cd_3As_2 in the literature, and they also exhibit very small limits of solubility at 5 % and 2 % (103,104). If it is the case that a magnetic element alloying percentage beyond the single digits is required for the QAHE, the FRTMs may not be sufficient due to their low solubility limits in Cd_3As_2. The limit of useful alloying content is decreased further when considering how alloying elements may quench the topological character of the host crystal through rotational symmetry breaking at compositions lower than the solubility limit. The study of the solubility limits of the REs in Cd_3As_2 is therefore prudent.

The stability of these potential alloys is captured by the Gibbs free energy of formation ΔG_f which can be approximated for a ternary alloy with constituents A, B, and C. It is a function of the composition-dependent enthalpy of formation $\Delta H_f(x)$ for its three binary systems (AB, AC, BC) and the enthalpy of mixing (105). The relevant equations are,

$$\Delta H_{f,ABC} = (1 - x_A)^2 \Delta H_{BC} + (1 - x_B)^2 \Delta H_{AC} + (1 - x_C)^2 \Delta H_{AB}, \quad (5.1)$$

and,

$$\Delta G_{f,ABC} = \Delta H_{f,ABC} - RT[x_A \ln(x_A) + x_B \ln(x_B) + x_C \ln(x_C)]. \quad (5.2)$$

Calculating these quantities is straightforward for binary alloys with well-established thermodynamic data and phase diagrams, but the data on many of the considered As-FRTM/RE and Cd-FRTM/RE systems are either limited or nonexistent. Because the enthalpy of formation is critical, especially at the low temperatures of Cd_3As_2 growth, a general model for the enthalpy of formation $\Delta H_{f,ABC}$ for these ternary systems is a necessity.

The empirical model for the enthalpy for formation for metallic alloys proposed by *Miedema et al.* is therefore employed (106). Relevant materials parameters are taken from the literature and the updated Entall database hosted by the Polish Academy of Sciences (106–108). The Miedema model parameters for Cd and As are closest to the class of metallic elements, such as the third-row transition metals. The full model only uses fixed parameters, so $\Delta H_{f,AB}$ is calculable from literature sources,

$$\Delta H_{f,AB} = \frac{2Pf(c^S)\left(c_A V_A^{\frac{2}{3}} + c_B V_B^{\frac{2}{3}}\right)}{\left(n_{ws}^A\right)^{-\frac{1}{3}} + \left(n_{ws}^B\right)^{-\frac{1}{3}}} \times \left[-(\Delta\phi^*)^2 + \frac{Q}{P}\Delta n_{ws}^{\frac{2}{3}} - \frac{R}{P}\right]. \quad (5.3)$$

The model parameters can be separated into the categories of empirically-derived constants (R, P, Q), fixed atomic parameters, and the surface concentration function $f(c^S)$.

The ratio Q/P = 9.4 V^2/(electrons$^{2/3}$Å^2) is nearly constant across a variety of many different metallic alloy systems as determined in the original model's work. For transition metal alloys P = 14.1 and for non-transition metal alloys P = 10.6. In the case that a transition metal is alloyed with

a non-transition metal, P = 12.3. The constant R is dependent on the valence of the considered metallic atoms and it pertains to the level of p-d orbital hybridization in their alloys. The FRTMs are considered transition metals in this analysis, but the REs with various configurations of the 4f orbitals are not. In the case that R represents a binary alloy between a transition metal and non-transition metal, the individual parameters R_i are multiplied together and then scaled by an additional phase-dependent factor of 1.00 for solid alloys and 0.73 for liquid alloys. For all other cases, such as alloys between two transition metals, $R = 0$.

The fixed atomic parameters for an element are its molar volume in a metallic alloy V_i, its electron density within the Wigner-Seitz cell of its pure metallic crystal n_{ws}, and its adjusted work function ϕ^* which has been modified according to the original work to account for the element's behavior in metallic alloys. The distinction between metallic atom volume in metallic alloys vs. in the pure metallic state is made because of its significant effect on V_i. Many parameters appear multiple times in the model as they are involved in more than one interaction associated with the enthalpy of formation, such as the enthalpy of solution and an enthalpy associated with the dipole created between dissimilar atoms.

The surface concentration function $f(c^S)$ is dependent on V_i and the constituent concentrations c_i, with variants for both disordered alloys,

$$f(c^s) = c_A^s c_B^s, \tag{5.4}$$

and for ordered alloys,

$$f(c^s) = c_A^s c_B^s [1 + 8(c_A^s c_B^s)^2]. \tag{5.5}$$

The individual constituent surface concentration is calculated via:

$$c_i^s = \frac{c_i V_i^{\frac{2}{3}}}{c_i V_i^{\frac{2}{3}} + c_j V_j^{\frac{2}{3}}}. \quad (5.6)$$

Because Cd_3As_2 is an ordered, stoichiometric compound, the intermetallic formed through alloying with a magnetic element is primarily considered using Equation 5.5. Relevant materials parameters are catalogued in
Table 5.2 (106–108). The considered constituent Cd-FRTM and As-FRTM binary systems use

$P = 12.3$.

Table 5.2: Fundamental atomic and empirical parameters used in the application of the Miedema model for the enthalpy of alloy formation in Cd-As-fourth row transition metal systems.

Element	V_i	n_{ws}	ϕ^*	R_i
Cd	13.00	1.91	4.05	1.40
As	11.85	3.00	4.80	2.30
Ti	10.58	3.51	3.80	1.00
V	8.36	4.41	4.25	1.00
Cr	7.23	5.18	4.65	1.00
Mn	7.35	4.17	4.45	1.00
Fe	7.19	5.55	4.93	1.00
Co	6.70	5.36	5.10	1.00
Ni	6.60	5.36	5.20	1.00

5.2 Instability of fourth-row transition metals in Cd_3As_2

As seen in Figure 5.1 and Figure 5.2, the theoretical ΔG_f values for the seven considered Cd-As-FRTM alloys border between somewhat negative (exothermic) and very positive (endothermic) values.

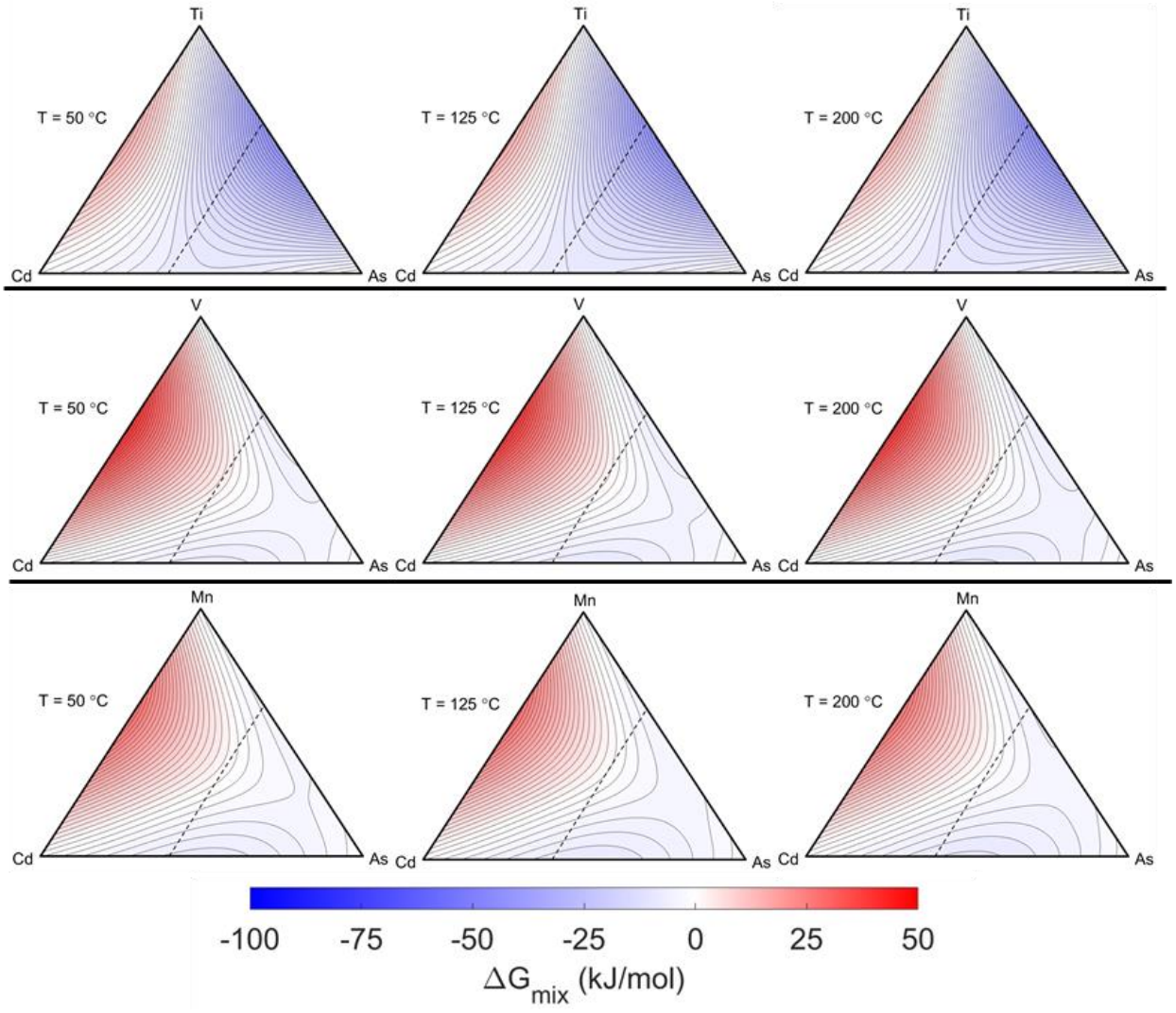

Figure 5.1: The Gibbs free energy of formation $\Delta G_f = \Delta G_{mix}$ for three Cd-As-Fourth Row Transition Metal (FRTM) systems with spontaneous formation for all compositions $(FRTM_xCd_{1-x})_3As_2$ where x is the atomic fraction of the FRTM. The dashed lines demarcate the ternary alloys belonging to this stoichiometric composition.

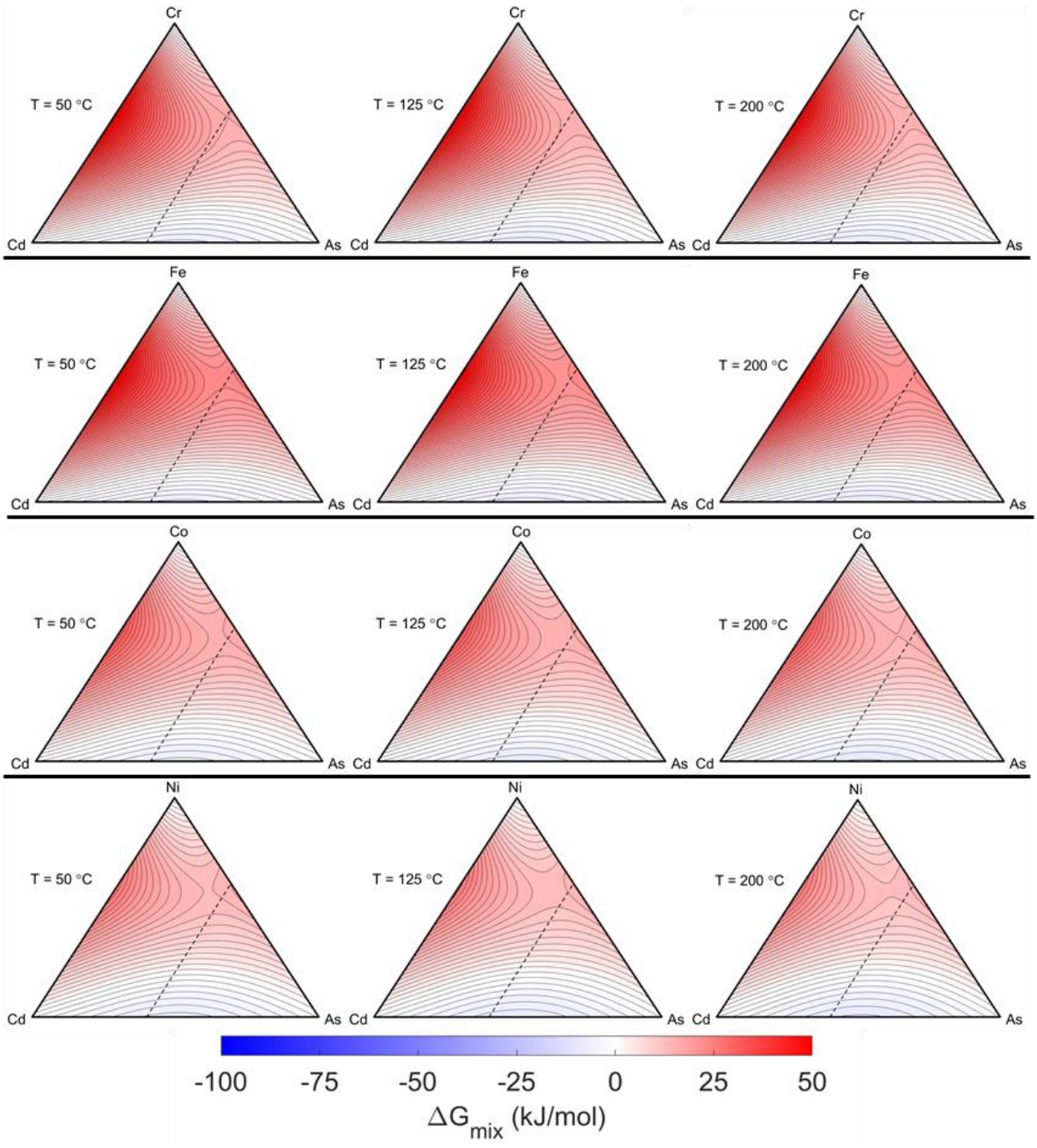

Figure 5.2: The Gibbs free energy of formation $\Delta G_f = \Delta G_{mix}$ for four Cd-As-Fourth Row Transition Metal (FRTM) systems with unfavorable formation at a specific composition $(\mathrm{FRTM_xCd_{1-x}})_3\mathrm{As_2}$ where x is the atomic fraction of the FRTM. The dashed lines demarcate the ternary alloys belonging to this stoichiometric composition.

These figures are separated based on whether the dashed line of stoichiometric alloying in Cd_3As_2 to maintain charge neutrality remains negative throughout (Ti, V, Mn) or not (Cr, Fe, Co, Ni). Unfortunately, the most positive ΔG_f values lie amongst the more commonly used magnetic FRTMs like Cr, Fe, and Co. According to this analysis, V and Mn are only just barely soluble across all potential stochiometric compositions $(V_xCd_{1-x})_3As_2$ and $(Mn_xCd_{1-x})_3As_2$.

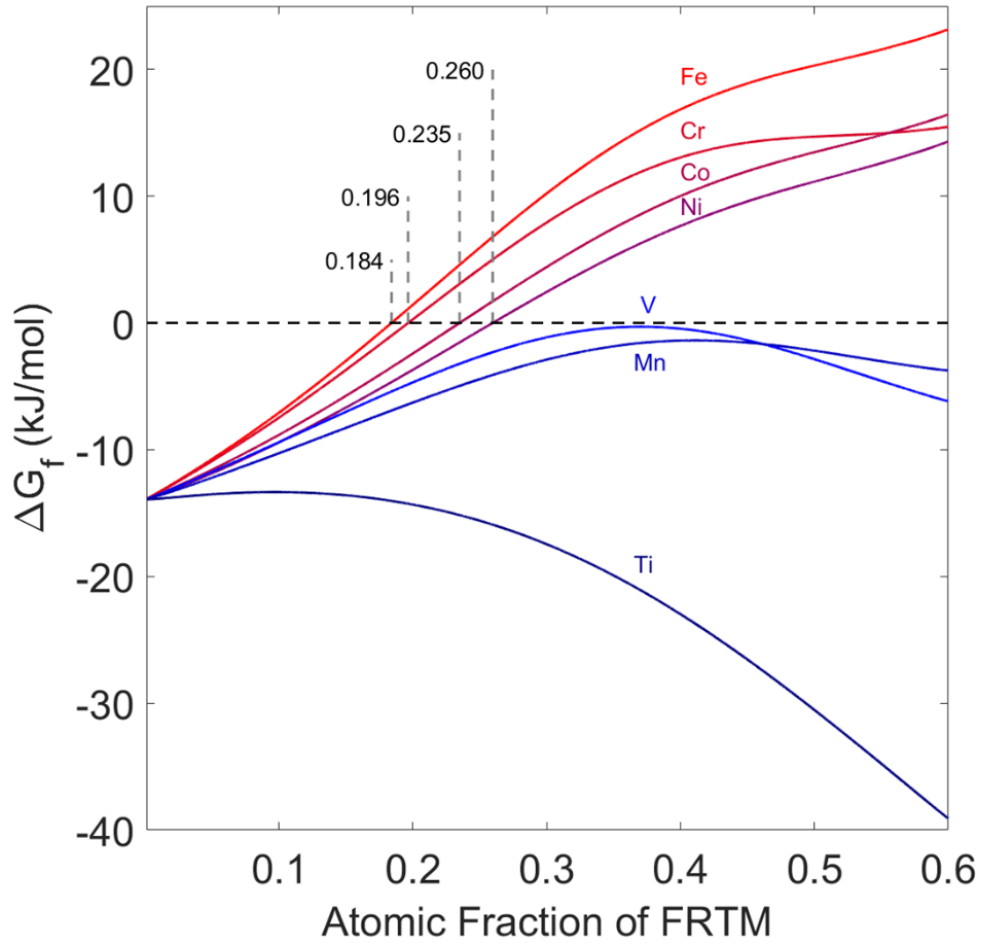

Figure 5.3: The Gibbs free energy of formation ΔG_f for all seven Cd-As-Fourth Row Transition Metal (FRTM) systems at 200 °C, plotted against the atomic FRTM fraction in the stoichiometric composition $(FRTM_xCd_{1-x})_3As_2$. Vertical dashed lines from left to right mark the atomic fractions for Fe, Cr, Co, and Ni where ΔG_f passes the line of spontaneous compound formation.

The 2D ternary cross sections of these seven FRTMs are compared against the line of spontaneous compound formation. The differences in alloying behaviors in Figure 5.3 are attributed to the large range of V_i, n_{ws}, and ϕ^* values amongst the FRTMs. One surprising result is that these curves suggest there is no solubility limit for Mn in the Cd_3As_2 system, in direct opposition to the experimental literature. The reality of attempted Mn alloying in Cd_3As_2 shows a strong drive towards the formation of topologically-trivial Mn-rich precipitates as opposed to a single phase based on the Cd_3As_2 crystal (103). For comparison with these Gibbs free energy calculations, the literature value for $\Delta G°_f$ of MnAs ranges from -55.2 to -61.6 kJ/mol based on its phase (79). This model-experiment disparity may be attributed to the fact the Miedema model is empirically-derived, and that the Gibbs free energies here consider only the energy of formation and the entropy of mixing. In addition, the interaction of As in these systems is done using parameters for metallic behavior, which needs confirmation through additional experimentation. It should be noted that the Miedema Mn curve is relatively close to crossing the dashed line of spontaneous reaction for the entirety of its compositional range.

The stability of these alloys is particularly linked to differences in n_{ws} and ϕ^* as their magnitudes influence the sign of the enthalpy of formation:

$$\mathrm{sgn}\left(\Delta H_{f,AB}\right) = \mathrm{sgn}\left[-P(\Delta\phi^*)^2 + Q\Delta n_{ws}^{2/3} - R\right]. \tag{5.7}$$

Because the Cd-FRTM and As-FRTM binaries are alloys containing one transition metal and one non-transition metal, they take the empirical parameter R into account as well. The contributions from the difference in adjusted work function $-P\Delta\phi^*$ and the difference in Wigner-Seitz cell

electron density $Q\Delta n_{ws}^{2/3}$ are on the same order, as illustrated by the transition from exothermic to endothermic ΔG_f in three of the considered alloys. Fe has the largest $Q\Delta n_{ws}^{2/3}$ amongst the FRTMs, which contributes to its curve with the most positive Gibbs free energy of formation. This also explains why the Cd-As-Ti system is the most stable, as Ti has both the smallest $Q\Delta n_{ws}^{2/3}$ and the most negative $-P\Delta\phi^*$ amongst the considered FRTMs.

5.3 Stability of rare earth elements in Cd_3As_2

Unlike the Cd-As-FRTM systems described above, the following Cd-As-RE alloys are all very negative in terms of their ΔG_f values.

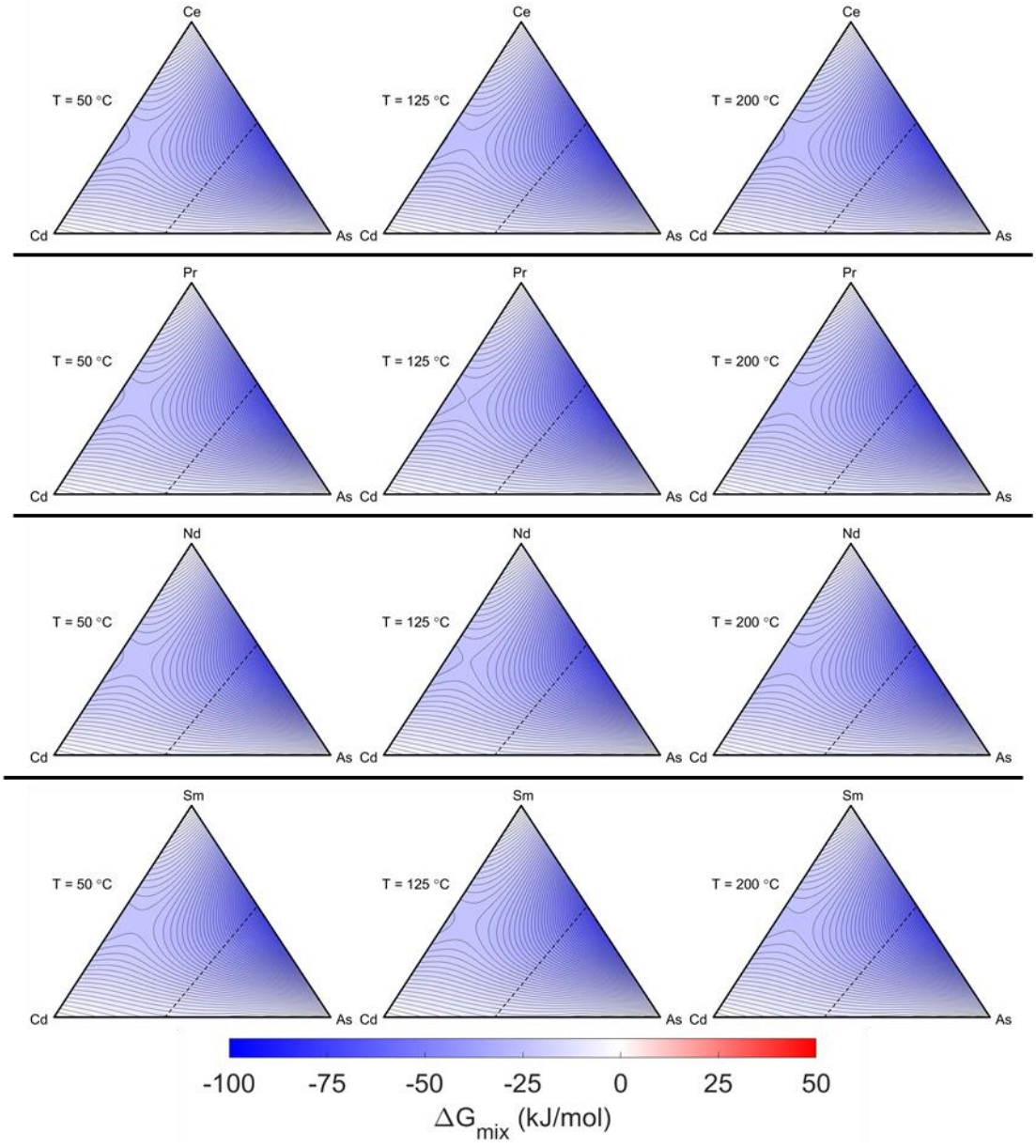

Figure 5.4: The Gibbs free energy of formation $\Delta G_f = \Delta G_{mix}$ for Cd-As-Rare Earth (RE) systems including the four lowest atomic number REs. The dashed lines demarcate the ternary alloys which belong to the stoichiometric composition $RE_xCd_{3(1-x)}As_{2-x}$.

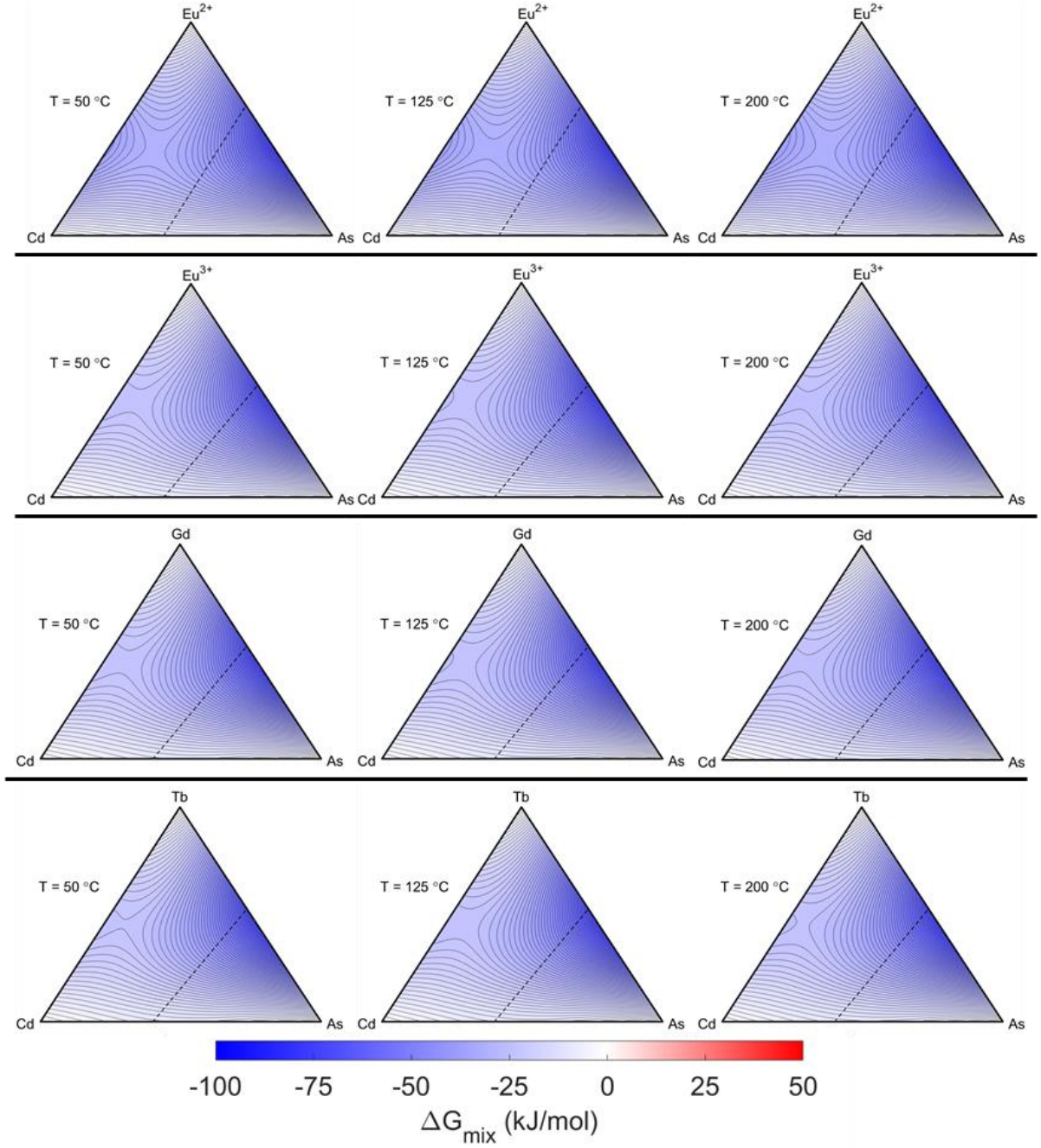

Figure 5.5: The Gibbs free energy of formation $\Delta G_f = \Delta G_{mix}$ for Cd-As-Rare Earth (RE) systems including the three medium atomic number REs, where both Eu^{2+} and Eu^{3+} are considered. The dashed lines demarcate the ternary alloys which belong to the stoichiometric composition $RE_xCd_{3(1-x)}As_{2-x}$ (3+ oxidation state alloys) and $(Eu_x^{2+}Cd_{1-x})_3As_2$.

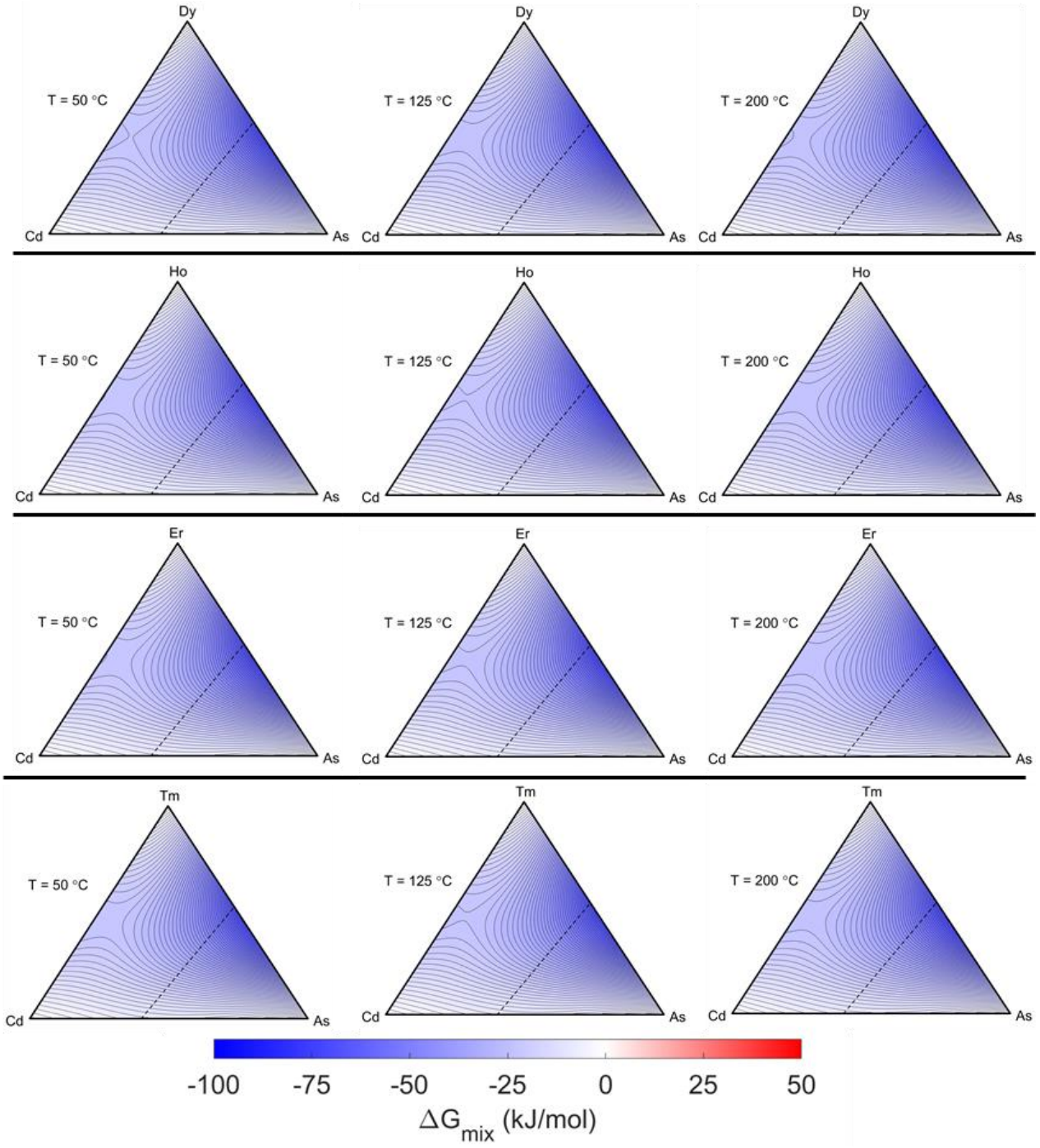

Figure 5.6: The Gibbs free energy of formation $\Delta G_f = \Delta G_{mix}$ for Cd-As-Rare Earth (RE) systems including the four highest atomic number REs. The dashed lines demarcate the ternary alloys which belong to the stoichiometric composition $\mathrm{RE}_x\mathrm{Cd}_{3(1-\mathrm{x})}\mathrm{As}_{2-\mathrm{x}}$.

In fact, there is not a single point in any of the twelve systems where ΔG_f is positive, and it is only zero at the pure element compositions. Furthermore, the incorporation of RE elements into the Cd-As system actually decreases ΔG_f monotonically with increasing RE atomic fraction.

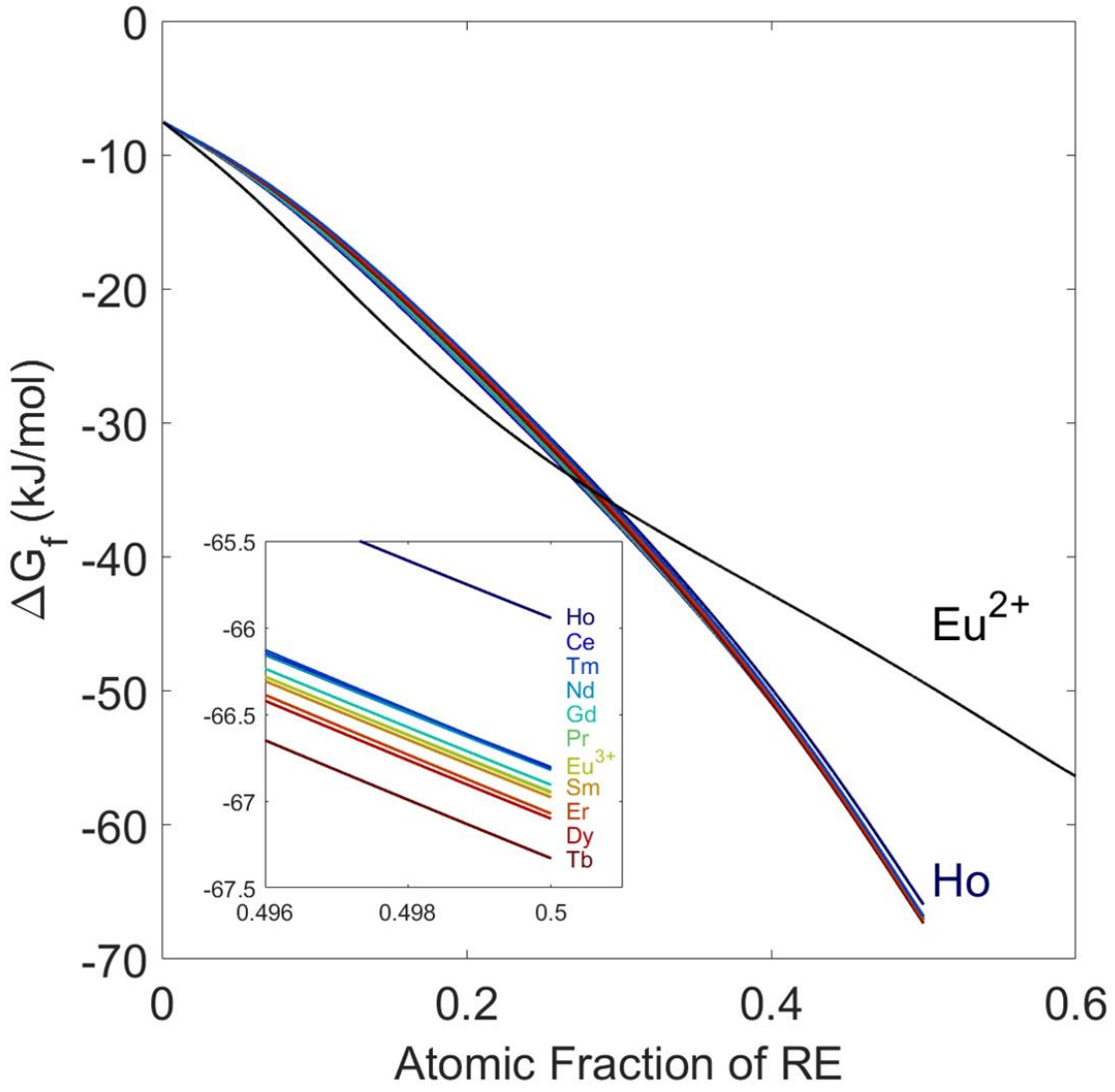

Figure 5.7: The Gibbs free energy of formation ΔG_f for all twelve Cd-As-Rare Earth (RE) systems at 200 °C plotted against the atomic fraction of RE x in the stoichiometric compositions $RE_xCd_{3(1-x)}As_{2-x}$ (3+ oxidation state alloys) and $(Eu_x^{2+}Cd_{1-x})_3As_2$. A zoomed section shows the closely-spaced end sections of the lines, excluding Eu^{2+}.

Unsurprisingly, the similarity in V_i, n_{ws}, and ϕ^* values for the REs in Table 5.3 makes the ΔG_f curves in Figure 5.7 extremely similar. The only outlier is the Cd-As-Eu^{2+} system, which is necessarily different due its unique charge-neutral stoichiometry $(Eu_x^{2+}Cd_{1-x})_3As_2$ amongst these RE alloys. A zoomed subplot of the $RE_xCd_{3(1-x)}As_{2-x}$ alloys is included to compare them at their compositional endpoints. There is no apparent correlation between ΔG_f and atomic number, irrespective of composition. Since none of the elements in these alloy systems are transition metals there is no further negative contribution from an R term. The DFT-calculated energies of formation for some common RE-As systems are detailed in Table 6.3 for comparison with these theoretical Miedema curves. The binary compound energies of formation are generally more negative than the lowest charge-neutral stoichiometry value of their related RE-Cd_3As_2 system.

Table 5.3: Fundamental atomic and empirical parameters used in the application of the Miedema model for the enthalpy of alloy formation in Cd-As-Rare Earth (RE) systems. $P = 10.6$ for the considered constituent Cd-RE and As-RE binary systems.

Element	V_i	n_{ws}	ϕ^*	R_i
Ce	21.62	1.69	3.18	0.70
Pr	20.79	1.73	3.19	0.70
Nd	20.58	1.73	3.19	0.70
Sm	20.01	1.77	3.20	0.70
Eu2+	28.95	0.68	2.50	0.70
Eu3+	19.97	1.77	3.20	0.70
Gd	19.97	1.77	3.20	0.70
Tb	19.32	1.82	3.21	0.70
Dy	19.00	1.82	3.21	0.70
Ho	18.76	1.82	3.22	0.70
Er	18.45	1.86	3.22	0.70
Tm	18.12	1.86	3.22	0.70

Table 5.4: Theoretical energies of formation for lowest-energy rare Earth arsenides according to density functional theory conducted by the Materials Project (109).

Compound	Space Group	Formation Energy (eV/atom)	$\Delta^{\circ}G_f$ (kJ/mol)
CeAs	$Fm\bar{3}m$ (#225)	-1.761	-169.9
PrAs	$Fm\bar{3}m$ (#225)	-1.760	-169.8
NdAs	$Fm\bar{3}m$ (#225)	-1.781	-171.9
SmAs	$Fm\bar{3}m$ (#225)	-1.799	-173.6
Eu_4As_3	$I\bar{4}3d$ (#220)	-1.228	-118.5
EuAs	$P\bar{6}2m$ (#189)	-1.144	-110.4
GdAs	$Fm\bar{3}m$ (#225)	-1.745	-168.4
TbAs	$Fm\bar{3}m$ (#225)	-1.820	-175.6
DyAs	$Fm\bar{3}m$ (#225)	-1.811	-174.7
HoAs	$Fm\bar{3}m$ (#225)	-1.799	-173.6
ErAs	$Fm\bar{3}m$ (#225)	-1.781	-171.9
TmAs	$Fm\bar{3}m$ (#225)	-1.776	-171.3

5.4 Considerations for the magnetic proximity effect

While the theoretical solubility of these RE elements in Cd_3As_2 appears promising, another strategy may be necessary in the case that no RE will complete the goals of both maintaining topological behavior and breaking *T* symmetry via an internal magnetic field. In this case, an alternative is the application of a magnetic layer grown pseudomorphically on Cd_3As_2. This arrangement leverages the effect of magnetic proximity, where a magnetic layer is deposited in contact with a topological material. The adjacent magnetic field extends into the topological crystal to break *T* symmetry. For example, the magnetic proximity effect has been demonstrated through the deposition of amorphous Fe on the TI system $Bi_{2-x}Mn_xTe_3$ (110). Here, TI Bi_2Se_3 is alloyed with a minimal amount of Mn ($x = 0.09$) which is then magnetized through close proximity to the ferromagnetic Fe layer. Such low alloying contents are familiar to the magnetic alloying of Cd_3As_2 with FRTMs, and so the same magnetic proximity effect may also be applied here. Even if the newly considered REs also possess the same low experimental solubility in the Cd-As system as the FRTMs do, the deposition of an adjacent magnetic RE-compound may induce magnetism in minimally-alloyed Cd_3As_2. There are many candidate layers including the pure REs and their arsenides/antimonides. The major obstacle associated with this scheme, however, is finding a magnetic layer which is nearly lattice-matched with Cd_3As_2. In addition, such a layer is limited to low-temperature, amorphous deposition if growth occurs after the thermally vulnerable Cd_3As_2 layer has been placed. As such, a magnetic RE-(As,Sb) layer for the magnetic proximity effect would ideally be minimally mismatched and low-thickness so that it may be pseudomorphically grown on the metamorphic ternary virtual substrates. It would then be strained by the ternary buffer so that it is lattice matched with the magnetically-alloyed Cd_3As_2 layer above, preserving the topological surface states of the TS-Cd_3As_2 through the minimization of interfacial strain.

The relevant lattice parameters of RE arsenides and antimonides are shown in Table 5.5.

Table 5.5: Lowest-energy rare Earth arsenides and antimonides for potential magnetic interfaces with $I4_1/acd$ Cd_3As_2. The lattice mismatch between the (001) plane of these compounds and the As FCC sublattice spacing of (001)-oriented Cd_3As_2 (6.317 Å) is also calculated.

Compound	Space Group	Lattice Parameter(s) (Å)	Lattice Mismatch (%)
CeAs	$Fm\bar{3}m$ (#225)	a = 6.08, 6.079 (111,112)	-3.75 , -3.76
CeSb	$Fm\bar{3}m$ (#225)	a = 6.42, 6.4237 (111,113)	+1.64 , +1.69
PrAs	$Fm\bar{3}m$ (#225)	a = 6.031 (114)	-4.52
PrSb	$Fm\bar{3}m$ (#225)	a = 6.3822 (113)	+1.04
NdAs	$Fm\bar{3}m$ (#225)	a = 5.995, 5.984 (115,116)	-5.09 , -5.27
NdSb	$Fm\bar{3}m$ (#225)	a = 6.3384(3) (113)	+0.34
SmAs	$Fm\bar{3}m$ (#225)	a = 5.91, 5.917 (117,118)	-6.44, -6.33
SmSb	$Fm\bar{3}m$ (#225)	a = 6.2706(1) (113)	-0.73
Eu_4As_3	$I\bar{4}3d$ (#220)	a = 9.214, 9.214 (119,120)	+45.87
$Eu_{16}Sb_{11}$	$P2_12_12_1$ (#19)	a = 12.67, c = 11.720 (121)	+100.65
GdAs	$Fm\bar{3}m$ (#225)	a = 5.861, 5.86 (122,123)	-7.21, -7.23
GdSb	$Fm\bar{3}m$ (#225)	a = 6.2194, 6.22 (113,123)	-1.54, -1.53
TbAs	$Fm\bar{3}m$ (#225)	a = 5.855, 5.823 (124,125)	-7.31, -7.82
TbSb	$Fm\bar{3}m$ (#225)	a = 6.1822(5) (113)	-2.13
DyAs	$Fm\bar{3}m$ (#225)	a = 5.795 (126)	-8.26
DySb	$Fm\bar{3}m$ (#225)	a = 6.1316 (113)	-2.93
HoAs	$Fm\bar{3}m$ (#225)	a = 5.768 Å, 5.769 (116,127)	-8.69, -8.67
HoSb	$Fm\bar{3}m$ (#225)	a = 6.1307 (113)	-2.94
ErAs	$Fm\bar{3}m$ (#225)	a = 5.743 (128)	-9.08
ErSb	$Fm\bar{3}m$ (#225)	a = 6.1089 (113)	-3.29
TmAs	$Fm\bar{3}m$ (#225)	a = 5.716 (129)	-9.51
TmSb	$Fm\bar{3}m$ (#225)	a = 6.16 (130)	-2.48

Unsurprisingly, the similar atomic properties of these REs (with the exception of Eu) cause their arsenides and antimonides to form the same cubic, rock salt-type crystal. Their $Fm\bar{3}m$ compounds are reported to have anti-ferromagnetic ordering as bulk materials, but this may not be the case for

very thin layers. The majority of these compounds have a negative lattice mismatch with the As FCC sublattice. The early and middle RE antimonides such as PrSb, NdSb, and SmSb possess relatively small mismatch with Cd_3As_2. $Eu_{11}Sb_{16}$ also appears to be an excellent candidate when considering its lattice mismatch with the full Cd_3As_2 unit cell a parameter. The critical thicknesses of these compounds on a = 6.317 Å ternary III-V alloy buffers are reported in Table 5.6.

Table 5.6: Calculated critical thicknesses for magnetic rare Earth-(As,Sb) layers on ternary III-V alloy layers with a = 6.317 Å. Compounds with no solution (—) will immediately form a metamorphic interface instead of a pseudomorphic layer with a real critical thickness.

Compound	Largest Absolute Lattice Mismatch	Critical Thickness (nm)
CeAs	-3.76 %	—
CeSb	+1.69 %	125.5
PrAs	-4.52 %	—
PrSb	+1.04 %	443.4
NdAs	-5.27 %	—
NdSb	+0.34 %	6060
SmAs	-6.44 %	—
SmSb	-0.73 %	1013
Eu_4As_3	+45.87 %	—
$Eu_{16}Sb_{11}$	+0.32 %*	3136
GdAs	-7.23 %	—
GdSb	-1.54 %	149.4
TbAs	-7.82 %	—
TbSb	-2.13 %	58.44
DyAs	-8.26 %	—
DySb	-2.93 %	18.22
HoAs	-8.69 %	—
HoSb	-2.94 %	17.79
ErAs	-9.08 %	—
ErSb	-3.29 %	—
TmAs	-9.51 %	—
TmSb	-2.48 %	35.35

The critical thicknesses are determined using the highest lattice mismatch corresponding to the lattice parameters reported in Table 5.5. The substrate lattice parameter a = 6.317 Å is used, except for $Eu_{16}Sb_{11}$ where the Cd_3As_2 unit cell a = 12.633 Å is used instead.

According to these calculations, not a single considered RE arsenide can be pseudomorphically grown on a ternary III-V. Amongst the antimonides, the best candidate for pseudomorphic growth appears to be NdSb, followed by $Eu_{11}Sb_{16}$ and then SmSb. Even more RE antimonides are available with critical thickness values in excess of that required to achieve the magnetic proximity effect. A variety of options allows for the consideration of other source properties, such as the relatively high vapor pressures of Eu and Sm which makes them more favorable for lower-temperature MBE growth (131). The vapor pressures of elemental Nd, Sm, and Eu at 800 °C are 1.04×10^{-5}, 7.15, ~80 Pa. Note that the vapor pressure fit for Nd data is over a data range of 1255 to 1650 °C, so interpolated values exist only at high effusion cell temperatures. Because there are several Eu antimonides and two common Eu oxidation states, Sm may be preferable by having fewer parameters to consider during MBE and structural analysis. An important source of error in these calculations would be any change in the Cd_3As_2 a lattice parameter as it is magnetically alloyed in preparation for the magnetic proximity effect. In this regard, the ideal RE-(As,Sb) overlayer may vary.

Chapter 6: Summary and Future Work

6.1 Summary

A series of molecular beam epitaxy growths were conducted to explore the accessibility and nature of topological semimetal Cd_3As_2 on ternary III-V alloy virtual substrates. The motivation was to lattice match these ternary alloys with the interatomic As distance of the $I4_1/acd$ Cd_3As_2 unit cell so that the topological semimetal overlayer could be studied in a state of minimal biaxial strain. These heterostructures were studied via *in situ* reflection high-energy electron diffraction and pyrometry, high-resolution X-ray diffraction including reciprocal space mapping, X-ray reflectivity, atomic force microscopy, cross-sectional scanning electron microscopy, transmission electron microscopy, and low-temperature Van der Pauw-geometry Hall measurements.

Three ternary III-V alloy systems $Ga_xIn_{1-x}Sb$, $Al_xIn_{1-x}Sb$, and $InAs_xSb_{1-x}$ were explored for the presence of spinodal and thermal decomposition at temperatures from room temperature to 505 °C. X-ray diffraction ω-2θ spectra and reciprocal space maps suggest that no appreciable phase separation of these ternary alloys occurs, even after cooling to room temperature. Transmission electron microscopy conducted on select heterostructures confirms that there is no phase separation and shows that the $Al_xIn_{1-x}Sb$ system has the lowest surface-level threading dislocation density. In terms of reaction with a potential Cd_3As_2 overlayer, Gibbs free energy calculations following the delta lattice parameter model show that the proposed reactions are generally either highly favorable or unfavorable. The AlInSb ternary buffer system appears to be the best candidate as it does not have any spontaneous interfacial or overpressure exchange reactions over the experimental temperature range. Reciprocal space maps of these systems were

analyzed using the theory by *Kaganer et al.* to correlate spot ellipticity with misfit and non-misfit defect densities, showing that the $Al_xIn_{1-x}Sb$ system exhibits the smallest deviation from the perfect case. $Al_xIn_{1-x}Sb$ was therefore applied as the primary virtual substrate system for growth of lattice-matched Cd_3As_2 due to its endothermic Gibbs free energy interactions with Cd_3As_2, its relatively low surface-level threading dislocation densities, and its favorable reciprocal space map analysis. All three ternary III-V alloy systems are suitable as virtual substrates for the low-temperature molecular beam epitaxy of lattice-matched Cd_3As_2 using a molecular source.

Cadmium arsenide films were grown as part of three experimental series following the variables of substrate temperature during growth, As_2 overpressure during growth, and engineered interfacial strain as a function of ternary alloy composition. Substrate growth temperature limits of 170-200 °C and 145 °C were determined for open and valved Knudsen cell sources. The As_2 overpressure series showed that the Cd_3As_2 c parameter moves closer to the ideal literature value of 6.317 Å as the applied overpressure increases up until a maximum limit of 1.0×10^{-6} mbar. A further overpressure of 1.5×10^{-6} mbar significantly reduced the quality of the film according to a sharp increase in its $(00\underline{16})$ peak full-width at half-maximum. The strain series explored the limits of Cd_3As_2 growth up to a maximum in-plane biaxial tensile strain of +0.136 %. This series was subjected to Van der Pauw Hall measurements at 2 K which produced Shubnikov-de Haas oscillations corresponding to the Landau levels $\upsilon = \pm1$ for all but the most-strained film. The carrier mobility appears to increase as the film strain moves closer to zero.

The potential for alloying these films with magnetic elements from the third-row transition metals and fourth-row rare-earth metals was explored using the empirical model proposed by *Miedema et al.* for the formation of intermetallic alloys. The application of these enthalpies of alloy formation in solving for ternary system Gibbs free energies was used to determine how

energetically stable twenty magnetic element-Cd-As alloys are over a series of temperatures and compositions. It was found that the third-row transition metals have regions of both endothermic and exothermic formation energies, but the fourth-row rare-earth metals consistently exhibit extremely negative formation energies. The magnetic compounds associated with these rare-earth elements are also reviewed for their applicability as magnetic underlayers for the magnetic proximity effect in minimally-alloyed Cd_3As_2. Sm appears to be a good candidate for exploring the quantum anomalous Hall effect in Cd_3As_2 as it has a relatively low vapor pressure for sufficient flux at moderate MBE temperatures and its antimonide has low lattice-mismatch with the Cd_3As_2 interatomic As distance.

6.2 Future Work

Future work on this project may be separated into the general categories of the improvement of pure Cd_3As_2 electronic properties and the application of a magnetic component for *T* symmetry breaking to realize the quantum anomalous Hall effect.

While current carrier mobilities are sufficient for the presence of Shubnikov-de Haas oscillations, a greater mobility corresponds to the observation of these oscillations at smaller absolute magnetic fields. With regards to the quantum Hall effect, this would manifest in the appearance of more Hall plateaus belonging to the filling of additional Landau levels. For the quantum anomalous Hall effect, the current minimum Hall plateau appearance field of 5 T may be too high for magnetically-alloyed Cd_3As_2 or proximal magnetic layers to achieve. Following the general increase in Cd_3As_2 mobility with decreasing tensile stress, a further series of in-plane compressive strains between should be investigated to find an optimum in maximized carrier mobility. In addition, this data should be used to find the compressive strain limit for the growth of topological semimetal Cd_3As_2.

The work on *T* symmetry breaking through a ferromagnetic heterostructure component has thus far been theoretical. Following considerations of suitability for both rare earth-alloying of Cd_3As_2 and the pseudomorphic growth of proximal ferromagnets, Sm has been chosen as the best candidate for both strategies. Attempts will be made to incorporate it into Cd_3As_2 while still maintaining the host crystal's topological character. In addition, thin SmSb films will be pseudomorphically on ternary buffers to attempt the acquisition of the quantum anomalous Hall effect in a Cd_3As_2 overlayer via the magnetic proximity effect.

Bibliography

1. Hasan MZ, Kane CL. Colloquium: Topological insulators. Rev Mod Phys. 2010 Nov 8;82(4):3045–67.
2. Yan B, Felser C. Topological Materials: Weyl Semimetals. Annu Rev Condens Matter Phys. 2017 Mar 31;8(1):337–54.
3. Thouless DJ, Kohmoto M, Nightingale MP, den Nijs M. Quantized Hall Conductance in a Two-Dimensional Periodic Potential. Phys Rev Lett. 1982 Aug 9;49(6):405–8.
4. Burkov AA. Topological semimetals. Nat Mater. 2016;15(11):1145–8.
5. Zheng H, and Zahid Hasan M. Quasiparticle interference on type-I and type-II Weyl semimetal surfaces: a review. Adv Phys X. 2018 Jan 1;3(1):1466661.
6. Lv BQ, Muff S, Qian T, Song ZD, Nie SM, Xu N, et al. Observation of Fermi-Arc Spin Texture in TaAs. Phys Rev Lett. 2015 Nov 16;115(21):217601.
7. Kargarian M, Randeria M, Lu YM. Are the surface Fermi arcs in Dirac semimetals topologically protected? Proceedings of the National Academy of Sciences. 2016 Aug 2;113(31):8648–52.
8. Uchida M, Nakazawa Y, Nishihaya S, Akiba K, Kriener M, Kozuka Y, et al. Quantum Hall states observed in thin films of Dirac semimetal Cd3As2. Nat Commun. 2017;8(1):2274.
9. He QL, Hughes TL, Armitage NP, Tokura Y, Wang KL. Topological spintronics and magnetoelectronics. Nat Mater. 2022;21(1):15–23.
10. Novoselov KS, Geim AK, Morozov S V, Jiang D, Katsnelson MI, Grigorieva I V, et al. Two-dimensional gas of massless Dirac fermions in graphene. Nature. 2005;438(7065):197–200.
11. Tokura Y, Kanazawa N. Magnetic Skyrmion Materials. Chem Rev. 2021 Mar 10;121(5):2857–97.
12. Akhmerov AR, Nilsson J, Beenakker CWJ. Electrically Detected Interferometry of Majorana Fermions in a Topological Insulator. Phys Rev Lett. 2009 May 28;102(21):216404.
13. Zhang H, Liu CX, Qi XL, Dai X, Fang Z, Zhang SC. Topological insulators in Bi2Se3, Bi2Te3 and Sb2Te3 with a single Dirac cone on the surface. Nat Phys. 2009;5(6):438–42.
14. Wang LL, Johnson DD. Ternary tetradymite compounds as topological insulators. Phys Rev B. 2011 Jun 29;83(24):241309.

15. Ali MN, Gibson Q, Jeon S, Zhou BB, Yazdani A, Cava RJ. The Crystal and Electronic Structures of Cd3As2, the Three-Dimensional Electronic Analogue of Graphene. Inorg Chem. 2014 Apr 21;53(8):4062–7.

16. Hsieh D, Qian D, Wray L, Xia Y, Hor YS, Cava RJ, et al. A topological Dirac insulator in a quantum spin Hall phase. Nature. 2008;452(7190):970–4.

17. Tung Y, Chiang YF, Chong CW, Deng ZX, Chen YC, Huang JCA, et al. Growth and characterization of molecular beam epitaxy-grown Bi2Te3−xSex topological insulator alloys. J Appl Phys. 2016 Feb 2;119(5):55303.

18. Küfner S, Fitzner M, Bechstedt F. Topological α-Sn surface states versus film thickness and strain. Phys Rev B. 2014 Sep 22;90(12):125312.

19. Kane CL, Mele EJ. Quantum Spin Hall Effect in Graphene. Phys Rev Lett. 2005 Nov 23;95(22):226801.

20. Li J, Chu RL, Jain JK, Shen SQ. Topological Anderson Insulator. Phys Rev Lett. 2009 Apr 1;102(13):136806.

21. J M Kosterlitz, D J Thouless. Long range order and metastability in two dimensional solids and superfluids. (Application of dislocation theory). Journal of Physics C: Solid State Physics. 1972;5(11):L124.

22. Wang C, Zhang H, Yuan H, Zhong J, Lu C. Universal numerical calculation method for the Berry curvature and Chern numbers of typical topological photonic crystals. Frontiers of Optoelectronics. 2020;13(1):73–88.

23. Chang CZ, Zhang J, Feng X, Shen J, Zhang Z, Guo M, et al. Experimental Observation of the Quantum Anomalous Hall Effect in a Magnetic Topological Insulator. Science (1979). 2013 Apr 12;340(6129):167 LP – 170.

24. Qi XL, Zhang SC. The quantum spin Hall effect and topological insulators. Phys Today. 2010 Jan 1;63(1):33–8.

25. Kane CL, Mele EJ. Z2 Topological Order and the Quantum Spin Hall Effect. Phys Rev Lett. 2005 Sep 28;95(14):146802.

26. Kitaev AYu. Fault-tolerant quantum computation by anyons. Ann Phys (N Y). 2003;303(1):2–30.

27. Dennis E, Kitaev A, Landahl A, Preskill J. Topological quantum memory. J Math Phys. 2002 Aug 20;43(9):4452–505.

28. Wray LA. Topological transistor. Nat Phys. 2012;8(10):705–6.

29. Yan B, Zhang SC. Topological materials. Reports on Progress in Physics. 2012;75(9):96501.

30. Vergniory MG, Elcoro L, Felser C, Regnault N, Bernevig BA, Wang Z. A complete catalogue of high-quality topological materials. Nature. 2019;566(7745):480–5.

31. Goyal M, Galletti L, Salmani-Rezaie S, Schumann T, Kealhofer DA, Stemmer S. Thickness dependence of the quantum Hall effect in films of the three-dimensional Dirac semimetal Cd3As2. APL Mater. 2018 Feb 1;6(2):26105.

32. Pardue TN, Goyal M, Guo B, Salmani-Rezaie S, Kim H, Heinonen O, et al. Controlling the symmetry of cadmium arsenide films by epitaxial strain. APL Mater. 2021 May 1;9(5):51111.

33. Crassee I, Sankar R, Lee WL, Akrap A, Orlita M. 3D Dirac semimetal Cd3As2: A review of material properties. Phys Rev Mater. 2018 Dec 26;2(12):120302.

34. Neupane M, Xu SY, Sankar R, Alidoust N, Bian G, Liu C, et al. Observation of a three-dimensional topological Dirac semimetal phase in high-mobility Cd3As2. Nat Commun. 2014;5(1):3786.

35. Jay-Gerin JP, Aubin MJ, Caron LG. The electron mobility and the static dielectric constant of Cd3As2 at 4.2 K. Solid State Commun. 1977;21(8):771–4.

36. Cheng L, Liu Y. What Limits the Intrinsic Mobility of Electrons and Holes in Two Dimensional Metal Dichalcogenides? J Am Chem Soc. 2018 Dec 26;140(51):17895–900.

37. Umansky V, de-Picciotto R, Heiblum M. Extremely high-mobility two dimensional electron gas: Evaluation of scattering mechanisms. Appl Phys Lett. 1997 Aug 4;71(5):683–5.

38. Li H, He H, Lu HZ, Zhang H, Liu H, Ma R, et al. Negative magnetoresistance in Dirac semimetal Cd3As2. Nat Commun. 2016;7(1):10301.

39. Chen ZG, Zhang C, Zou Y, Zhang E, Yang L, Hong M, et al. Scalable Growth of High Mobility Dirac Semimetal Cd3As2 Microbelts. Nano Lett. 2015 Sep 9;15(9):5830–4.

40. Kealhofer DA, Kim H, Schumann T, Goyal M, Galletti L, Stemmer S. Basal-plane growth of cadmium arsenide by molecular beam epitaxy. Phys Rev Mater. 2019 Mar 19;3(3):31201.

41. Schumann T, Goyal M, Kim H, Stemmer S. Molecular beam epitaxy of Cd3As2 on a III-V substrate. APL Mater. 2016 Dec 1;4(12):126110.

42. Jalil MBA, Tan SG, Siu ZB. Quantum anomalous Hall effect in topological insulator memory. J Appl Phys. 2015 Apr 8;117(17):17C739.

43. Tian J, Chang C, Cao H, He K, Ma X, Xue Q, et al. Quantum and Classical Magnetoresistance in Ambipolar Topological Insulator Transistors with Gate-tunable Bulk and Surface Conduction. Sci Rep. 2014;4(1):4859.

44. Ainsworth R, Slingerland JK. Topological qubit design and leakage. New J Phys. 2011;13(6):65030.

45. Cheng M, Lutchyn RM, Das Sarma S. Topological protection of Majorana qubits. Phys Rev B. 2012 Apr 16;85(16):165124.

46. Farinha TG, Supple E, Gorman BP, Richardson CJK. Abrupt ternary III–V metamorphic buffers. J Appl Phys [Internet]. 2024 May 2;135(17):175304. Available from: https://doi.org/10.1063/5.0203835

47. Adachi S. Iii-v ternary and quaternary compounds. In: Kasap S, Capper P, editors. Springer Handbooks. Cham: Springer International Publishing; 2017. p. 725–41.

48. Margrave J. L. The Characterization of High-Temperature Vapors. Hoboken: Wiley; 1967.

49. Umansky V, Heiblum M, Levinson Y, Smet J, Nübler J, Dolev M. MBE growth of ultra-low disorder 2DEG with mobility exceeding 35×106cm2/Vs. J Cryst Growth. 2009;311(7):1658–61.

50. Wallart X, Lastennet J, Vignaud D, Mollot F. Performances and limitations of InAs⁄InAlAs metamorphic heterostructures on InP for high mobility devices. Appl Phys Lett. 2005 Jul 19;87(4):43504.

51. Thomas C, Hatke AT, Tuaz A, Kallaher R, Wu T, Wang T, et al. High-mobility InAs 2DEGs on GaSb substrates: A platform for mesoscopic quantum transport. Phys Rev Mater. 2018 Oct 18;2(10):104602.

52. Smith D. L. Thin-Film Deposition: Principles and Practice. 1st ed. New_York: McGraw-Hill; 1995. 1–616 p.

53. Oh JE, Bhattacharya PK, Chen YC, Tsukamoto S. Molecular-beam epitaxial growth of high-quality InSb on InP and GaAs substrates. J Appl Phys. 1989 Oct 15;66(8):3618–21.

54. Wilk A, Genty F, Fraisse B, Boissier G, Grech P, El Gazouli M, et al. MBE growth of InAs/InAsSb/AlAsSb structures for mid-infrared lasers. J Cryst Growth. 2001;223(3):341–8.

55. Foxon CT, Joyce BA. Interaction kinetics of As4 and Ga on {100} GaAs surfaces using a modulated molecular beam technique. Surf Sci. 1975;50(2):434–50.

56. Kaspi R, Evans KR. Sb-surface segregation and the control of compositional abruptness at the GaAsSbGaAs interface. J Cryst Growth. 1997;175–176:838–43.

57. Denton AR, Ashcroft NW. Vegard's law. Phys Rev A (Coll Park). 1991 Mar 1;43(6):3161–4.

58. Farrow RFC. Molecular beam epitaxy: applications to key materials. Elsevier; 1995.

59. SpringThorpe AJ, Ingrey SJ, Emmerstorfer B, Mandeville P, Moore WT. Measurement of GaAs surface oxide desorption temperatures. Appl Phys Lett. 1987 Jan 12;50(2):77–9.

60. Murdick DA, Zhou XW, Wadley HNG, Nguyen-Manh D. Predicting surface free energies with interatomic potentials and electron counting. Journal of Physics: Condensed Matter. 2005;17(39):6123.

61. Ohtake A, Ozeki M, Yasuda T, Hanada T. Atomic structure of the GaAs (001) — (2×4) surface under As flux. Phys Rev B. 2002 Apr 5;65(16):165315.

62. Drossel B, Kardar M. Phase Ordering and Roughening on Growing Films. Phys Rev Lett. 2000 Jul 17;85(3):614–7.

63. Muszalski J. Pyrometric interferometry during MBE growth of laser heterostructures. Thin Solid Films. 2000;367(1):299–301.

64. Speakman SA. Introduction to high resolution x-ray diffraction of epitaxial thin films. MIT Center for Materials Science and Engineering, Cambridge. 2012;

65. Harrington GF, Santiso J. Back-to-Basics tutorial: X-ray diffraction of thin films. J Electroceram. 2021;47(4):141–63.

66. Kriegner DWESJ. xrayutilities: a versatile tool for reciprocal space conversion of scattering data recorded with linear and area detectors. J Appl Crystallogr. 2013 Jul 18;46(4):1162–70.

67. Murphy ST, Chroneos A, Jiang C, Schwingenschlögl U, Grimes RW. Deviations from Vegard's law in ternary III-V alloys. Phys Rev B. 2010 Aug 3;82(7):73201.

68. Lindemuth J. Hall Effect Measurement Handbook. Dodrill B, editor. Lakeshore;

69. Oliveira FS, Cipriano RB, da Silva FT, Romão EC, dos Santos CAM. Simple analytical method for determining electrical resistivity and sheet resistance using the van der Pauw procedure. Sci Rep [Internet]. 2020;10(1):16379. Available from: https://doi.org/10.1038/s41598-020-72097-1

70. Shah VA, Dobbie A, Myronov M, Leadley DR. Reverse graded SiGe/Ge/Si buffers for high-composition virtual substrates. J Appl Phys. 2010 Mar 15;107(6):64304.

71. Richardson CJK, Lee ML. Metamorphic epitaxial materials. MRS Bull. 2016/03/14. 2016;41(3):193–8.

72. Dura JA, Vigliante A, Golding TD, Moss SC. Epitaxial growth of Sb/GaSb structures: An example of V/III-V heteroepitaxy. J Appl Phys. 1995 Jan 1;77(1):21–7.

73. People R, Bean JC. Calculation of critical layer thickness versus lattice mismatch for GexSi1−x/Si strained-layer heterostructures. Appl Phys Lett. 1985 Aug 1;47(3):322–4.

74. Kaganer VM, Köhler R, Schmidbauer M, Opitz R, Jenichen B. X-ray diffraction peaks due to misfit dislocations in heteroepitaxial structures. Phys Rev B. 1997 Jan 15;55(3):1793–810.

75. Kim YH, Lee JY, Noh YG, Kim MD, Cho SM, Kwon YJ, et al. Growth mode and structural characterization of GaSb on Si (001) substrate: A transmission electron microscopy study. Appl Phys Lett. 2006 Jun 12;88(24):241907.

76. Kim HS, Noh YK, Kim MD, Kwon YJ, Oh JE, Kim YH, et al. Dependence of the AlSb buffers on GaSb/GaAs(001) heterostructures. J Cryst Growth. 2007;301–302:230–4.

77. Boebel FG, Möller H, Hertel B, Grothe H, Schraud G, Schröder St, et al. In situ film thickness and temperature control of molecular beam epitaxy growth by pyrometric interferometry. J Cryst Growth. 1995;150:54–61.

78. He L, Clinger LE, Richardson CJK. Stability of arsenide and antimonide surfaces during molecular beam epitaxy growth. Journal of Vacuum Science & Technology B. 2013 Oct 29;31(6):61204.

79. Henke K. Arsenic: environmental chemistry, health threats and waste treatment. John Wiley & Sons; 2009.

80. Schlesinger ME. Thermodynamic Properties of Solid Binary Antimonides. Chem Rev. 2013 Oct 9;113(10):8066–92.

81. Longenbach KF, Wang WI. Molecular beam epitaxy of GaSb. Appl Phys Lett. 1991 Nov 4;59(19):2427–9.

82. Chang C, Takaoka H, Chang LL, Esaki L. Molecular beam epitaxy of AlSb. Appl Phys Lett. 1982 Jun 1;40(11):983–5.

83. Noreika AJ, Greggi J, Takei WJ, Francombe MH. Properties of MBE grown InSb and InSb1−xBix. Journal of Vacuum Science & Technology A. 1983 Apr 1;1(2):558–61.

84. Ye H, Li L, Hinkey RT, Yang RQ, Mishima TD, Keay JC, et al. MBE growth optimization of InAs (001) homoepitaxy. Journal of Vacuum Science & Technology B. 2013 May 1;31(3):03C135.

85. Rehm R, Walther M, Schmitz J, Fleißner J, Fuchs F, Ziegler J, et al. InAs/GaSb superlattice focal plane arrays for high-resolution thermal imaging. 2006;14(1):19–24.

86. Vurgaftman I, Meyer JR, Ram-Mohan LR. Band parameters for III–V compound semiconductors and their alloys. J Appl Phys. 2001 Jun 1;89(11):5815–75.

87. Jasik A, Sankowska I, Wawro A, Ratajczak J, Jakieła R, Pierścińska D, et al. Comprehensive investigation of the interfacial misfit array formation in GaSb/GaAs material system. Applied Physics A. 2018;124(7):512.

88. Thibado PM, Bennett BR, Shanabrook B V, Whitman LJ. A RHEED and STM study of Sb-rich AlSb and GaSb (0 0 1) surface reconstructions. J Cryst Growth. 1997;175–176:317–22.

89. Bracker AS, Yang MJ, Bennett BR, Culbertson JC, Moore WJ. Surface reconstruction phase diagrams for InAs, AlSb, and GaSb. J Cryst Growth. 2000;220(4):384–92.

90. Liu WK, Santos MB. Surface reconstructions of InSb(001) during molecular beam epitaxy. Surf Sci. 1994;319(1):172–83.

91. de Oliveira AG, Parker SD, Droopad R, Joyce BA. A generalized model for the reconstruction of {001} surfaces of III–V compound semiconductors based on a RHEED study of InSb(001). Surf Sci. 1990;227(1):150–6.

92. Hosoda T, Wang D, Kipshidze G, Sarney WL, Shterengas L, Belenky G. 3 μm diode lasers grown on (Al)GaInSb compositionally graded metamorphic buffer layers. Semicond Sci Technol. 2012;27(5):55011.

93. Zhang J. Room-temperature compressibilities of MnO and CdO: further examination of the role of cation type in bulk modulus systematics. Phys Chem Miner. 1999;26(8):644–8.

94. Ballirano P, Maras A. Refinement of the crystal structure of arsenolite, AS2O3. 2002;217(JG):177–8.

95. Frueh Jr. AJ. The crystal structure of claudetite (monoclinic As2O3). American Mineralogist. 1951 Dec 1;36(11–12):833–50.

96. Whitten AE, Dittrich B, Spackman MA, Turner P, Brown TC. Charge density analysis of two polymorphs of antimony(iii) oxide. Dalton Transactions. 2004;(1):23–9.

97. Zhao B, Cheng P, Pan H, Zhang S, Wang B, Wang G, et al. Weak antilocalization in Cd3As2 thin films. Sci Rep. 2016;6(1):22377.

98. Bergmann G. Weak anti-localization—An experimental proof for the destructive interference of rotated spin 12. Solid State Commun. 1982;42(11):815–7.

99. Shannon RD. Revised effective ionic radii and systematic studies of interatomic distances in halides and chalcogenides. Acta Crystallographica Section A. 1976 Sep 1;32(5):751–67.

100. Pauling L. THE PRINCIPLES DETERMINING THE STRUCTURE OF COMPLEX IONIC CRYSTALS. J Am Chem Soc. 1929 Apr 1;51(4):1010–26.

101. Dietl T. A ten-year perspective on dilute magnetic semiconductors and oxides. Nat Mater [Internet]. 2010;9(12):965–74. Available from: https://doi.org/10.1038/nmat2898

102. Matsukura F, Ohno H, Shen A, Sugawara Y. Transport properties and origin of ferromagnetism in (Ga,Mn)As. Phys Rev B [Internet]. 1998 Jan 15;57(4):R2037–40. Available from: https://link.aps.org/doi/10.1103/PhysRevB.57.R2037

103. Xiao R, Held JT, Rable J, Ghosh S, Wang K, Mkhoyan KA, et al. Challenges to magnetic doping of thin films of the Dirac semimetal Cd3As2. Phys Rev Mater. 2022 Feb 22;6(2):24203.

104. Yuan X, Cheng P, Zhang L, Zhang C, Wang J, Liu Y, et al. Direct Observation of Landau Level Resonance and Mass Generation in Dirac Semimetal Cd3As2 Thin Films. Nano Lett. 2017 Apr 12;17(4):2211–9.

105. Kohler F. Zur Berechnung der thermodynamischen Daten eines ternären Systems aus den zugehörigen binären Systemen. Monatshefte für Chemie und verwandte Teile anderer Wissenschaften. 1960;91(4):738–40.

106. Miedema AR, de Châtel PF, de Boer FR. Cohesion in alloys — fundamentals of a semi-empirical model. Physica B+C. 1980;100(1):1–28.

107. Boom R, Mattens WCM, De Boer FR. Cohesion in metals : transition metal alloys. 2nd corr. Amsterdam : North-Holland; 1989.

108. Dębski A, Dębski R, Gąsior W. New Features of Entall Database: Comparison of Experimental and Model Formation Enthalpies/ Nowe Funkcje Bazy Danych Entall: Porównanie Doświadczalnych I Modelowych Entalpii Tworzenia. Archives of Metallurgy and Materials. 2014;(No 4 December).

109. Jain A, Ong SP, Hautier G, Chen W, Richards WD, Dacek S, et al. Commentary: The Materials Project: A materials genome approach to accelerating materials innovation. APL Mater. 2013 Jul 1;1(1):11002.

110. Vobornik I, Manju U, Fujii J, Borgatti F, Torelli P, Krizmancic D, et al. Magnetic Proximity Effect as a Pathway to Spintronic Applications of Topological Insulators. Nano Lett. 2011 Oct 12;11(10):4079–82.

111. Léger JM. Chalcogenides and pnictides of cerium and uranium under high pressure. Physica B Condens Matter. 1993;190(1):84–91.

112. Gschneidner KA, Calderwood FW. The As−Ce (Arsenic-Cerium) system. Bulletin of Alloy Phase Diagrams. 1986;7(3):276–7.

113. Holbourn PE, Woodhams FWD. A 121Sb Mössbauer investigation of the rare earth antimonides. J Solid State Chem. 1981;39(2):186–94.

114. Gschneidner KA, Calderwood FW. The As−Pr (Arsenic-Praseodymium) system. Bulletin of Alloy Phase Diagrams. 1986;7(4):347–8.

115. Gschneidner KA, Calderwood FW. The As−Nd (Arsenic-Neodymium) system. Bulletin of Alloy Phase Diagrams. 1986;7(4):345–7.

116. Schurr JN. The Synthesis and Characterization of Some Rare Earth Arsenides. AEROSPACE CORP EL SEGUNDO CA MATERIALS SCIENCES LAB; 1987.

117. Gschneidner KA, Calderwood FW. The As−Sm (Arsenic-Samarium) system. Bulletin of Alloy Phase Diagrams. 1986;7(4):349–50.

118. Beeken RB, Schweitzer JW. Intermediate valence in alloys of SmSe with SmAs. Phys Rev B. 1981 Apr 15;23(8):3620–6.

119. Gschneidner KA, Calderwood FW. The As−Eu (Arsenic-Europium) system. Bulletin of Alloy Phase Diagrams. 1986;7(3):279–83.

120. Wang Y, Calvert LD, Taylor JB. The structures of Eu4As3 and La4Sb3. Acta Crystallogr B. 1980;36(1):221–2.

121. Chan JY, Olmstead MM, Hope H, Kauzlarich SM. Synthesis, Structure, and Properties of Eu16Sb11 and Eu16Bi11. J Solid State Chem. 2000;155(1):168–76.

122. Gschneidner KA, Calderwood FW. The As−Gd (Arsenic-Gadolinium) system. Bulletin of Alloy Phase Diagrams. 1986;7(4):340–1.

123. Duan CG, Sabirianov RF, Mei WN, Dowben PA, Jaswal SS, Tsymbal EY. Electronic, magnetic and transport properties of rare-earth monopnictides. Journal of Physics: Condensed Matter. 2007;19(31):315220.

124. Gschneidner KA, Calderwood FW. The As−Tb (Arsenic-Terbium) system. Bulletin of Alloy Phase Diagrams. 1986;7(4):351.

125. Amari S, Yahiaoui IE, Bourourou Y. Electronic and magnetic properties of antiferromagnetic TbAs via modified Becke Johnson potential plus an on-site Coulomb U. Physica B Condens Matter. 2017;515:112–7.

126. Gschneidner KA, Calderwood FW. The As−Dy (Arsenic-Dysprosium) system. Bulletin of Alloy Phase Diagrams. 1986;7(3):277–8.

127. Gschneidner KA, Calderwood FW, Gschneidner KA. The As−Ho (Arsenic-Holmium) system. Bulletin of Alloy Phase Diagrams. 1986;7(4):341–2.

128. Gschneidner KA, Calderwood FW. The As−Er (Arsenic-Erbium) system. Bulletin of Alloy Phase Diagrams. 1986;7(3):278–9.

129. Gschneidner KA, Calderwood FW. The As−Tm (Arsenic-Thulium) system. Bulletin of Alloy Phase Diagrams. 1986;7(4):352.

130. Jabua ZU. Preparation and electrical properties of TbSb films. Inorganic Materials. 2017;53(7):682–4.

131. Habermann CE, Daane AH. Vapor Pressures of the Rare-Earth Metals. J Chem Phys. 1964 Nov 1;41(9):2818–27.